DISSERTATION

A STUDY OF STRUCTURAL ORGANIZATIONS IN AMORPHOUS OXIDE THIN FILMS FOR LOW MECHANICAL LOSS MIRROR COATINGS IN INTERFEROMETRIC GRAVITATIONAL WAVE DETECTORS

Submitted by

Le Yang

Department of Chemistry

In partial fulfillment of the requirements

For the Degree of Doctor of Philosophy

Colorado State University

Fort Collins, Colorado

Summer 2021

Doctoral Committee:

Advisor: Carmen S. Menoni

Jean K. Chung
Grzegorz Szamel
Mark R. Bradley

Copyright by Le Yang 2021

All Rights Reserved

ABSTRACT

A STUDY OF STRUCTURAL ORGANIZATIONS IN AMORPHOUS OXIDE THIN FILMS FOR LOW MECHANICAL LOSS MIRROR COATINGS IN INTERFEROMETRIC GRAVITATIONAL WAVE DETECTORS

Amorphous thin films prepared from vapor deposition are nonequilibrium solids with structures dependent on their physical parameters, such as composition, and method of preparation. The macroscopic properties of an amorphous material are fundamentally connected to the atomic configuration at the microscopic level. Two-level systems, conceptualized as two adjacent potential wells in the potential energy landscape, are due to intrinsic atomic disorder in amorphous materials. When coupled with an elastic field, the configuration change between the two wells creates a dissipation of mechanical energy that manifests itself as the mechanical loss angle. The mechanical loss of the thin films composing the high reflectivity mirror coating has become the dominant noise source limiting further performance improvements for the next generation gravitational wave detectors.

The study presented here comprises investigations of key structural organizations that correlate with the room temperature mechanical loss in vapor-deposited amorphous oxide thin films. In theory, manipulations of substrate temperature or use of assist ion bombardment that transfers energy to the film surface are capable of introducing structural changes during the highly dynamic transition of sputtered particles from the vapor to the solids phase. Tuning the

composition by doping or nanolayering is also effective at altering the atomic structure of the amorphous materials. Herein, we discuss in detail the findings from each work.

In work on Ta_2O_5, the effects of low energy assist ion bombardment on the mechanical loss of amorphous thin films are presented. Bombarding ions of Ar^+, Xe^+, and O_2^+ of different energy and different dose are directed to the thin films' surface during growth. Negligible influence is found from the assist ion bombardment on the atomic structure and mechanical loss of the Ta_2O_5 thin films. Based on an analysis of surface diffusivity, it is suggested that the dominant deposition of Ta_2O_2 cluster might be responsible for the unaltered mechanical loss for Ta_2O_5 thin films. The parameter space explored within the experimental setup is not capable of affecting the atomic arrangements.

It has been proposed that modifiers such as dopants and nanolayers incorporated into the Ta_2O_5 matrix alter the atomic network in a beneficial way. Two systems of SiO_2/Ta_2O_5 and TiO_2/Ta_2O_5 in both mixture and nanolaminate forms are investigated. For the nanolaminates, it is demonstrated that thermal treatment results in a morphological change that involves layer breakup and mixture formation at the interface in the TiO_2/Ta_2O_5 nanolaminate. Similarly, a stable mixed phase is only formed in the TiO_2/Ta_2O_5 mixture after annealing. The formation of a mixture is suggested to be the key to the lower mechanical loss of the TiO_2/Ta_2O_5 in contrast to the SiO_2/Ta_2O_5 system. The two-level systems are essentially modified when the system configures itself in a thermodynamically more stable state. Combined with results from the atomic modeling using molecular dynamics of TiO_2/Ta_2O_5, it is then proposed that the medium-range order in these oxides is key to lowering the room temperature mechanical loss.

A direct evaluation of the modifications at the medium-range order is obtained from work on amorphous GeO_2 thin films. GeO_2 with a maximized degree of medium-range order is in-

vestigated with elevated temperature deposition. It is demonstrated that the medium-range order of amorphous GeO_2, characterized by GeO_4 tetrahedra connected in rings of various sizes, evolves into a more ordered configuration at elevated temperatures. A systematic decrease in mechanical loss is associated with the increase in medium-range order for the GeO_2 thin films. We conclusively show that an improved packing at medium range is linked to the low mechanical loss for the amorphous oxide thin films.

Furthermore, engineering of GeO_2 to achieve a high refractive index is carried out by the incorporation of TiO_2. We identified the optimal cation concentration Ti/(Ge+Ti) around 44%, which provides both low mechanical loss and low absorption loss for the mixture to be used in the multilayer stack. The designed high reflector multilayer is calculated to have the Brownian thermal noise near the target for next-generation Advanced LIGO.

In combination, the results described in this dissertation have identified key structural organizations that affect the room temperature mechanical loss of amorphous oxide thin films. The evolution in the connecting rings of metal-centered oxygen polyhedra in these thin films is essential to altering the medium-range order in the atomic network. Such modifications could be achieved with the formation of a thermodynamically more stable phase, elevated deposition temperature, or post-deposition thermal treatment. Future work to identify the microscopic origin of low-temperature mechanical loss is envisioned for a thorough understanding of the two-level systems present in the amorphous oxides.

ACKNOWLEDGEMENTS

To begin, I would like to thank my advisor, Professor Carmen Menoni, for her mentorship through the Ph.D. program. She has been a role model for me with her diligence in work. As a researcher, she also taught me to view things from different perspectives and to develop a broader vision of the work.

I would like to express my thanks to the dissertation committee for their insightful feedback in many meetings.

Many thanks to Dr. Mariana Fazio, who has been my teammate throughout the project. We've had countless talks that were inspiring and fruitful. We've also spent all day sitting on the floor trying to figure out the problem with the broken pump. It would not have been possible for me to finish the dissertation without her help. And her lovely cat Laszlo, who has helped to cheer me up when I was feeling down.

My colleagues in the lab have also been a great asset to me in my day-to-day work. Aaron Davenport, who has never hesitated to offer his help when needed. Ela Jankowska, who has brought laughter and sunshine to the lab.

Working in the LIGO collaboration has also offered me the great opportunity to learn from experts in different areas. Thanks to Gabriele Vajente from the LIGO lab at Caltech for carrying out the mechanical loss measurements in the work. His efficiency feedback is essential to pushing forward the project.

Finally, I would like to thank my family for their never-ending support and love. My grandfather has encouraged me to be resilient when experiencing difficulties. My parents have taught me to be independent and supported my decisions all the time. And last and not least, my

husband Han. His belief in me has been the motivation for me to carry on with the hard work. Thank you for being a fantastic partner in my life.

TABLE OF CONTENTS

ABSTRACT ii
ACKNOWLEDGEMENTS v
LIST OF TABLES ix
LIST OF FIGURES x

Chapter 1 Introduction 1
1.1 Amorphous Thin Films 1
1.1.1 Structure, Preparation, and Properties of Amorphous Thin Films 1
1.1.2 Two-level Systems and Internal Friction in Amorphous Thin Films . . . 5
1.2 Motivation 7
1.2.1 Gravitational Wave Detection 8
1.2.2 Thin Film Coatings in Gravitational Wave Detectors 10
1.2.3 Coating Brownian Thermal Noise 12
1.2.4 Current Status of Coating Research 15
1.3 Scope of The Work 19

Chapter 2 Experimental Methods 21
2.1 Ion Beam Sputtering Deposition 21
2.1.1 Dual Ion Beam Sputtering System 21
2.1.2 Biased Target Ion Beam Sputtering System 23
2.2 Coating Ring Down measurement 24
2.3 Optical Characterizations 26
2.3.1 Ellipsometry 26
2.3.2 Photo-thermal Commonpath Interferometry 27
2.4 Structural and Composition Characterizations 28
2.4.1 Grazing-Incidence X-Ray Diffraction 28
2.4.2 X-Ray Photoelectron Spectroscopy 29
2.4.3 Rutherford Backscattering Spectrometry 30
2.4.4 Raman Scattering 30

Chapter 3 Modifications of Ion Beam Sputtered Tantala Thin Films by Secondary Argon and Oxygen Bombardment[1] 32
3.1 Introduction 32
3.2 Experimental 34
3.3 Results and Discussion 36
3.4 Conclusions 41

Chapter 4 Investigation of Effects of Assisted Ion Bombardment on Mechanical Loss of Sputtered Tantala Thin Films for Gravitational Wave Interferometers [2] . . 43
4.1 Introduction 44
4.2 Methods 46

4.3 Results and Discussions . . . 50
4.4 Conclusions . . . 60

Chapter 5 Structural Evolution that Affects the Room-Temperature Internal Friction of Binary Oxide Nanolaminates: Implications for Ultrastable Optical Cavities [3] . . . 62
5.1 Introduction . . . 63
5.2 Experimental . . . 65
5.3 Results and Discussion . . . 68
5.4 Conclusions . . . 76

Chapter 6 Enhanced Medium Range Order in Vapor Deposited Germania Glasses at Elevated Temperatures[4] . . . 77
6.1 Introduction . . . 78
6.2 Experimental . . . 80
6.3 Results and Discussion . . . 82
6.4 Conclusion . . . 88

Chapter 7 Reduced Room-Temperature Thermal Noise in TiO_2-Doped GeO_2-Based Coatings for Gravitational Wave Detectors[5] . . . 90
7.1 Introduction . . . 90
7.2 Material Properties . . . 93
7.3 Coating Design for Future Gravitational Wave Detectors . . . 100
7.4 Conclusions . . . 102

Chapter 8 Summary and Outlook . . . 103

Bibliography . . . 106

Appendix A Ion Dose Measurement with Faraday Cup . . . 129

Appendix B Design of Nanolaminates . . . 132

Appendix C GIXRD of GeO_2 Thin Films with Annealing . . . 134

LIST OF TABLES

3.1 Deposition conditions and characterization results for all samples. 35
3.2 Sputtering yield and vacancy creation of Ar^+ and O^+ of different energies. 38
3.3 Refractive index at 1 μm and band gap of all samples 38

4.1 Deposition conditions and characterization results for the control samples. 47
4.2 Deposition conditions and characterization results for samples prepared with Ar^+ assist. 48
4.3 Deposition conditions and characterization results for samples prepared with Xe^+ assist. 48
4.4 Measured optical absorption loss at 1 μm for all samples. 51
4.5 Peak positions from fitting results for Ta 4*f* and O 1*s* peaks. 53

5.1 Deposition conditions of the nanolaminates. 66
5.2 Deposition conditions of the mixtures. 66

7.1 Measured parameters for the best TiO_2:GeO_2 mixture, after annealing at 600°C for 108 hours. 99
7.2 Computed Brownian noise for Advanced LIGO+ multilayer coatings, based on the measured material properties. 101

C.1 Diffraction peak position for GeO_2 after crystallization. 134

LIST OF FIGURES

1.1 Schematic illustration of polyhedral connections of corner-sharing, edge-sharing, and face sharing. . . . 2
1.2 Schematic illustration of an energy landscape. . . . 5
1.3 Representation of the double-well potential, TLS. . . . 6
1.4 A schematic diagram of a Fabry-Perot interferometer. . . . 9
1.5 Bright field TEM image of the ion-beam sputtered $\lambda/4$ multilayer stack of SiO_2 (light) and TiO_2-doped Ta_2O_5 (dark) designed for high reflectivity at 1064 nm. . . . 11
1.6 Advanced LIGO+ design sensitivity. The coating Brownian noise (red) is the dominant noise source at the mid-band. . . . 12

2.1 Schematic of the dual ion beam sputtering deposition system. . . . 22
2.2 Schematic of the biased target ion beam sputtering deposition system. . . . 23
2.3 Coating ring down measurement system inside the vacuum chamber. . . . 25
2.4 Example of the time evolution of the detected mode amplitude in one of the photodetector signals. . . . 26
2.5 Refractive index and extinction coefficient dispersion of a Ta_2O_5 thin film sample. . . . 27
2.6 Schematic illustration of the PCI setup. . . . 28
2.7 Signal voltage as a function of the scanning distance for one GeO_2-TiO_2 mixture coating. . . . 28
2.8 Grazing incidence x-ray diffractograms of GeO_2 thin films annealed at different temperatures. . . . 29
2.9 X-ray photoelectron spectrum of a Ta_2O_2 thin film sample. . . . 30
2.10 Raman scattering spectrum of a GeO_2 thin film. . . . 31

3.1 Absorption loss at 1064 nm for all samples. . . . 37
3.2 Dispersion of refractive index of samples s11, s12, s13. . . . 39
3.3 XPS spectra of Ta 4f doublets of control sample c0, samples s11, and s13. . . . 40
3.4 Coating loss angle of control sample c0 and samples bombarded with assist ions. . . . 41

4.1 Grazing angle x-ray diffraction diffractograms for control sample c2, sample s23 bombarded with Xe^+ assist, and sample s11 bombarded with Ar^+. . . . 52
4.2 Photoelectron spectra of Ta $4f$ and O $1s$ for the as-deposited reference tantala sample, s12, and s22. . . . 53
4.3 Loss angles of samples bombarded by Ar^+ and Xe^+ ions. The ion energy was 100 eV for both samples. . . . 54
4.4 Loss angles of tantala coatings bombarded by Xe^+ ions of different energy. . . . 55
4.5 Loss angles of tantala coatings bombarded with 100 eV Ar^+ and different particle-to-ion arrival ratios. . . . 56
4.6 Loss angles of tantala coatings bombarded with 50 eV Xe^+ and different particle-to-ion arrival ratios. . . . 56

5.1 Schematic of the nanolaminate samples with a 6 nm top layer of Ta_2O_5 and 15 pairs of 1.6 nm SiO_2 or TiO_2 and 6 nm Ta_2O_5. 67
5.2 Room temperature internal friction of nanolaminates and mixtures as-deposited and annealed at different temperatures. 69
5.3 GIXRD patterns of crystallized SiO_2/Ta_2O_5 and TiO_2/Ta_2O_5 mixtures after annealing. 70
5.4 High resolution cross-sectional TEM images of nanolaminates before and after annealing at 650°C. 71
5.5 Diffraction patterns of the crystallized nanolaminates and a single layer Ta_2O_5. 72
5.6 X-ray photoelectron spectra for as-deposited and annealed nanolaminates. 74
5.7 X-ray photoelectron spectrum of Ti 2p in the TiO_2/Ta_2O_5 nanolaminate after annealing at 650°C. 75

6.1 Raman scattering spectra of a-GeO_2 thin films deposited at different temperatures. . 83
6.2 Structural relaxation with annealing characterized by the A_6/A_3 ratio for a-GeO_2 thin films deposited at different substrate temperatures. 84
6.3 Internal friction Q^{-1} of a-GeO_2 thin films deposited at (a) T_{sub} = room temperature (green), (b) T_{sub} = 0.60 T_g (orange), and (c) T_{sub} = 0.83 T_g (purple). 87
6.4 Internal friction Q^{-1} as a function of A_6/A_3 of a-GeO_2 thin films deposited at different temperatures. 88

7.1 Measured refractive index n at 1064 nm as a function of the Ti/(Ti+Ge) concentration for different TiO_2:GeO_2 mixtures. 95
7.2 Grazing incidence x-ray diffractograms from 44% TiO_2:GeO_2 thin films annealed in air at 600 °C and 700°C for 10 hours. 96
7.3 Measured loss angle (top) and Young's modulus (bottom) of mixed titanium oxide and germanium oxide, for the samples as deposited and after 10-hours-long heat treatments (annealing) in air, at increasing temperatures. 98
7.4 Effect of the annealing time on the measured mechanical loss angle (top) and Young's modulus (bottom) for the 44% TiO_2:GeO_2 sample. 100

A.1 Schematic of the Faraday cup measurement. 129
A.2 Current as a function of the negative voltage applied to the deflector for assist beam of 50% Ar and 50% O_2 at different beam voltage and beam current. 130

C.1 Grazing incidence x-ray diffraction pattern for GeO_2 thin films with annealing. 134

Chapter 1

Introduction

In this chapter, Section 1.1 reviews various aspects of the preparation, structure, and properties of amorphous thin films. Section 1.2 introduces the application of the thin films we study and the motivation to the work. In Section 1.3, the scope of the work is described.

1.1 Amorphous Thin Films

1.1.1 Structure, Preparation, and Properties of Amorphous Thin Films

Amorphous thin films play a critical role in modern technology. They maintain disordered microscopic structures similar to the liquid meanwhile exhibit many of the mechanical properties of crystalline solids. They are widely used in various applications ranging from optical fibers made of high-purity amorphous silica, amorphous silicon for photovoltaic cells, to smartphone displays that use vapor-deposited glasses of organic semiconductors [1].

The atomic structure of an amorphous material is absent of translational periodicity found in crystalline material. The types of structural ordering that exist in such material can be categorized based on different length scales [2, 3]. At the short to medium range (2-5 Å), atoms align themselves to balance charge and minimize bond energies. Coordination, bond length, and bond angle are determined by such arrangements. At the medium range (5-20 Å), the key structural and topological descriptors are angles between structural motifs and the connectivity between them. Similarities may exist between the amorphous and crystalline phase at the short and medium range. For amorphous metal oxides, the atomic network could be viewed

as a three-dimensional collection of metal-centered polyhedra or cages constructed by oxygen atoms. The connection between the polyhedra could be corner-sharing, edge-sharing, or face-sharing, depending on how many oxygen atoms are shared between the connecting polyhedra (Figure 1.1). For strong glass-forming oxides such as GeO_2 and SiO_2, the network can be viewed as GeO_4 tetrahedra connected in rings of different sizes, with the dominant being six- and seven-fold rings. Various techniques, including NMR [4], Raman spectroscopy [5], and molecular dynamics simulation [6], have been used to obtain the structural information at this range.

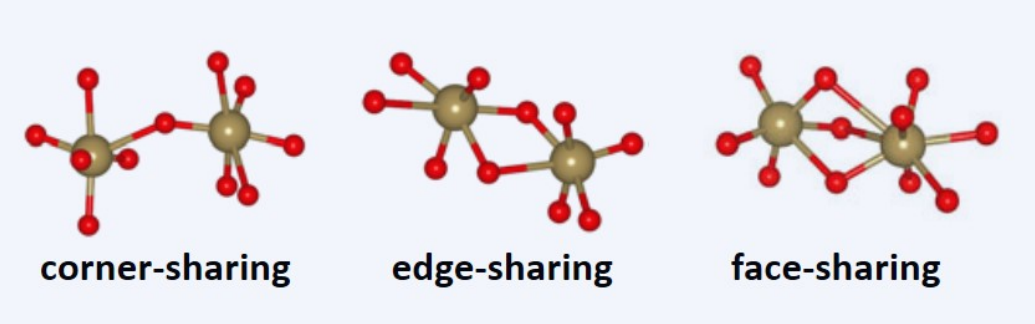


Figure 1.1: Schematic illustration of polyhedral connections of corner-sharing, edge-sharing, and face sharing [7].

The most general process used to form amorphous materials is to quench from the liquid phase sufficiently fast to avoid crystallization [8]. Upon cooling below the melting point T_m, atomic motion becomes so slow that nucleation of crystalline seeds and growth of nuclei into crystallites are avoided. In the end, atoms will rearrange so slowly that they can not adequately sample configurations in the available time allowed by the cooling rate. The liquid's structure appears 'frozen' on the laboratory timescale. Due to insufficient relaxation of the atomic configuration, the supercooled liquid is at a metastable state.

Another efficient means of rapid cooling to produce amorphous materials is vapor deposition. Vapor deposition has been used to prepare organic [9] and inorganic [10] glasses for several decades. The materials prepared with this method are typically in a thin film form, with thickness in the range of a few nanometers to thousands of nanometers. In the process, the target material is firstly vaporized from a solid source in the form of atoms or particles either by introducing thermal energy or by kinetic energy from ions (sputtering). The material is then transported in the form of vapor through a vacuum environment to the substrate, where it condenses, creating a nonequilibrium state. By progressively depositing particles on a substrate, transient liquid-like metastable states reminiscent of those of deeply supercooled oxide liquids are reached. Rapid bond-breaking and re-formation allow for a full relaxation of at least the short-range structure, then subsequent quenching to an amorphous solid has a dynamical transition similar to that of more conventional glasses such as SiO_2 [11]. Theoretical modeling shows that glassy materials prepared by physical vapor deposition are the same as those prepared by slow cooling from the liquid phase [12]. Structures that arise in vapor-deposited materials are statistically identical to those observed in ordinary glasses.

Theoretically, manipulation of the vapor deposition process has the capability to alter the structural organization as newly landed vapor particles are less constrained than in the bulk [13]. Parameters that could be varied include the deposition rate, substrate temperature, and bombarding ions that transfer energy to the surface. For example, in vapor-deposited thin films of itraconazole, the molecule's long axis tends to align with the surface normal with a low deposition rate, whereas nearly isotropic orientation is preferred when the deposition rate is 3 orders of magnitude higher [14]. In a similar fashion, the substrate temperature affects the molecular packing in thin-film organic glasses. Depositing *N*,*N*'-bis(3-methylphenyl)-*N*,*N*'-

diphenylbenzidine at around 0.8 T_g produces glasses with a strong horizontal orientation, while at 0.95 T_g weak vertical orientation is observed [15, 16]. Assist ion bombardment is more commonly used in the deposition of thin films with ion beam sputtering. The structure could be tuned due to enhanced mobility of surface adatoms under low-energy ion bombardment using Xe^+ and Ar^+ [17, 18].

One useful tool to understand the relationships between the structure and the thermodynamics of an amorphous system is the potential energy landscape, which is the hypersurface that the total potential energy of a system forms as a function of coordinates of all the atoms in the system. The manner in which a system samples its landscape as a function of temperature provides information on its dynamic behavior. Figure 1.2 is a schematic illustration of an energy landscape. Despite its topographically complexity, only a few statistical features of the landscape have been found to influence the thermodynamic of the systems significantly. Basins represent possible states with saddle-point potential barriers acting as the transition states. The height of the basin is related to the amorphous material's properties. As the potential energy lowers, fewer and fewer amorphous states, i.e., fewer and fewer ways of arranging the atoms, are accessible. The lowest basin for the amorphous part of the potential energy landscape represents a limiting state of a perfect amorphous packing, known as 'ideal glass,' with configurational entropy equal to that of its crystalline counterpart. In recent experiments, it was discovered that through physical vapor deposition onto a substrate at a controlled temperature and a slow deposition rate, one can create glassy materials that exhibit extraordinary thermodynamic stability [19]. This is possibly due to the existence of a mobile surface layer regenerated by the incoming flux of particles that allows the system to sample deeper configurational states before being buried.

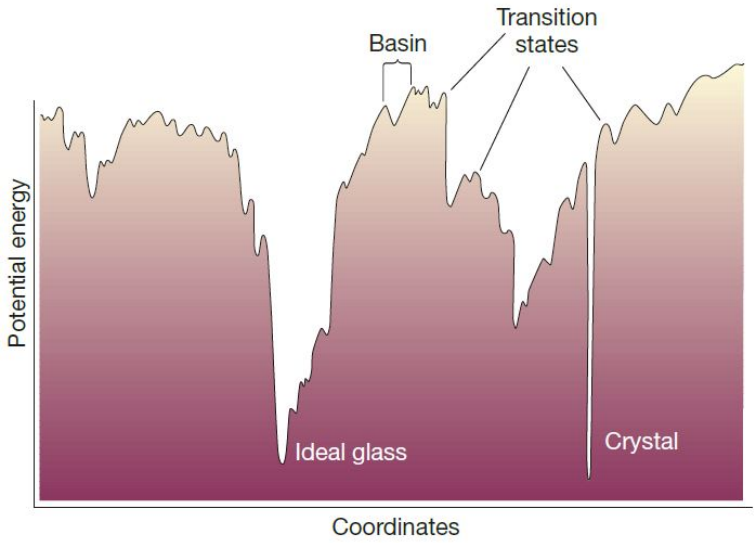


Figure 1.2: Schematic illustration of an energy landscape. The x-axis represents all configurational coordinates [20].

1.1.2 Two-level Systems and Internal Friction in Amorphous Thin Films

It was first suggested by Zeller and Pohl in 1971 [21] that all amorphous solids have low energy excitations in a rather similar magnitude for a wide range of materials. Despite the randomness of the atomic arrangements and chemical composition, most amorphous solids display similarities in their properties at temperatures below a few Kelvin. For example, the thermal conductivity dependence on temperature of all amorphous solids below 1 K were measured to be spaced by a factor of 20 [22]. Similarly, the internal friction (Q^{-1}), which is a measure of anelasticity of the material, approaches a temperature-independent value in the range of 10^{-4} to 10^{-3} at temperatures below 10 K. To understand such universality, a phenomenological model based on the assumption of atomic tunneling was proposed, with the basic principle being that the low-temperature behavior of amorphous systems is dominated by the presence of two-level systems (TLS).

Two-level systems (TLS) are represented by asymmetric double-well potentials in some configuration coordinate, with adjacent wells being geometrical configurations of similar energy separated by an energy barrier (Figure 1.3). Each TLS is characterized by the energy asymmetry between the two configurations (Δ) and the average barrier height (V). Transitions between different configurations are possible through the rearrangements of small groups of atoms. At temperature below 1 K, transitions between states occur via quantum tunneling. At higher temperatures above 5 K, thermally activated transitions dominate over the tunneling mechanism. The nature of the states, however, is the same. A solid can be viewed as a collection of TLS with varied barrier height and energy asymmetry.

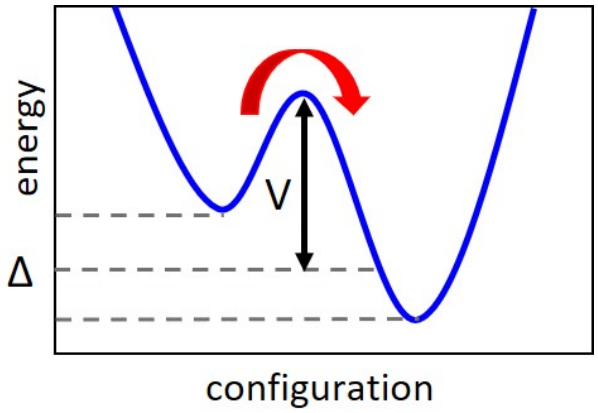


Figure 1.3: Representation of the double-well potential, TLS. Δ is the energy asymmetry and V is the barrier height.

When coupled to the environment, the distribution of TLS gives rise to various acoustic and thermal properties of a solid. Internal friction (Q^{-1}), also known as mechanical loss, of amorphous solids is a macroscopic manifestation of TLS. It can be modeled by an ensemble of TLS, with each TLS contributing to the Q^{-1} by coupling into an elastic field [23]. By finding the TLS distribution and the coupling constant, one can reproduce the low-temperature behavior seen

in experiments. The model was later developed to include thermal hopping to explain higher temperature phenomena [23, 24]. Recent work has shown that using molecular dynamics simulations combined with numerical calculations, the internal friction behavior of amorphous SiO_2 comparable to experimental results could be reproduced [25]. This molecular dynamics based approach allows a direct correlation between the atomic structure and TLS, which would eventually advance the understanding of the microscopic origin of TLS in amorphous solids.

Reducing the internal friction at a given temperature would thus require lowering the density of associated TLS. Recent insight into the synthesis of low internal friction amorphous solids is obtained from work on amorphous Si [26–28]. Amorphous Si, when prepared at elevated growth temperature, has substantially reduced density of TLS near zero. The measured internal friction Q^{-1} is orders of magnitude lower than that of the sample prepared at room temperature. This finding was attributed to an improved atomic packing characterized by less bond angle disorder and higher atomic density from elevated growth temperature. Moreover, remarkable suppression of TLS has also been found in vapor-deposited glasses of indomethacin [29], in which particular molecular arrangements enabled by the substrate temperature have hindered the coupling of the structural defects.

1.2 Motivation

The amorphous oxide thin films studied in this work are utilized as coating materials in the high-reflectivity mirror stack of the end test masses of the interferometric gravitation wave detectors. Improvements in the sensitivity of the detectors have been made possible through the reduction of quantum noise and seismic noise over the past few years [30]. The performance of the detector is now limited by Brownian thermal noise in the mirrors associated with the

internal friction, also known as mechanical loss, in the multilayer coatings. All future detector upgrades and concepts rely on the development of new mirror coating materials to reduce Brownian thermal noise.

1.2.1 Gravitational Wave Detection

The existence of gravitational waves was first predicted by Einsteins' General Theory of Relativity back in 1916 [31]. Asymmetric acceleration of masses would produce fluctuations in the curvature of space-time, or gravitational waves, which propagate at the speed of light. To create waves of detectable amplitude, large masses and accelerations such as those found in astrophysical and cosmological events are required.

In their path of propagation, gravitational waves produce fluctuating forces on masses that manifest themselves as strains, $\Delta L/L$, where L is the measurement baseline. A gravitational wave propagating in the z-direction will alternatively stretch and compress space along the x- and y-directions.

Due to the relative weakness of their interaction with matter, gravitational waves are exceptionally challenging to detect. A promising detector to capture the minute strain would require broadband sensitivity with extremely low noise. The detector was first suggested in the form of a laser interferometer due to its high sensitivity to changes in the interferometer arms' length. Modern gravitational wave detectors are based on a kilometer-scale Michelson interferometer with Fabry-Perot arm cavities (Figure 1.4). These interferometers are designed to measure the separation between widely distant masses with high accuracy. As a gravitational wave passes through an interferometer, traveling perpendicular to the two arms, one arm gets shorter and the other longer. After being reflected from the end test mass mirrors and recombined at the

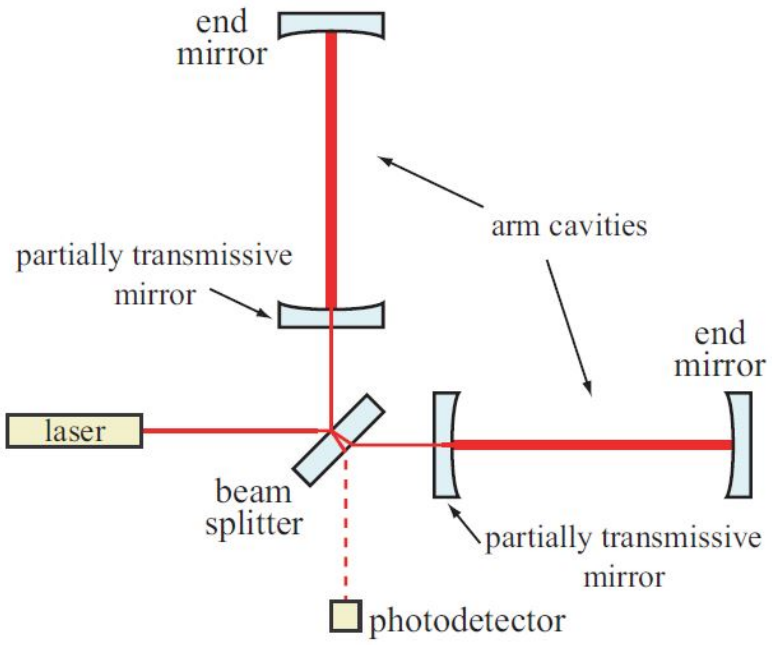


Figure 1.4: A schematic diagram of a Fabry-Perot interferometer [32].

beam splitter, the laser beams interfere to show the change in the relative lengths of the arms that is sensed using the photodetector at the output port. In this configuration, the laser beam is reflected back and forward in the cavity. The high reflectivity mirror at the end of the arm determines the effective number of bounces along the cavity. When the arm length changes due to the interaction with a gravitational wave, the resulting interference is enhanced with each bounce.

On September 14, 2015, the two Advanced LIGO interferometers located in Hanford, WA and Livingston, LA detected the passage of gravitational waves for the first time [33]. The source of the gravitational radiation was the collision of two black holes located roughly 1.3 billion light years from earth. The measured physical displacement caused by the gravitational wave on the two Advanced LIGO interferometers was 4×10^{-18} m, comparable in length to 1/1000 the

diameter of a proton. This remarkable discovery has only been possible with the development of advanced lasers and optical technologies to achieve such measurement precision.

1.2.2 Thin Film Coatings in Gravitational Wave Detectors

The mirrors suspended at the end of the arms in the Fabry-Perot optical cavity are fused silica substrate of 35 cm in diameter, 40 Kg in mass, with high-reflectivity coatings on the surface. The mirror coatings are Bragg reflectors that consist of alternate layers of high (H) and low (L) index thin films, all of one-quarter optical wavelength (λ) thick, where λ is the laser wavelength. The position of the coating surface is a direct measure of the arm length change.

In Figure 1.5, a TEM image of the mirror coating used in the Advanced LIGO detector is shown [34]. It is composed of alternating layers of high-index TiO_2-doped Ta_2O_5 (dark) and low-index SiO_2 (light). The geometrical thickness of the high and low index layer is,

$$t_{\mathrm{H}} = \lambda/(4n_{\mathrm{H}}), \tag{1.1}$$

$$t_{\mathrm{L}} = \lambda/(4n_{\mathrm{L}}), \tag{1.2}$$

where n_{H} and n_{L} are the indices of the refraction of the high and low index films, respectively, and λ is the wavelength of the operating laser.

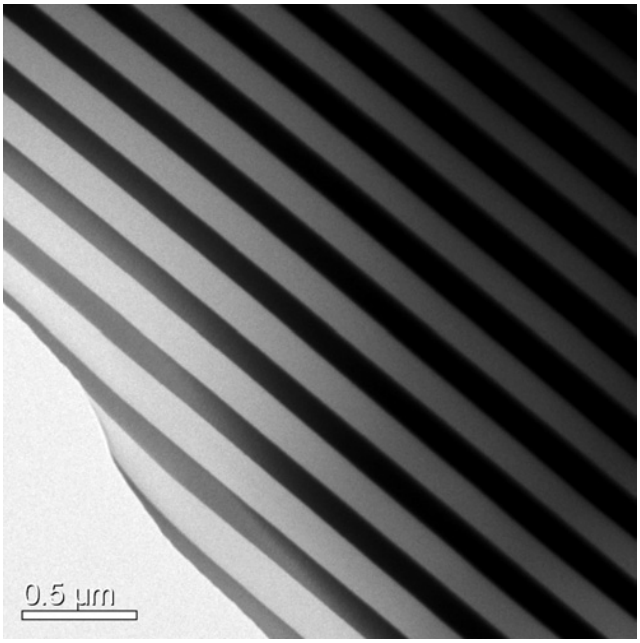


Figure 1.5: Bright field TEM image of the ion-beam sputtered $\lambda/4$ multilayer stack of SiO_2 (light) and TiO_2-doped Ta_2O_5 (dark) designed for high reflectivity at 1064 nm [35].

On each interface between the high and low index layer, part of the incident beam is reflected. The reflected waves experience a phase shift of π only if the incident light goes from the low index layer to the high index layer. The relative phase difference of all reflected beams is zero or a multiple of 2π, creating a constructive interference that leads to high reflectivity at the operating wavelength.

In addition to the high-reflectivity of the mirror coatings, extremely low optical absorption loss at the wavelength of operation (λ = 1064 nm) is required. The mirror coating shown in Figure 1.5 has extraordinary optical absorption loss below 1 ppm [36]. In Advanced LIGO, the high index layer Ta_2O_5 was replaced with TiO_2-doped Ta_2O_5. The average absorption loss of the mirror coating at λ = 1064 nm was measured to be 0.14 $\pm$ 0.05 ppm [36]. For amorphous oxide thin films, the absorption loss is often associated with oxygen deficiency [37] and oxygen

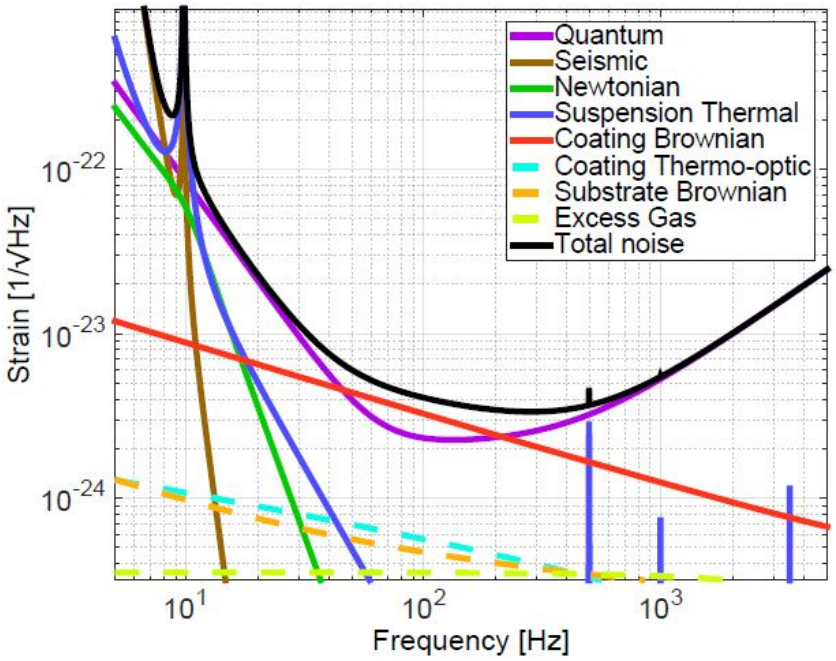


Figure 1.6: Advanced LIGO+ design sensitivity. The coating Brownian noise (red) is the dominant noise source at the mid-band [30].

interstitials [38]. Post-deposition thermal treatment is often a useful tool to remove such defects and reduce the absorption loss [39].

1.2.3 Coating Brownian Thermal Noise

Ideally, the phase shift associated with reflection from the cavity mirror in the gravitational detector is independent of time. Various noise sources cause deviation from this ideal situation, with different effects dominating in different spectral bands. Figure 1.6 shows the current understanding of the fundamental noise sources that limit Advanced LIGO. In the mid-band around 100 Hz, where the system is most sensitive, the dominant noise source is the Brownian thermal noise of the mirror coatings.

In a gravitational wave detector, coating Brownian thermal noise manifests itself as the Brownian motion of the coating. It is associated with the internal friction in the thin film via the fluctuation-dissipation theorem [40].

The main source of internal friction is anelastic relaxation. As described in Section 1.1.2, internal friction in amorphous materials is generally understood as energy coupling from the elastic field into two-level systems present in the amorphous material. It is defined as the dissipation of mechanical energy inside a medium connected with the deviation from Hooke's law as manifested by some stress-strain hysteresis. In an ideal situation, a strain is created instantaneously when stress is applied to the material. For most real materials, the strain response will develop over a finite relaxation time with a lag behind the applied stress. For example, an oscillating stress σ with an angular frequency ω can be expressed as:

$$\sigma = \sigma_0 e^{i\omega t} \tag{1.3}$$

in which σ_0 is the stress amplitude. The resulting strain ϵ will have the same angular frequency ω, but with a phase lag ϕ:

$$\epsilon = \epsilon_0 e^{i(\omega t - \phi)} \tag{1.4}$$

The phase lag ϕ is also known as the mechanical loss angle. It is a measure of the amount of mechanical energy dissipated per cycle of an oscillation at a particular frequency. For a mechanical system resonating at frequency f, the mechanical loss angle $\phi(f)$ can be defined as:

$$\phi(f) = \frac{E_{\text{lostpercycle}}}{2\pi E_{\text{stored}}} \tag{1.5}$$

where $E_{\text{lostpercycle}}$ and E_{stored} are the energy lost per cycle and the total energy stored in the system, respectively. The reciprocal loss angle is also called quality factor Q. Herein, we will use Q^{-1} to refer to mechanical loss or internal friction throughout.

The observable result from such mechanical energy dissipation is the fluctuation of the surface position of the high-reflective mirror. As a result, the mirrors forming the resonators in the arms of the gravitational wave detectors vibrate. This vibration translates into a change in arm length that adds to the detecting signal.

To calculate the thermal noise due to the mechanical loss Q^{-1}, work by Levin directly connects the position of the mirror surface with the dissipation of mechanical energy through the fluctuation-dissipation theorem [40]. In this way, the Brownian thermal noise could be calculated from the power dissipated in the mirror through the interferometer readout of the position of the test mass face, weighted by the Gaussian intensity profile of the sensing laser beam. Further simplification that includes modeling the multilayer as a thick surface layer, assuming the same mechanical loss for strains parallel and perpendicular to the coating surface, allows calculation of the coating Brownian thermal noise at a frequency f, $S_x(f)$ as follows,

$$S_{\text{Brownian}}(f) = \frac{k_B T}{\pi^2 f} \frac{d\phi(f)}{w^2 Y_S} \left(\frac{Y_C}{Y_S} + \frac{Y_S}{Y_C} \right) \tag{1.6}$$

where k_B is the Boltzmann constant, T is the temperature, d is the total thickness of the mirror coating, ϕ_{coating} is the coating mechanical loss, w is the laser beam spot size, and Y_C and Y_S are the Young's modulus of the coating and the substrate, respectively. Therefore, by measuring the mechanical loss of the material, the coating Brownian thermal noise at a certain frequency can be evaluated.

It is also worth noting that in an interferometric gravitational wave detector, there exist other thermally drive fluctuations in the mirror substrates and suspensions. In general, these are not a big concern, as the effects are small in detectors using high-quality silica substrates. Coating Brownian thermal noise, on the other hand, can have a significant effect on the detectors.

1.2.4 Current Status of Coating Research

The gravitational-wave community has started research in mirror coating Brownian thermal noise since it was first shown to be a potential limiting noise source for the interferometric detectors. The mirror coatings used in the initial interferometric gravitational wave detectors were a multilayer stack consisting of ion beam sputtered amorphous SiO_2 and Ta_2O_5 (Figure 1.5). The mechanical loss of the whole stack was found to be dominated by the high index Ta_2O_5 layers rather than the low index SiO_2 layers, with a mechanical loss around 4×10^{-4} for Ta_2O_5 that is substantially larger than 5×10^{-5} for SiO_2 [41].

A reduction in the mechanical loss of these coatings was later achieved through the incorporation of TiO_2 into Ta_2O_5. With approximately 27% TiO_2 addition, the loss angle was reduced by 40% to around 2.4×10^{-4} after annealing at 600°C [35, 42]. Doping concentrations lower or higher than this value were found to result in higher mechanical loss.

The question of why the addition of approximately 27% TiO_2 into Ta_2O_5 introduced the most significant reduction in mechanical loss after annealing has been a topic of great interest since then. At the atomic-scale, a thorough understanding of the structure evolution in the mixture with annealing would advance the understanding of the beneficial modification to the atomic configuration. In recent work [43], a systematic study of pure Ta_2O_5, 27%, and 53% TiO_2-doped Ta_2O_5 was carried out. It was found that all as-deposited thin films have approximately the

same mechanical loss around 8 × 10^{-4}. It was the thermal annealing at 600°C that reduced the mechanical loss of the 27% TiO_2-doped Ta_2O_5 to around 2.8 × 10^{-4}, lower than that of the pure Ta_2O_5 and 53% TiO_2-doped Ta_2O_5. Further annealing to the onset crystallization of the three samples revealed that the diffraction pattern of the crystallized 27% TiO_2-doped Ta_2O_5 has a crystalline structure that corresponded to a stable $TiTa_{18}O_{47}$ ternary phase. When the Ti cation concentration was 53%, however, phase separation occurred after annealing at 600°C with the crystallized phase being rutile TiO_2. The resulting mechanical loss was high in the 13 × 10^{-4} range. The chemical bonding environment of the Ti atoms in the 27% TiO_2-doped Ta_2O_5 was also changed with annealing, showing inconsistency with that in the TiO_2. The indication that the formation of a thermodynamically more stable ternary phase is associated with the low mechanical loss seen in the 27% mixture has brought a new perspective to the community for understanding the relationship between the atomic structure and mechanical loss.

To search for dopant materials that could form a ternary phase in a similar way and further reduce the mechanical loss of Ta_2O_5, a study was carried out with the addition of approximately 20% Al_2O_3, SiO_2, Sc_2O_3, Y_2O_3, ZnO, and ZrO_2 into Ta_2O_5. All mixture thin films were annealed to the highest temperature before crystallization. Among all, the lowest mechanical loss value around 2.8 × 10^{-4} was only obtained for TiO_2- and ZnO-doped Ta_2O_5, while the rest mixtures had higher mechanical losses in the 3.2 - 4.7 × 10^{-4} range. Evaluation of diffraction patterns for crystallized mixtures showed that ternary compounds were only found to form in the case of TiO_2- and ZnO-doped Ta_2O_5 after heat treatment. In the other cases, phase separation occurred with the crystallized phase being β-Ta_2O_5. The increased annealing temperature before crystallization to 800°C by doping of ZrO_2 also improved the mechanical loss to around 3.2 × 10^{-4} after annealing, but by a smaller degree compared to that realized by doping of TiO_2 and

ZnO. The findings further strengthened the assumption that the presence of a thermodynamically more stable phase between two binary oxides would introduce beneficial modifications to the mechanical loss of the mixture with annealing.

Apart from doping, nanolayering has also been envisioned to introduce structural modifications to the atomic network. Nanolayers consist of nanometer-thick layers of two intercalating materials. Experiments on TiO_2/SiO_2 nanolaminates have shown pronounced suppression of mechanical loss at cryogenic temperatures [44]. This behavior was attributed to the interruption of long scale building blocks associated with mechanical loss by constraining the layer thickness.

In parallel to the experimental efforts, extensive atomic modeling has also been devoted to understanding the microscopic origin for mechanical loss in amorphous oxides. One outstanding feature emerged from empirical studies is that thermal annealing reduces the room temperate mechanical loss for all amorphous oxides. The implication of this finding was obtained from the atomic modeling of pure Ta_2O_5 with annealing in work by Hart et al. [45]. The decrease in mechanical loss with annealing was correlated with an increased ordering at the medium range. Additionally, investigation of the structural changes as a result of the doping of Ta_2O_5 with varying levels of TiO_2 was carried out with molecular dynamics simulations [46]. The lowering in mechanical loss appeared to be well correlated with a higher degree of structural homogeneity, and that Ti doping promotes this with an optimum effect around 20-30% Ti. Further evidence of the link between medium-range order and mechanical loss was obtained from work by Prasai using high precision x-ray scattering measurements in combination with molecular dynamics simulations [7]. In this work, atomic modeling of ZrO_2-doped Ta_2O_5 revealed that the systematic change in medium-range order with annealing was associated with

an increasing number of corner-shared polyhedra at the expense of edge-shared ones, and that such change corresponded to the reduction in mechanical loss.

Moreover, since the mechanical loss has been understood with the two-level system model, a direct computation of the loss value from existing two-level systems in the amorphous oxides is necessary. Work along this direction has mainly been carried out using molecular dynamics simulation to search for the local potential minima that a system visits and the transition state between any two consecutive minima [25, 47, 48]. The use of such procedure results in a collection of two-level systems and a distribution of asymmetries and barriers that could then be used to calculate the mechanical loss. Reproduction of the mechanical loss of pure and doped SiO_2 using this method has shown comparable results to those experimentally measured [25]. Furthermore, it was found that different types of TLS are responsible for mechanical loss at different temperatures, with room temperature mechanical loss dominated by TLS of higher barriers [47]. An atomic description of the configurational change that accompanies the TLS transitions is obtained from recent work by Jiang et al. [49]. It was shown that significant events associate with changes in the polyhedral connection contribute to the room temperature mechanical loss of ZrO_2-doped Ta_2O_5, further confirming the observed effect from medium-range order.

Apart from the above-mentioned amorphous metal oxide thin films, significant progress has also been made toward the selection of other potential coatings materials. Amorphous Si that has exceptionally low absorption at λ = 1550 nm and mechanical loss through elevated temperature deposition has been reported in [50]. SiN that has low mechanical loss is also being developed to achieve low optical absorption loss [51]. Moreover, single-crystalline material such as AlGaAs with a mechanical loss around 4×10^{-5} is also a competitive candidate [52],

while the main challenge is the scale-up experiments to grow the material at a diameter of 35 cm.

1.3 Scope of The Work

The work presented in this dissertation focuses on the identification of the key structural organizations that affect the room temperature mechanical loss of amorphous oxide thin films. It is found that the way the metal-centered oxygen cages arrange themselves in the atomic network plays a critical role in affecting the room temperature mechanical loss. The polyhedral connection could be modified with the formation of a thermodynamically stable phase, elevated deposition temperature, and alternatively thermal annealing at high temperatures. Such rearrangements in the polyhedral connecting rings determine the medium-range order in these oxides, and consequently affect the two-level systems associated with the room temperature mechanical loss.

The dissertation is structured as follows. Chapter 2 contains a detailed description of the deposition system and the mechanical loss measurements used in the work. The optical and structural characterization methods are also described.

In Chapter 3, the effects of low energy assist Ar^+ and O_2^+ bombardment on the mechanical loss of amorphous Ta_2O_5 thin films are presented. The implantation of oxygen defects with the O_2^+ bombardment is found to be adversely affecting the mechanical loss. Next, a more systematic study of the influence by varying the assist ion energy and ion dose of Ar^+ and Xe^+ ions is described in Chapter 4. An analysis of surface diffusivity was provided to explain the observed invariance on mechanical loss, possibly due to the dominant cluster deposition.

Chapter 5 focuses on the behavior of room temperature mechanical loss of the SiO_2/Ta_2O_5 and TiO_2/Ta_2O_5 nanolaminates. The morphological and structural evolution upon annealing in the two nanolaminates was studied. The interdiffusion and formation of a stable ternary phase upon annealing in the TiO_2/Ta_2O_5 nanolaminate were correlated with a significant reduction in mechanical loss.

Chapter 6 reports on the modifications in the atomic configuration at medium range of amorphous GeO_2 thin films with deposition at elevated substrate temperatures. Raman spectroscopy was used to probe the ordering at the medium range for thin films deposited at different substrate temperatures and with post-deposition annealing. The results demonstrate a strong correlation between medium-range order and mechanical loss.

Chapter 7 is an extension to Chapter 6 to engineer the GeO_2 thin films for use as the high index material. The incorporation of TiO_2 into GeO_2 was examined with different cation concentrations to identify the optimum concentration for both low mechanical loss and low optical absorption. A multilayer high reflector of TiO_2:GeO_2/SiO_2 was designed to reach the benchmark thermal noise specified for Advanced LIGO+.

Finally, Chapter 8 summarizes the findings of this work and proposes future work to explore the origin of cryogenic mechanical loss with a direct assessment of the density of two-level systems.

Chapter 2

Experimental Methods

In this chapter, Section 2.1 provides a detailed description of the two ion beam sputtering systems used for the thin film preparation, Section 2.2 describes the coating ring down system for the mechanical loss measurements, Section 2.3 introduces the optical characterization methods of the thin films, and Section 2.4 describes the structural and composition characterizations of the thin films.

2.1 Ion Beam Sputtering Deposition

All thin films in this work were prepared by ion beam sputtering deposition. The ion beam sputtering process uses energetic noble gas ions to sputter particles from a solid target surface. The sputtered materials are transported to the substrates in the vapor phase. Depending on the substrate temperature, the landing atoms or particles have limited ability to migrate beyond the point of incidence. Oxidization is achieved by flowing oxygen in the chamber near the target.

2.1.1 Dual Ion Beam Sputtering System

The deposition system described in Chapter 3 and Chapter 4 is a Veeco Spector® dual ion beam sputtering system. A schematic of the system is shown in Figure 2.1.

Gridded broad-beam ion source was used in the system. Ar ions were generated by radio frequency excitation in a bowl, then accelerated electrostatically through ion optics. After leaving the ion source, the ions were neutralized with electrons from the neutralizer. The ion beam

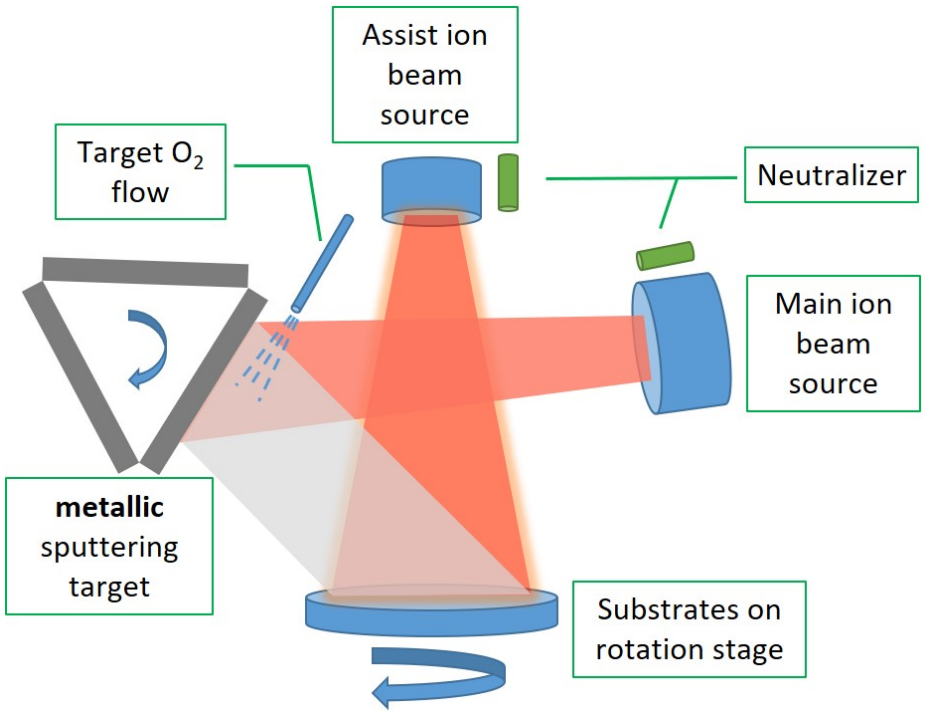


Figure 2.1: Schematic of the dual ion beam sputtering deposition system.

from a gridded source was a composite of beamlets, the profile of which was collimated. The Ar^+ energy was defined by the grid accelerating potential with a range from 100 to 1500 eV.

In addition to the main ion beam source, a second assist beam source directed at the rotating sample holder was equipped in the Veeco Spector®. This ion source was identical to the main ion source but with a smaller diameter.

High purity metallic sputtering targets were used. Oxygen flow was introduced near the target surface to react with the target surface and the sputtered particles.

The substrate holders were fixed on the rotation stage so that uniform deposition could be achieved.

2.1.2 Biased Target Ion Beam Sputtering System

The other deposition system used for thin-film preparation in Chapter 5-Chapter 7 was a biased target ion beam sputtering system LANS, manufactured by 4Wave, Inc (Figure 2.2).

The end-Hall ion source in the system generated ions with energy less than 50 eV. A hollow cathode electron emitter was used to generate electrons. Through a magnetic field, the electrons were directed to the anode to create ions. The ion beam from an end-Hall gridless ion source spread out in all directions. The ion trajectories were not affected by the negative potential on the target until they were within 1-2 mm from that target. The ions struck the target at a near-normal incidence angle.

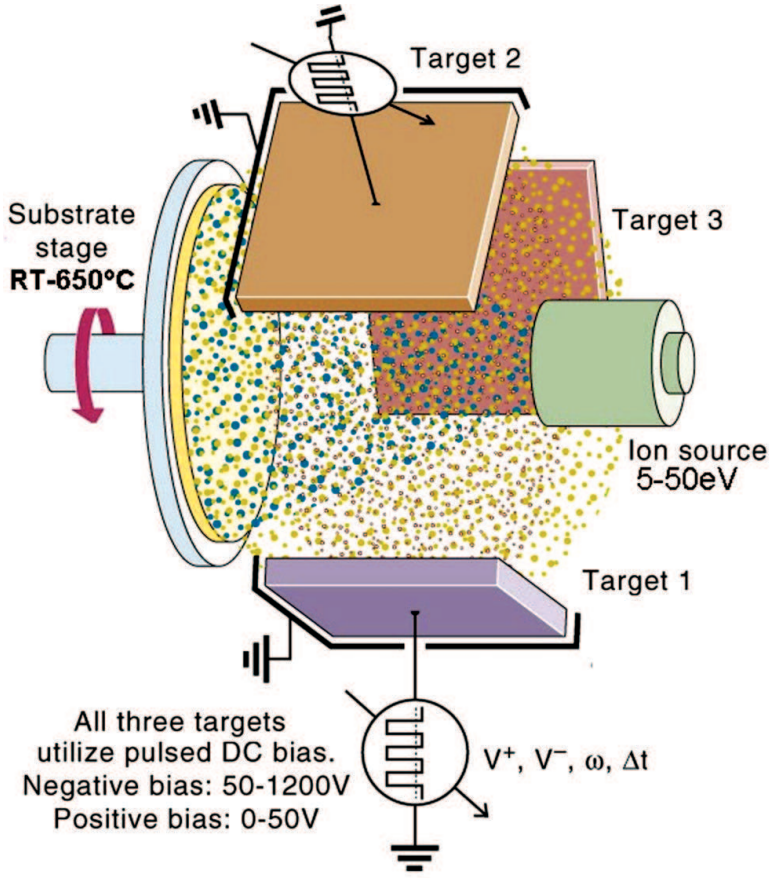


Figure 2.2: Schematic of the biased target ion beam sputtering deposition system. Taken from [53]

.

During the deposition, the metallic targets were negatively biased at 800 V, with selected pulse width. The pulse width was the time that the positive bias (off voltage) was applied to the target. The longer the pulse width, the shorter the time the target was actively sputtered.

Similarly, oxygen flow was introduced into the chamber near the substrate surface for reactive deposition.

2.2 Coating Ring Down measurement

The mechanical loss Q^{-1} of each thin film was evaluated using a ring-down method developed by the LIGO lab at Caltech [54]. The resonant mode of a sample was excited and the amplitude of the resulting motion was allowed to decay freely to extract the mechanical loss angle.

Thin films were deposited on disks of 75 mm in diameter and 1 mm in thickness made of Corning 7980. The disks were held with a gentle nodal suspension (Figure 2.3). To avoid damping due to residual air pressure, the measurements were operated at a pressure below 10^{-6} Torr.

The resonant modes were excited using a non-contacting electrostatic comb actuator held at around 1 mm from the disk surface. All modes were excited simultaneously by driving the amplifier with broadband white noise.

The excited surface motion was measured using a HeNe laser beam directed into the vacuum chamber to hit the upper surface of the disks. The position of the beam on the disk was close to the edge where the resonant modes induce a larger displacement. The reflected beam was sent to a photodetector to obtain a dimensionless normalized beam spot position, which then was converted to the disk angular motion.

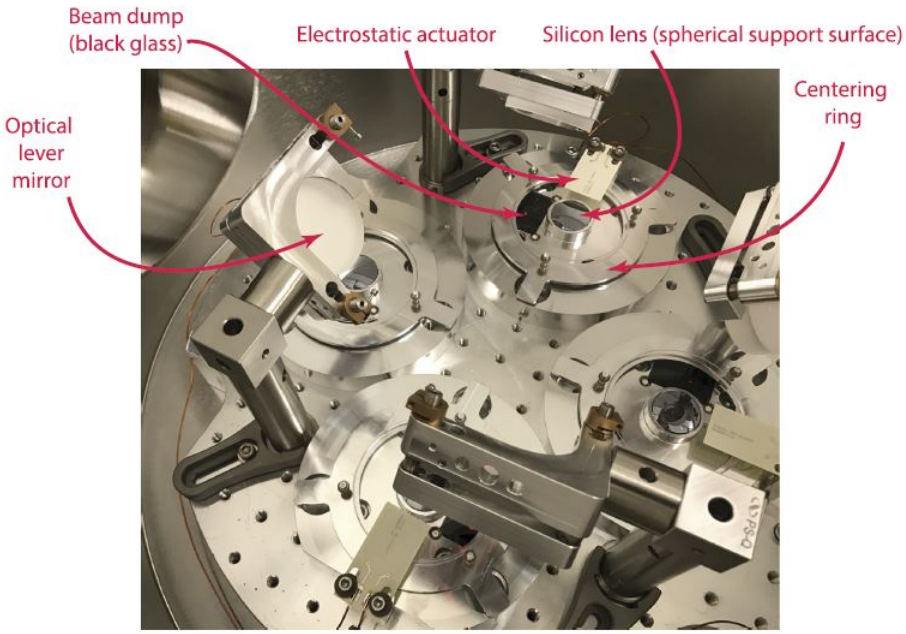


Figure 2.3: Coating ring down measurement system inside the vacuum chamber [54].

The time evolution of the amplitude of the disk motion was then tracked and fitted with exponential decay (Figure 2.4),

$$A_i(t) = A_i(0)e^{-t/\tau_i} \tag{2.1}$$

where A_i was the oscillation amplitude of each mode, τ_i was the decay time constant. τ_i was then related to the mechanical loss Q_i^{-1} at the mode frequency f_i by

$$Q_i^{-1} = \frac{1}{\pi f_i \tau_i} \tag{2.2}$$

For each sample, eight measurements were carried out to obtain an averaged Q_i^{-1}, which was then averaged over the frequency range to obtain the Q^{-1}.

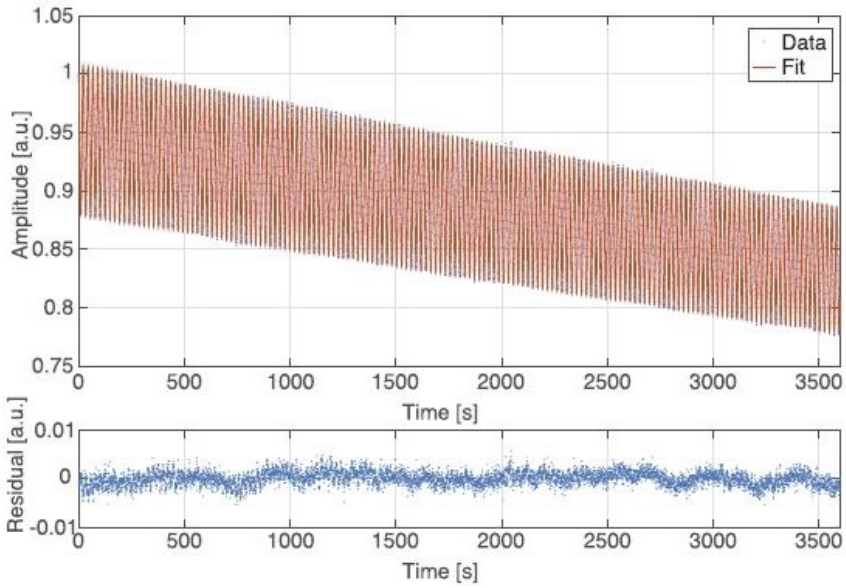


Figure 2.4: Example of the time evolution of the detected mode amplitude in one of the photodetector signals [54].

2.3 Optical Characterizations

2.3.1 Ellipsometry

The thickness and dispersion of the thin film samples were obtained by spectroscopic ellipsometry using a Horiba UVISEL. The change in the polarization state of the light beam reflected on the sample surface was collected in a spectral range of 0.59 eV to 6.5 eV at an incidence angle of 60°. The fitting of ellipsometry data was performed with the DeltaPsi2 software. Dispersion model suitable for amorphous dielectrics was used to obtain the film thickness and refractive index.

Figure 2.5 illustrates the refractive index and extinction coefficient dispersion of a Ta_2O_5 thin film sample.

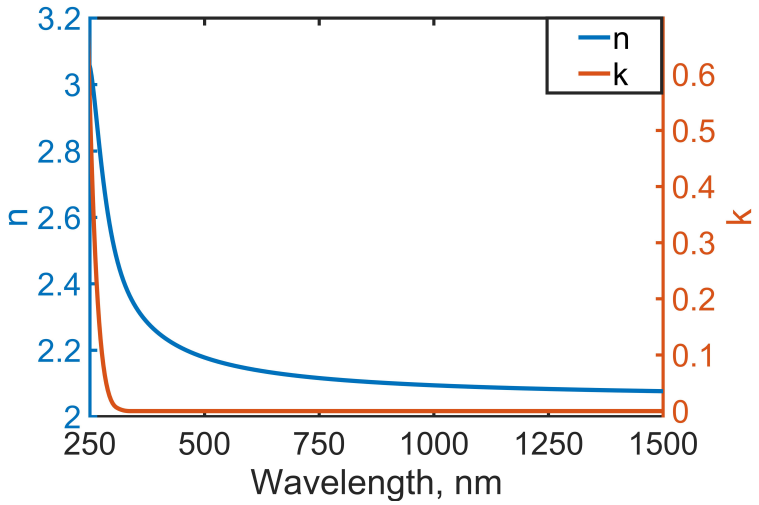


Figure 2.5: Refractive index and extinction coefficient dispersion of a Ta_2O_5 thin film sample.

2.3.2 Photo-thermal Commonpath Interferometry

The optical absorption loss at 1064 nm of each coating was measured by the photo-thermal common-path interferometry (PCI) technique that has a sensitivity better than 1 ppm [55]. With power delivered on coating surface, the heating effect caused a distortion of the probe beam profile in the central area, altering the total beam profile from Gaussian due to interference between distorted and undistorted parts of the probe beam (Figure 2.6). By comparing the peak voltage measured for the sample to that of a calibration sample, the absorption loss was determined. For example, the peak voltage for one GeO_2-TiO_2 mixture sample was measured to be around 4.4×10^{-6} V (Figure 2.7). By comparing it to 2.6×10^{-6} V measured for the calibration sample with an absorption loss of 10.4 ppm, the mixture sample's absorption loss was determined to be around 17.9 ppm.

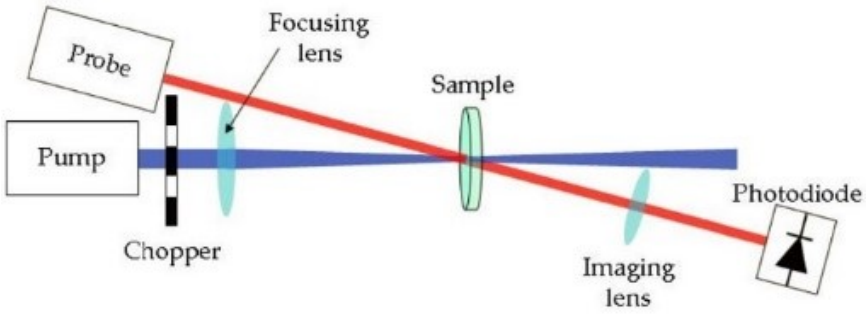


Figure 2.6: Schematic illustration of the PCI setup. Taken from [56].

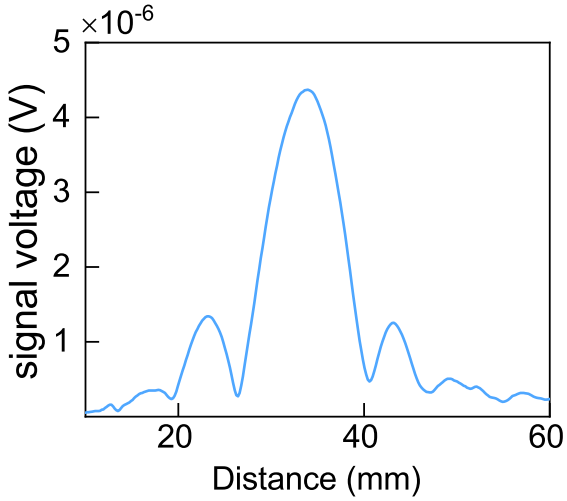


Figure 2.7: Signal voltage as a function of the scanning distance for one GeO_2-TiO_2 mixture coating.

2.4 Structural and Composition Characterizations

2.4.1 Grazing-Incidence X-Ray Diffraction

A Bruker D8 Discover diffractometer with a Cu Kα source at grazing incidence angle was used to examine the amorphous states of the tantala thin films. The diffracted beam was collected by a scintillation detector as a function of 2θ in the range of 10° to 80°. The incident angle was set at 0.5° for all measurements.

Figure 2.8 shows the diffractograms of GeO_2 thin films annealed at different temperatures. The thin film was fully crystallized after annealing at 650°C into an α-quartz phase.

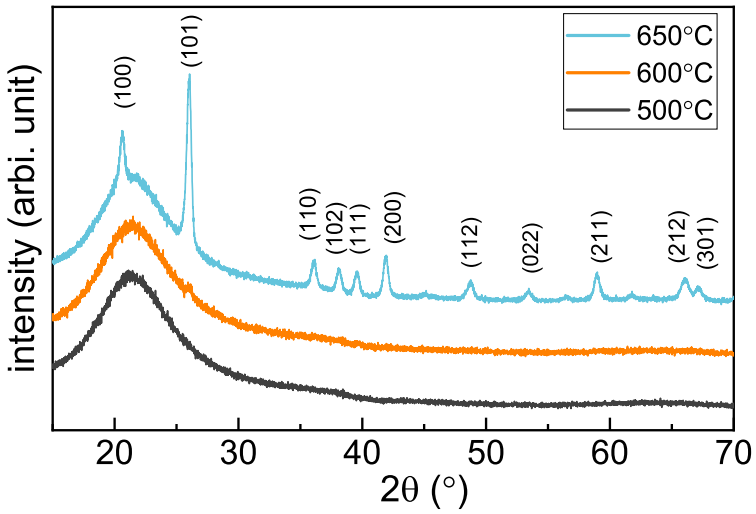


Figure 2.8: Grazing incidence x-ray diffractograms of GeO_2 thin films annealed at different temperatures.

2.4.2 X-Ray Photoelectron Spectroscopy

X-ray photoelectron spectroscopy (XPS) measurements were carried out with a Physical Electronics PE 5800 ESCA/ASE system equipped with a monochromatic Al Kα x-ray source. Samples for this purpose were deposited on p-type (100) Si wafers. A take-off angle of 45° was used for all scans. The neutralizer operating at 10 μA was used to counteract the charging effect of the sample. High-resolution scans were obtained from the sample surface with no sputtering. The C 1*s* peak position was used to calibrate the binding energy scale of the spectra. The peak profile was fitted with the Gaussian function.

Figure 2.9 shows the XPS spectrum of a Ta_2O_5 thin film sample. For the fitting, the doublet peak separation was set at 1.9 V and the peak area ratio was set at 1.33 to 1.4.

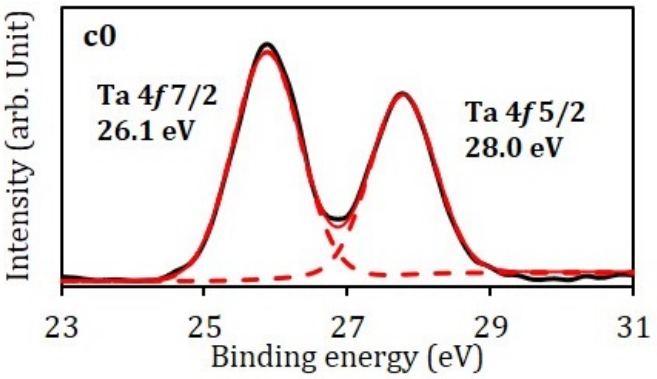


Figure 2.9: X-ray photoelectron spectrum of a Ta_2O_5 thin film sample.

2.4.3 Rutherford Backscattering Spectrometry

Rutherford backscattering spectrometry (RBS) analyses were performed using He^+ ions at 2.035 MeV with a 1.7 MV Tandetron accelerator. Spectra were acquired with samples tilted at 7° to minimize channeling. The scattered ions were collected at an angle of 10° from the beam. The experimental spectra were simulated using the SIMNRA software in order to extract the composition and areal atomic density of the deposited layers.

2.4.4 Raman Scattering

To prepare samples for Raman scattering, a thin Ta layer of 50 nm that has no Raman signal was pre-coated on the fused silica substrate.

Raman scattering was performed with a Horiba LabRAM HR Evolution Spectrometer. A frequency doubled Nd:YAG laser of 532 nm wavelength and 10 mW average power was used for excitation. The laser beam was focused onto the sample's surface using a ×100 objective. Three spectra of 60 seconds acquisition time were collected for each sample and averaged to improve

signal to noise. Deconvolution of the peaks in the Raman spectrum was carried out by fitting the peaks with Gaussian lineshapes.

Figure 2.10 is the Raman scattering spectrum of a GeO_2 thin film sample. The red peak at 420 cm^{-1} corresponds to the symmetric stretching of bridging oxygen in 6-membered rings. The green peak at 520 cm^{-1} corresponds to the breathing motion of bridging oxygen in 3-membered rings. The yellow peak at 333 cm^{-1} is possibly due to Ge motion within the network. The blue peak at 595 cm^{-1} is assigned to Ge-O-Ge bending modes [57, 58].

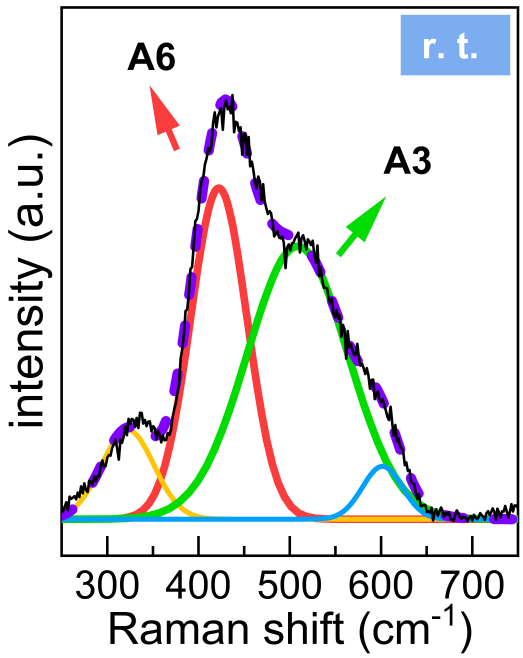


Figure 2.10: Raman scattering spectrum of a GeO_2 thin film.

Chapter 3

Modifications of Ion Beam Sputtered Tantala Thin Films by Secondary Argon and Oxygen Bombardment[6]

Amorphous tantala (Ta_2O_5) thin films were deposited by reactive ion beam sputtering with simultaneous low energy assist Ar^+ or Ar^+/O_2^+ bombardment. Under the conditions of the experiment, the as-deposited thin films are amorphous and stoichiometric. The refractive index and optical band gap of thin films remain unchanged by ion bombardment. Around 20% improvement in room temperature mechanical loss and 60% decrease in absorption loss are found in samples bombarded with 100-eV Ar^+. A detrimental influence from low energy O_2^+ bombardment on absorption loss and mechanical loss is observed. Low energy Ar^+ bombardment removes excess oxygen point defects, while O_2^+ bombardment introduces defects into the tantala films.

3.1 Introduction

Amorphous tantalum pentoxide (Ta_2O_5) is widely used as the high index material in dielectric mirror for applications in astronomy [41], continuous wave laser optics [60], and high-power ultrashort pulse lasers [61]. Ta_2O_5/SiO_2 high-reflection mirrors are used in high-finesse

[6]Substantial portions of this chapter have been reproduced with permission from Le Yang, Emmett Randel, Gabriele Vajente, Alena Ananyeva, Eric Gustafson, Ashot Markosyan, Riccardo Bassiri, Martin Fejer, and Carmen Menoni, *Appl. Opt.*, **2020**, *59*, A150-A154 [59]. ©2020 The Optical Society

optical cavities that require ultrastable optical frequency references [62]. In the successful detection of gravitational waves, the test masses in the interferometer are coated with multilayers of Ti:Ta_2O_5/SiO_2 that have achieved extremely low values of absorption loss at 1064 nm, 0.5 ppm [63], low scattering, and low mechanical dissipation [36,64]. Nevertheless, for applications in ultrastable cavities and the next generation gravitational wave detectors, further understanding of how it will be possible to modify structural properties of the material at the atomic level is necessary to reduce mechanical dissipation.

Ion bombardment during thin film deposition is used to increase the packing density of thin films, as with electron beam evaporation [65], to reduce stress in ion beam sputtered films [66], and to improve the surface smoothness [67]. There are different regimes of use for the assist source. In the energy range of several to tens of eV, the ions are effective in the near-vicinity of the impinge points at the surface, while with hundreds eV they are likely to penetrate the materials and create bulk effects. Re-sputtering of deposited species occurs when input energy reaches around 1000 eV [17]. In previous work, the stoichiometry of SiN was improved with 300-eV to 500-eV N_2^+ bombardment [68]. In ion beam sputtered Nb_2O_5 thin films, it was shown the compressive stress decreased from -230 to -120 MPa when bombarded with assist Ar^+ beyond 250 eV [66]. This effect was attributed to the thermal spike released by energetic ions, inducing a structural relaxation that places atoms in a more stable location.

In this work we investigate modifications in the structural and optical properties of Ta_2O_5 upon low energy Ar^+ and Ar^+/O_2^+ bombardment. It is shown that the refractive index at 1 μm and optical band gap are not changed by assist ion bombardment. Low energy Ar^+ bombardment reduced the absorption loss of the coating compared to the control sample; it also lowered

the coating mechanical loss by around 20 %, possibly by removal of local oxygen defects. Instead, O_2^+ bombardment caused both absorption loss and coating mechanical loss to increase.

3.2 Experimental

Ta_2O_5 Deposition Conditions

Tantala thin films were deposited with a Veeco Spector® dual ion beam sputtering (IBS) system. The substrate was mounted on a rotation stage that was centered on the axis of the assist beam to receive continuous bombardment during deposition. The rotation speed was set at 2 Hz. Chamber temperature was equilibrized at 60°C during deposition while no extra heating was applied to the substrate. A high-purity (99.99 %) Tantalum (Ta) target was sputtered with a primary Ar+ beam at 1250 V and 600 mA in a reactive O_2 atmosphere. An O_2 flow of 49 sccm was introduced into the chamber. For reference, a control sample (c0) was deposited with no assist ion bombardment. The assist beam was operated with Ar^+ or Ar^+/O_2^+ mixture at three conditions by varying the assist beam voltage and beam current as listed in Table 3.1. With the same assist beam condition, the O_2 flow content in the assist source was increased from 0 to 50% to 75%. The deposition rate was at 3 Å/s with no assist ions and slightly lower, 2.8 Å/s, under assist ion bombardment. The assist ion dose at the substrate surface was measured with a Faraday cup and is tabulated in Table 3.1 (Appendix A). The number of sputtered particles was estimated based on the sputtering yield of tantala obtained from transport of ions in matter (TRIM) simulation.

Table 3.1: Deposition conditions and characterization results for all samples.

	c0	s11	s12	s13	s21	s22	s23	s31	s32	s33
Secondary ion beam voltage (V)	n.a.		100			100			200	
Secondary ion beam current (mA)	n.a.		100			100			200	
O_2 content in assist ion source (%)	n.a.	0	50	75	0	50	75	0	50	75
Measured dose (10^{14}ions·cm^{-2}·s^{-1})	n.a.	1.1	2.2	2.3	2.5	4.1	4.1	2.0	3.0	3.2
Thickness (nm)	492.9 ±1.9	479.1 ±1.7	482.2 ±1.9	491.6 ±1.8	486.8 ±1.9	491.0 ±2.0	482.9 ±1.9	480.4 ±2.0	481.8 ±1.9	483.1 ±1.8

Characterization of Ta_2O_5 Thin Films

The thickness, dispersion of the refractive index, and optical band gap of the tantala samples were obtained by spectroscopic ellipsometry using a Horiba UVISEL. The optical absorption loss at 1064 nm of each coating was measured by the photothermal common-path interferometry (PCI) technique that has a sensitivity better than 1ppm [69].

A Bruker D8 Discover diffractometer at grazing incidence angle was used to examine the amorphous states of the tantala thin films. The diffracted beam was collected by a scintillation detector as a function of 2 theta. The incident angle was set at 0.5° for all measurements.

A PE-5800 X-ray photoelectron spectrometer (XPS) was used to check the bonding states of Ta in samples deposited on p-type (100) Si wafers. High-resolution spectra were scanned for Ta 4f, O 1s, and C 1s. Peak positions and widths were determined from a least square fitting using MultiPak. The peak separation of Ta 4f doublet was kept at 1.91 eV and an area ratio at 1.33 in the data fitting.

To evaluate room temperature mechanical loss in the tantala coatings, gentle nodal suspension measurements were carried out at California Institute of Technology [54]. The decay of the disk oscillation amplitude after electrical excitation was tracked to obtain the coating loss angle. Annealed fused silica disks of 75 mm diameter and 1 mm thickness were used to deposit the tantala samples for loss angle measurements.

3.3 Results and Discussion

The absorption loss at 1064 nm of each sample is plotted in Figure 3.1. For control sample c0, a green line is used to represent the absorption loss at 22 ppm. The corresponding absorption loss for the rest of the samples bombarded with assist Ar^+ or Ar^+/O_2^+ are shown separately in the figure. When comparing samples bombarded with Ar^+ only (solid marks), s11 with 100 V 100 mA assist beam is found to have a significantly decreased absorption loss of 7 ppm. The reduction is associated with energetic Ar^+ removing excess oxygen defects that are initially implanted in the film due to high O_2 flow of 49 sccm used during deposition, as is found in Sc_2O_3 that oxygen interstitials can be created by high O_2 flow in the chamber [38].

As shown in Table 3.2, TRIM simulation of 100-eV Ar^+ bombarding Ta_2O_5 indicates a preferential sputtering of O 6 times higher than Ta, which could be accounted for the removal of excess oxygen defects. When the Ar^+ ion energy is increased to 200 eV, a higher absorption loss of 18 ppm in s31 is found (blue solid mark). It is estimated that 3.6 vacancies are created by one 200-eV Ar^+ whereas only 1.4 vacancies by 100-eV Ar^+. The higher possibility of vacancy creation gives rise to the formation of point defects that lead to higher absorption. Increasing the projectile ion energy to 500 eV renders a tantala film that is dark, metallic-like. The addition of O_2^+ in the assist source is intended to maintain the stoichiometry under energetic ion bombardment,

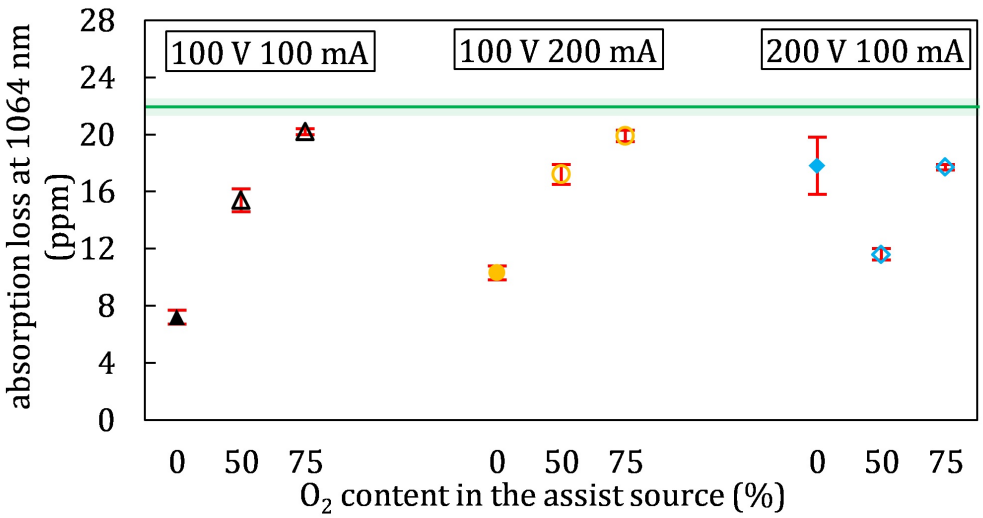


Figure 3.1: Absorption loss at 1064 nm for all samples. Green solid line represents the absorption loss of control sample c0. Samples bombarded with Ar^+ only are shown in solid marks, and samples bombarded with O_2^+ in empty marks.

as was observed in SiN [68]. The results in Figure 3.1, nevertheless, show that the absorption loss increases as the O_2^+ content increases for samples that are bombarded with 100-eV ions. If we assume one 100-eV O_2^+ breaks down to two 50-eV O^+ upon interaction with the surface [70], the resulting bombardment of Ta_2O_5 by 50-eV O^+ leads to almost 100 times more preferential sputtering of O over Ta. This in turn will result in more damage points at the oxygen site and as a result a higher absorption loss. The trend is not seen in group 3. Nevertheless, the results show that in all cases, the absorption loss remained at or below the level of the control sample c0.

In Figure 3.2, the dispersion of the refractive index is plotted for sample series 1 and series 3. These results show almost no variation between different samples. The refractive index at 1 μm of all samples falls in the range of 2.09 to 2.11 (Table 3.3) which is consistent with values previously reported [71]. These results indicate that within the parameter space of operation of the assist ion source in these experiments, the tantala films remain dense. This is likely due

Table 3.2: Sputtering yield and vacancy creation of Ar^+ and O^+ of different energies.

		Sputtering yield Ta atom/ion	Sputtering yield O atom/ion	Vacancies /ion
Ar^+ energy (eV)	100	0.07	0.40	1.4
	200	0.13	0.91	3.6
	500	0.24	1.85	8.9
O^+ energy (eV)	50	0.001	0.11	0.3
	100	0.024	0.36	1.2

to the fact that the amount of tantala particles sputtered from the target exceeds the dose of assist ions impinging on the growing film at all conditions. A similar observation was reported by Ref [72]. The optical band gap of each sample, obtained from the ellipsometry model fit, also remains unchanged with a value near 4 eV.

Table 3.3: Refractive index at 1 μm and band gap of all samples

	c0	s11	s12	s13	s21	s22	s23	s31	s32	s33
Refractive index n at 1064 nm	2.1 ±0.1	2.09 ±0.1	2.10 ±0.1	2.08 ±0.1	2.11 ±0.1	2.11 ±0.1	2.10 ±0.1	2.10 ±0.1	2.09 ±0.1	2.09 ±0.1
Optical band gap (eV)	4.00 ±0.02	4.03 ±0.02	4.02 ±0.03	4.02 ±0.03	4.00 ±0.02	3.98 ±0.03	3.99 ±0.02	4.00 ±0.03	4.01 ±0.03	4.01 ±0.03

The structural properties of tantala thin films showed no evidence of modification by ion bombardment. All samples were found amorphous from X-ray diffraction. A well-defined Ta 4f doublet at around 28 eV and 26.1 eV with no suboxide shoulder at lower binding energies was observed with XPS for all samples. These values were in good agreement with tabulated values for Ta 5+ in Ref [73], indicating stoichiometry. Shown in Figure 3.3 are the doublets for

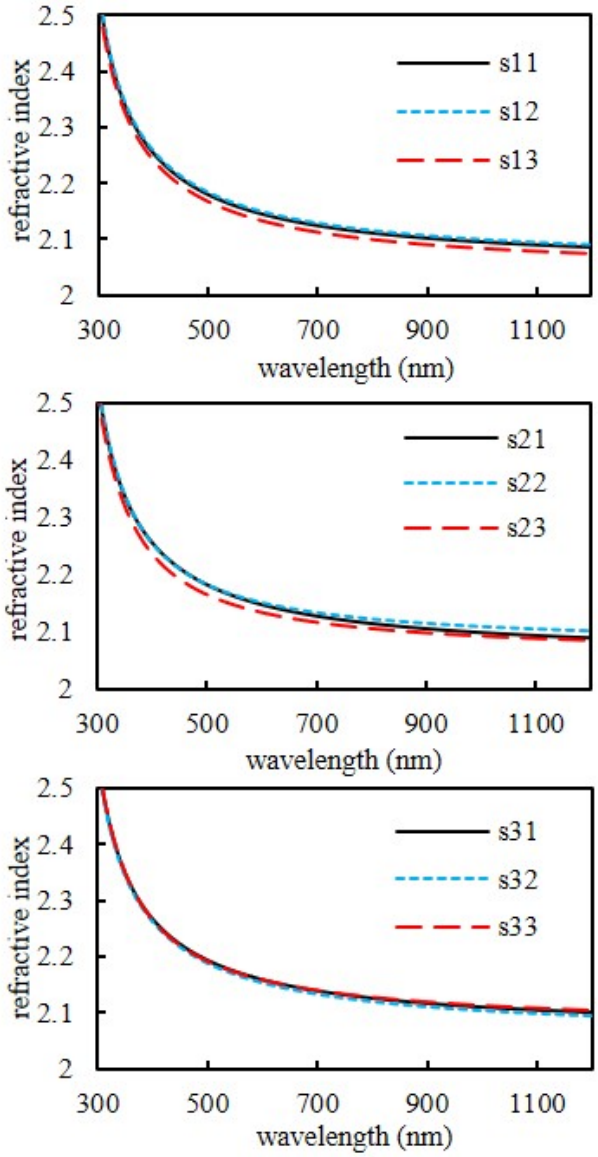


Figure 3.2: Dispersion of refractive index of samples s11, s12, s13. Samples s21, s22, and s23 show very similar behavior to group 1. Group 3 shows there are no variations in the dispersion.

control c0, samples s11, and s13 that have the smallest and highest absorption loss, respectively. Stoichiometry was maintained regardless of the variation in absorption loss.

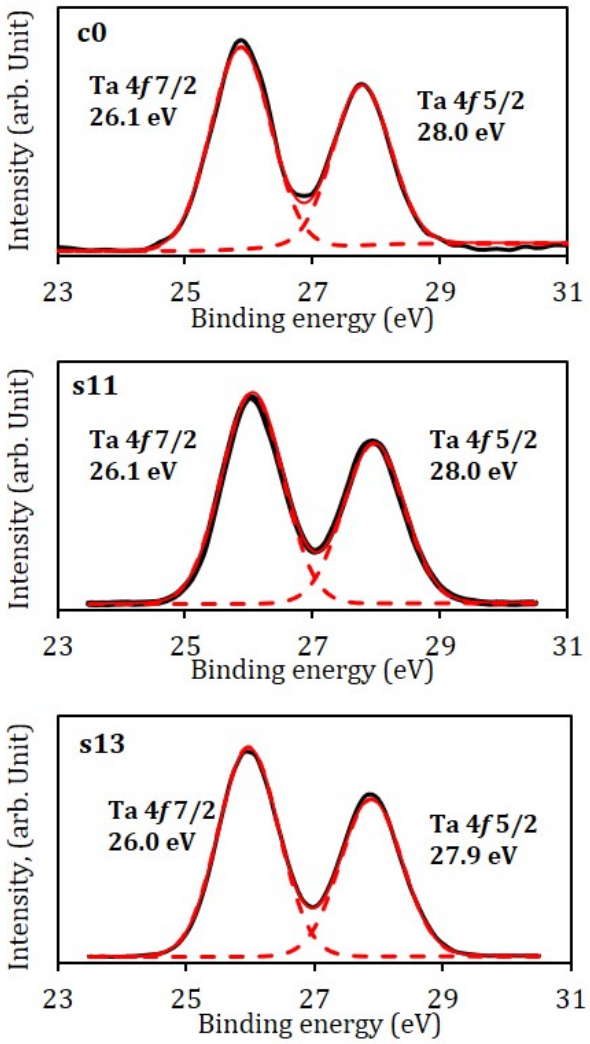


Figure 3.3: XPS spectra of Ta 4f doublets of control sample c0, samples s11, and s13. s11 has the smallest absorption loss of 7 ppm and s13 has the highest absorption loss of 20 ppm.

The room temperature mechanical loss of each coating is shown in Figure 3.4. Control sample c0 has a loss angle of 8.6×10^{-4}, represented by the green line in Figure 3.4, while samples bombarded with assist ions have values ranging from 6.4×10^{-4} to 8.9×10^{-4}. We compared samples in each group that were bombarded with increasing O_2^+ in the secondary ion source

to show the loss angle increases as the O_2^+ content increases. The increase in loss angle for all samples correlates with the increase in density of oxygen defects created in the film due to low energy O_2^+ bombardment. Around 20% lower room temperature mechanical loss is found in s11 and s21 bombarded with 100 eV Ar^+. Furthermore, upon annealing at 500°C, all coatings' loss angles were reduced to 4×10^{-4} (represented by the red dotted line) regardless of the initial value. The results are consistent with reported values for annealed tantala coatings in Ref [74]. The annealing process significantly removes oxygen defects and modifies the atomic structure more than any assist ion bombardment.

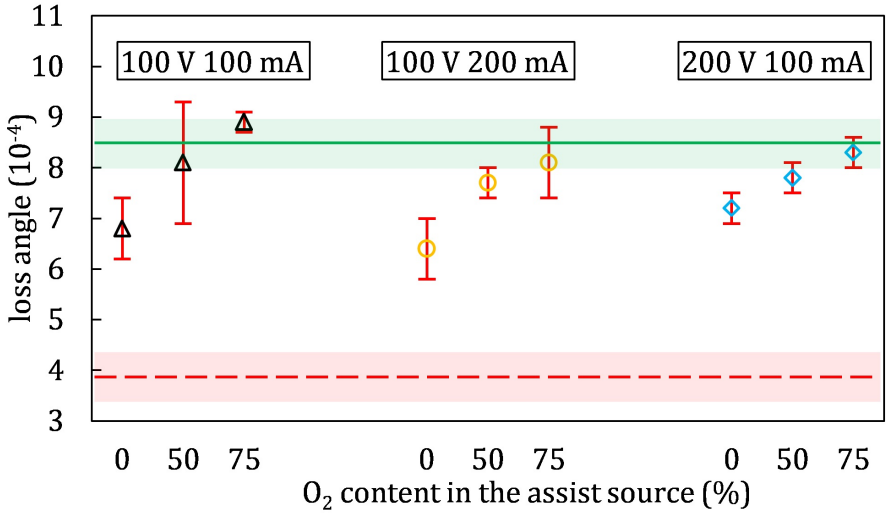


Figure 3.4: Coating loss angle of control sample c0 and samples bombarded with assist ions. The green solid line represents the loss angle of control sample c0, and the red dotted line represents the loss angle of annealed samples. The shades indicate the experimental error.

3.4 Conclusions

Based on the above-mentioned results, two conclusions can be made: 1) Under the parameter space in these experiments, low energy Ar^+ bombardment removes oxygen point defects

that are initially implanted in the films by excess O_2 used during deposition. Increased O_2^+ in the assist source, however, introduced oxygen point defects that contribute to both higher absorption loss and larger mechanical loss in the film. The annealing process effectively eliminated such point defects; 2) The packing density indicated by refractive index and film stoichiometry from XPS shows no modification from secondary ion bombardment, possibly due to a larger number of particles sputtered from the target than the dose of assist ions impinging on the growing film at all conditions. To further investigate the effect of assist ion bombardment on coating mechanical loss, parameters that vary particle-to-ion arrival ratio and energy deposited at the substrate surface, such as deposition rate, ion energy, and ion type, need to be systematically evaluated [75].

Chapter 4

Investigation of Effects of Assisted Ion Bombardment on Mechanical Loss of Sputtered Tantala Thin Films for Gravitational Wave Interferometers [7]

Reduction of Brownian thermal noise due to mechanical loss in high-reflectivity mirror coatings is critical for improving the sensitivity of future gravitational wave detectors. In these mirrors, the mechanical loss at room temperature is dominated by the high refractive index component, amorphous tantala (Ta_2O_5) or tantala doped with titania ($Ti:Ta_2O_5$). Toward the goal of identifying mechanisms that could alter mechanical loss, this work investigates the use of assist ion bombardment in the reactive ion beam sputtering deposition of tantala single layers. Low-energy assist ion bombardment can enhance adatom diffusion. Low-energy assist Ar^+ and Xe^+ ion bombardment at different conditions was implemented during deposition to identify trends in the mechanical loss with ion mass, ion energy, and ion dose. It is shown that the atomic structure and bonding states of the tantala thin films are not significantly modified by low-energy assist ion bombardment. The coating's mechanical loss remains unaltered by ion bombardment within errors. Based on an analysis of surface diffusivity, it is shown that the dominant deposition of tantala clusters and the limited surface diffusion length of oxygen atoms constrain structural changes in the tantala films. A slower deposition rate coupled with

[7] Substantial portions of this chapter have been reproduced with permission from Le Yang, Emmett Randel, Gabriele Vajente, Alena Ananyeva, Eric Gustafson, Ashot Markosyan, Riccardo Bassiri, Martin Fejer, and Carmen Menoni, *Phys. Rev. D*, **2019**, *100*, 122004 [75]. ©2019 The American Physical Society

a significant increase in the dose of the low-energy assist ions may provide more favorable conditions to improve adatom diffusivity.

4.1 Introduction

Gravitational waves emerge from energetic processes of astrophysical bodies in the Universe. To detect a gravitational wave strain ($\Delta L/L$) of 10^{-23} or smaller, gravitational wave detectors based on kilometers-scale interferometers have been established [33, 76, 77]. In the midband (approximately 100 Hz), in which the Advanced LIGO (aLIGO) detector is most sensitive, Brownian thermal noise from the coatings in the test masses is the dominant source of noise [78, 79].

In aLIGO, the coatings on the test masses consist of alternating layers of amorphous silica (SiO_2) and titania-doped tantala ($Ti:Ta_2O_5$) deposited by ion beam sputtering with less than 1 ppm optical absorption loss at 1064 nm [35, 36, 63]. The thermal noise of the coatings is estimated from the internal mechanical losses of the layer materials based on the fluctuation-dissipation theorem [80, 81]. It is well established that the coating's loss angle is dominated by the high-index $Ti:Ta_2O_5$ layer (2.9×10^{-4}) rather than the low-index SiO_2 layer (1.1×10^{-5}) [82]. A successful strategy that has been employed to reduce the loss angle in tantala is to incorporate impurities, such as Ti, Zr, Nb, and Hf [42]. Modeling of the atomic structure of Ti-doped and undoped Ta_2O_5 showed that the doping modifies the medium-range order that correlates with reduced mechanical loss [46].

In this work, we explore the use of low-energy assist ion bombardment during the reactive sputtered deposition of ion beam sputtered (IBS) tantala thin films to investigate whether it would be possible to alter surface diffusion of particles (representing atoms, molecules, and

clusters) sputtered from the target and chemi-sorbed on the growing tantala films. Enhanced surface mobility has been claimed to favor an atomic network that is thermodynamically more stable. Glasses with unprecedented thermodynamic stability enabled by high adatom mobility are reported in Ref [29]. Work on amorphous Si (a-Si) deposited at elevated temperature also indicates suppressed mechanical loss at low temperature [26] and at room temperature [50], presumably via increased surface mobility. With the specific goal of enhancing surface mobility as observed in a-Si, tantala thin films were deposited by Vajente *et al.* with IBS at elevated temperatures [83]. The loss angle of the as-deposited tantala coatings reduced from around 16×10^{-4} to 6×10^{-4} when the substrate temperature increased from 30°C to 400°C. Nevertheless, a major reduction in loss angle to 4×10^{-4} was achieved with post-annealing at 500°C independent of the initial deposition temperature. Alternatively, assist ion bombardment can lead to increased surface mobility. Previous work has shown that low-energy (i.e., 65 eV) bombardment using He^+, Ar^+, and Xe^+ ions increased the surface diffusion of Ge on Si(111) [84,85]. Atomic rearrangement in Ge was also achieved during the thermal spike induced by Ar^+ ion bombardment [86].

In the results described herein, amorphous tantala thin films were deposited by reactive IBS with concurrent low-energy assist Ar^+ and Xe^+ ion bombardment, respectively. The assist ion beam was operated at conditions that altered the assist ion energy and dose at the surface of the growing tantala film. It is shown that the atomic structure and bonding states of the tantala thin films are not significantly modified by the assist ion bombardment. Assessment of the room temperature mechanical loss shows that loss remains unaltered by low-energy ion bombardment within experimental errors. An analysis of mass transfer surface diffusivity shows

that at the assist conditions of the experiment reordering by ion-assisted diffusion is negligible due to low coverage of mobile adatoms and the high diffusion activation energy of clusters.

4.2 Methods

Thin Film Deposition

Tantala thin films were prepared using a Veeco Spector® dual IBS system. The system was baked at 150°C for 1 h and pumped down to 2.6×10^{-5} Pa before deposition to reduce water partial pressure to below 10^{-6} Pa. The main ion beam source using Ar^+ sputtered a Ta target in a reactive oxygen atmosphere at different beam voltages and beam currents that altered the deposition rate. In the absence of assist bombardment and when keeping the chamber temperature at 60°C, the substrate reached an equilibrium temperature of approximately 100°C. The assist ion beam source was operated using either Ar^+ or Xe^+ to bombard the growing film at normal incidence concurrently. The substrate was positioned on a fixed rotation stage that at all times faces the assist ion source. The rotation speed was set at 4π rad/s. The temperature of the film/substrate, in this case, increased to approximately 130°C when using 100 eV bombarding ions. Two 75 mm diameter, 1 mm thick fused silica disks were coated for mechanical loss measurements. Using the same conditions, the tantala films were deposited on 25.4 mm diameter fused-silica and silicon (100) substrates for optical and structural characterization.

Two control tantala thin film samples were deposited using the main ion source at different conditions with no assist ion beam (Table 4.1). The deposition rate decreased from 3.6 Å/s (c1) to 0.9 Å/s (c2) when the main ion beam voltage and beam current were lowered. These deposition rates are indicative of complete oxide coverage of the Ta target [38]. Nevertheless,

the sputtered particles that reach the substrate are a combination of Ta atoms and tantalum oxide fragments, the majority of which were found to be Ta_2O_2 ring clusters [87]. The variation in the deposition rate was used to control the arrival ratio between particles sputtered from the Ta target and the assist ions dose at the substrate surface.

Table 4.1: Deposition conditions and characterization results for the control samples.

Sample	Main beam voltage (V)	Main beam current (mA)	Assist beam voltage (V)	Assist beam current (mA)	Deposition rate (Å/s)	Thickness (nm)
c1	1250	600	n.a.	n.a.	3.6	523.6 ± 1.9
c2	1000	300	n.a	n.a.	0.9	503.8 ± 1.2

Two sets of runs were carried out with either Ar^+ or Xe^+ assist bombardment. In each set, the assist ion energy and dose were modified by varying the assist ion beam voltage and current. Details of the deposition conditions are in Tables 4.2 and 4.3. The number of particles arriving at the substrate was estimated from the deposition rate of the control samples assuming sputtering of Ta_2O_2 clusters. For c1, with a deposition rate of 3.6 Å/s, the number of particles arriving at the substrate was approximately 2.8×10^{15} particles/(cm^2·s). The assist ion dose at the sample surface was measured with a Faraday cup. For an assist ion beam at 100 V and 100 mA, the ion dose was approximately 1.2×10^{14} ions/(cm^2·s) for Ar^+ and approximately 1.6×10^{14} ions/(cm^2·s) for Xe^+. The particle-to-ion arrival ratio calculated from these quantities is shown in Table 4.2 and Table 4.3.

Table 4.2: Deposition conditions and characterization results for samples prepared with Ar^+ assist. p/i is the particle-to-ion arrival ratio at the substrate surface.

Sample	Main beam voltage (V)	Main beam current (mA)	assist beam voltage (V)	Assist beam current (mA)	Deposition rate (Å/s)	Thickness (nm)	p/i
s11	1250	600	100	100	3.5	479.2 ± 1.7	22/1
s12	1250	600	100	200	3.4	487.0 ± 1.9	10/1
s13	1000	300	100	100	0.8	505.6 ± 2.2	5/1

Table 4.3: Deposition conditions and characterization results for samples prepared with Xe^+ assist. p/i is the particle-to-ion arrival ratio at the substrate surface.

Sample	Main beam voltage (V)	Main beam current (mA)	Assist beam voltage (V)	Assist beam current (mA)	Deposition rate (Å/s)	Thickness (nm)	p/i
s21	1250	600	50	100	3.3	496.0 ± 2.1	40/1
s22	1250	600	50	200	3.3	496.0 ± 2.2	23/1
s23	1000	300	50	200	0.8	469.8 ± 1.6	5/1
s24	1000	300	100	100	0.8	490.4 ± 1.8	4/1

Optical Characterization

The thickness and optical constants of the tantala films were obtained with a Horiba UVISEL spectroscopic ellipsometer. Thin films were scanned with a 60° incident angle from 190 nm to 2101 nm. The films' thickness determined from the fitting had a standard deviation of approximately 2 nm for all samples. The coating's optical absorption loss at 1064 nm was measured by the photo-thermal common-path interferometry technique, which has sensitivity better than 1 ppm [55].

X-ray Diffraction and X-ray Photoelectron Spectroscopy

Grazing angle x-ray diffraction (GAXRD) was used to characterize the atomic structure of the tantala coatings. A Bruker D8 Discover diffractometer with a grazing angle set up was used. An incident angle of approximately 1.5° was used to minimize the diffraction signal from the substrate. The diffracted beam was collected by a scintillation detector as a function of 2theta (2θ).

The bonding states of Ta in the samples coated on p-type (100) Si wafers were examined with a PE-5800 x-ray photoelectron spectrometer (XPS). The take-off angle of 45° was used for all scans. The neutralizer operating at 10 μA was used to counteract the charging effect of the sample due to loss of electrons. The C 1*s* peak position was used to calibrate the binding energy scale of the spectra. High-resolution spectra were collected for Ta 4*f*, O 1*s*, and C 1*s*. A superposition curve fitting procedure was used to analyze the spectra. Peak position and widths were determined from a least-square fitting using MultiPak. The peak shapes were fitted with Gaussian functions. The oxidation state of Ta is represented by the Ta $4f$ 5/2 and Ta $4f$ 7/2 doublet

peak position. When fitting the acquired data, the energy separation of the doublet lines was fixed to 1.9 eV, and the area ratio was fixed to 1.3-1.33.

Coating Mechanical Loss

Each coating's loss angle was assessed with the coating ring-down system developed at California Institute of Technology [54]. The tantala films for this purpose were deposited on fused silica disks 75 mm in diameter and 1 mm in thickness. The system is based on the gentle nodal suspension method. After excitation of the disk modes, the amplitude of the motion at the mode peak frequency was tracked over time. The damping time is directly linked to the total mechanical loss, and the loss angle for the coating can be extracted. Uncoated substrates have a loss angle of 10^{-7} to 10^{-8}, which is orders of magnitude smaller than that of the tantala coatings. The coating's loss angle was measured both in as-deposited and annealed tantala thin films. The annealing procedure includes 1) a 5 h ramp up to 500°C, 2) a 10 h soaking at 500°C, and 3) a 5 h ramp down to room temperature.

The results are presented in the following section.

4.3 Results and Discussions

Optical Properties

All tantala coatings are optically transparent. Non-ion-assisted control films c1 and c2 have refractive indices of 2.10 and 2.09 at 1064 nm, respectively. Similar values ranging from 2.09 to 2.11 were obtained for the tantala samples bombarded with Ar^+ or Xe^+ assist.

Low optical absorption loss at 1064 nm is a requirement for the tantala thin films to ensure that when used in the high reflectors, they meet the stringent absorption loss (approximately 0.5

ppm) required for aLIGO coatings [88]. For most of the approximately 500 nm thick samples, an absorption loss of less than 18 ppm at 1064 nm was measured (Tables 4.4). Preferential sputtering of oxygen by Ar^+ or Xe^+ was not evident at the low ion beam voltages used. One exception is s24, which has an absorption loss of 32.8 ppm. The minimum absorption, 5.5 ppm, was found in sample s21 prepared with a 50 eV Xe^+ assist beam.

Table 4.4: Measured optical absorption loss at 1 μm for all samples.

	c1	c2	s11	s12	s13	s21	s22	s23	s24
Absorption loss (ppm)	22.1 ± 0.7	9.3 ± 0.2	7.2 ± 0.4	10.3 ± 0.4	13.1 ± 0.2	9.4 ± 0.2	5.5 ± 0.1	12.1 ± 0.4	32.8 ± 1.3

Structural and Bonding Properties

Grazing incidence x-ray diffractograms of tantala coatings show an amorphous packing (Figure 4.1). The arrows in Figure 4.1 indicate the theoretical peak positions for the crystalline orthorhombic phase of Ta_2O_5 (PDF 01-082-9637) [89]. There are two main broad peaks between 20° and 40° and between 40° and 70°. Signals from the fused silica substrate contribute to the profile at 2θ = 20.8°. Between the control sample c2, sample s23 bombarded with assist Xe^+, and sample s11 bombarded with Ar^+, there are no significant differences in the spectra. Figure 1 shows that the atomic structure remained amorphous under concurrent ion bombardment, regardless of variance in the ion type, ion energy, or ion dose.

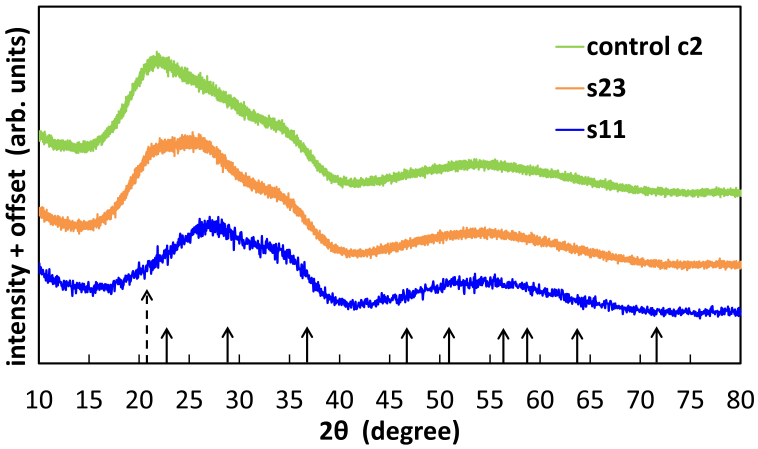


Figure 4.1: Grazing angle x-ray diffractograms for control sample c2, sample s23 bombarded with Xe^+ assist, and sample s11 bombarded with Ar^+. Signals from the fused silica substrate contribute to the peak at 20.8°, as indicated by the dashed arrow. Solid arrows indicate peaks from crystalline orthorhombic Ta_2O_5

The XPS spectra of tantala provide information on the bonding states of Ta in as-deposited samples. As shown in Figure 4.2, close agreement between measured spectra and peak synthesis was obtained. To evaluate the oxidation states, we used a 267 nm thick reference sample deposited using the Veeco Spector® with planetary rotation at a deposition rate of 2 Å/s and with an absorption loss of 3 ppm at 1064 nm. The Ta 4*f* doublet peaks were at 27.9 eV and 26.0 eV for this reference sample (Table 4.5), and the values are consistent with binding energies of Ta in Ta_2O_5 [90, 91]. No suboxide peak was identified. The O 1*s* peak was decomposed into one sharp peak at 530.4 eV and one broad peak at 531.9 eV. The latter was attributed to surface contamination [90]. The XPS spectra of s12 and s22 have the largest and smallest mechanical loss are displayed in Figure 4.2. For both Ta 4*f* doublets and O 1*s* peaks, the peak center did not shift from that of the reference sample (Table 4.5). These results indicate that, within the sensitivity of XPS, there are no significant changes in bonding states in tantala samples prepared with and without ion-assisted bombardment.

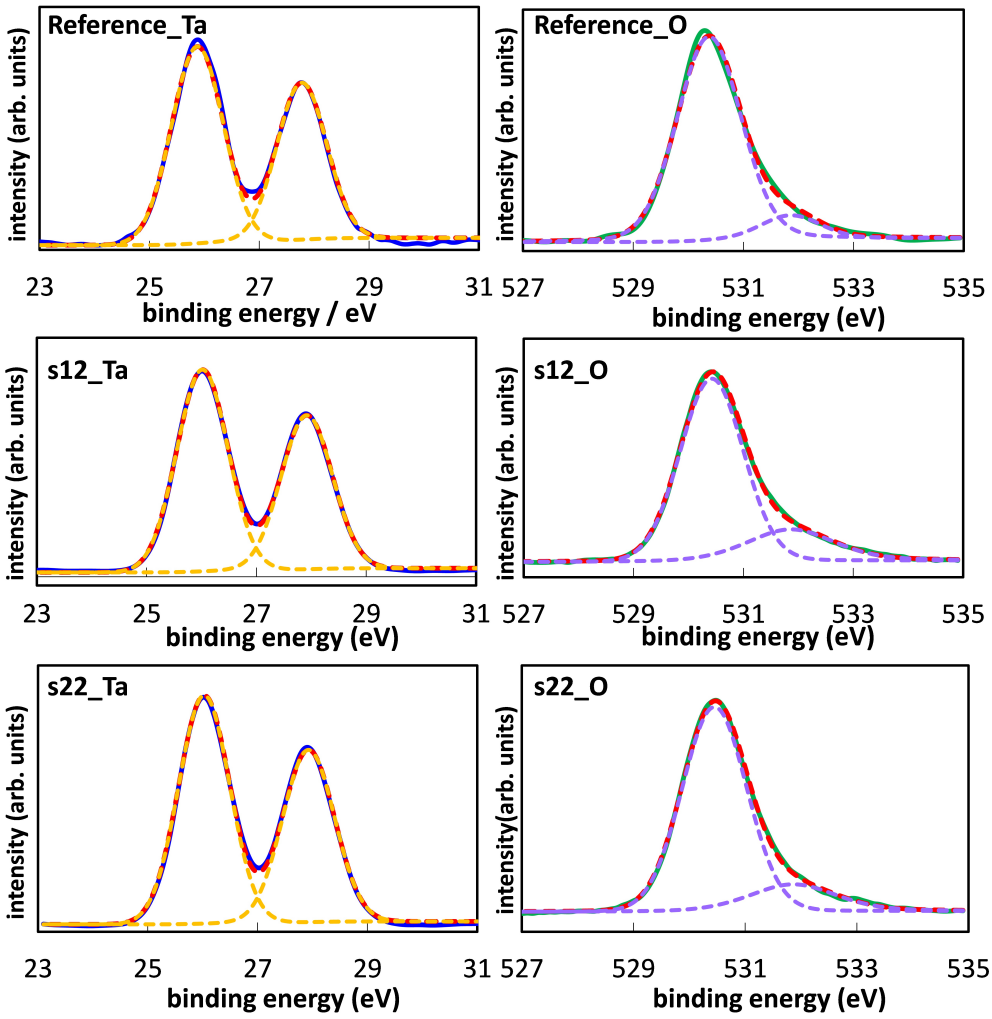


Figure 4.2: Photoelectron spectra of Ta 4*f* and O 1*s* for the as-deposited reference tantala sample, s12, and s22. Solid lines are collected spectra, and dashed lines are composite spectra with decomposed peaks.

Table 4.5: Peak positions from fitting results for Ta 4*f* and O 1*s* peaks.

Sample	Ta 4*f* 5/2 (eV)	Ta 4*f* 7/2 (eV)	O 1*s* (eV)	$O_{surface}$ 1*s* (eV)
Reference	27.9 ± 0.02	26.0 ± 0.03	530.4 ± 0.04	531.9 ± 0.06
s12	27.9 ± 0.03	26.0 ± 0.01	530.4 ± 0.03	531.9 ± 0.02
s22	27.9 ± 0.02	26.0 ± 0.02	530.4 ± 0.01	531.9 ± 0.05

Mechanical Loss

The set of IBS conditions that were selected to assess modifications to mechanical loss include i) variations in the projectile mass, i.e., the mass of the assist ions; ii) variations in the assist ion energy; and iii) variations in the ratio between the number of sputtered particles and the number of assist ions arriving at the substrate surface. The implications these parameters have on surface diffusion are discussed in the next section.

The loss angles of the two control samples c1 and c2 deposited with no assist ion bombardment are similar, 8.5×10^{-4} and 8.4×10^{-4} for c1 and c2, respectively. These values are represented in Figure 4.3-Figure 4.6 by green dotted lines.

The coating's mechanical loss vs ion mass is plotted in Figure 4.3. Samples s13 and s24 were deposited with 100 eV assist ions and similar particle-to-ion arrival ratios, except that the assist ions were Ar^+ for s13 and Xe^+ for s24. The coating's loss angle shows no trend with ion mass within one standard deviation.

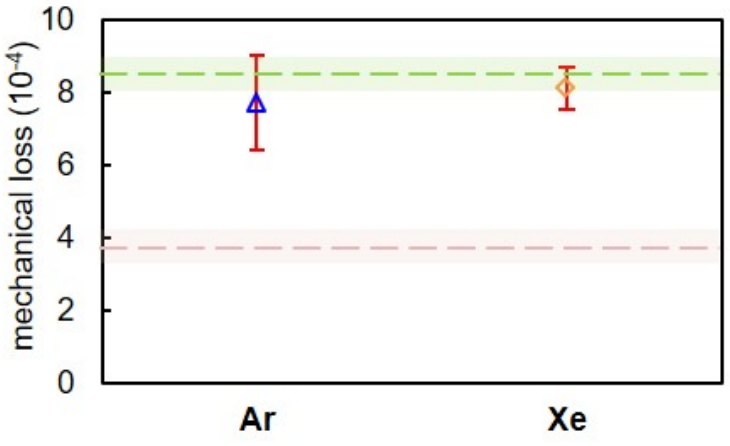


Figure 4.3: Loss angles of samples bombarded by Ar^+ and Xe^+ ions. The ion energy was 100 eV for both samples. The particle-to-ion arrival ratios are almost identical. s13 was bombarded with Ar^+, while s24 was bombarded with Xe^+. The green and red dotted lines represent the loss angle level of the as-deposited control samples and the samples after annealing, respectively. The shading indicates the experimental error.

In Figure 4.4 we compare the loss angles of samples s23 and s24 that were bombarded with Xe^+ of 50 and 100 eV energy and similar particle-to-ion arrival ratios. With higher energy, the Xe^+ were more likely to increase the surface diffusivity of the adsorbed particles and affect the coating's loss angle. Nevertheless, this trend was not observed.

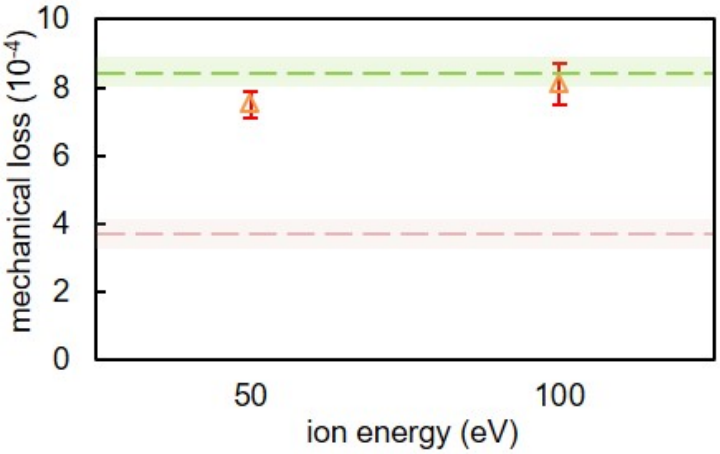


Figure 4.4: Loss angles of tantala coatings bombarded by Xe^+ ions of different energy. The particle-to-ion arrival ratio was kept constant. The assist ion energy was 50 eV for s23 and 100 eV for s24. The green and red dotted lines represent the loss angle level of the as-deposited control samples and the samples after annealing, respectively. The shading indicates the experimental error.

The loss angle of samples bombarded with Ar^+ with different particle-to-ion arrival ratios is shown in Figure 4.5. For s11, s12, and s13, the particle-to-ion arrival ratio decreases from 22/1 to 5/1. Comparison of the coating's loss angles shows no systematic trend with particle-to-ion arrival ratio. Similar behavior of the coating's loss angle is shown in Figure 4.6 for Xe^+ assist bombardment with a particle-to-ion arrival ratio varying from 4/1 to 40/1.

Following these measurements, all tantala thin film samples were annealed. Regardless of the initial loss angle values, for all Ar^+ and Xe^+ bombardment conditions, the annealed tantala samples reached their lowest loss angle of approximately 4×10^{-4}, represented by the red dotted line the Figure 4.3-Figure 4.6, which is in the typical range for annealed tantala films deposited

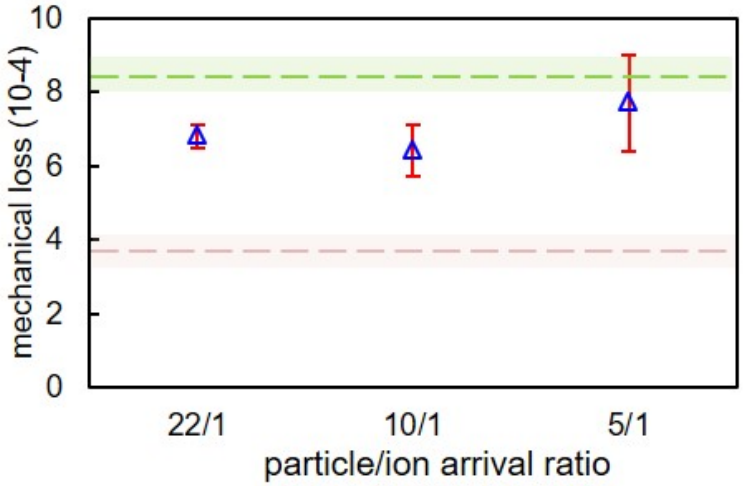


Figure 4.5: Loss angle of tantala coatings bombarded with 100 eV Ar^+ and different particle-to-ion arrival ratios. The green and red dotted lines represent the loss angle level of the as-deposited control samples and the samples after annealing, respectively. The shading indicates the experimental error.

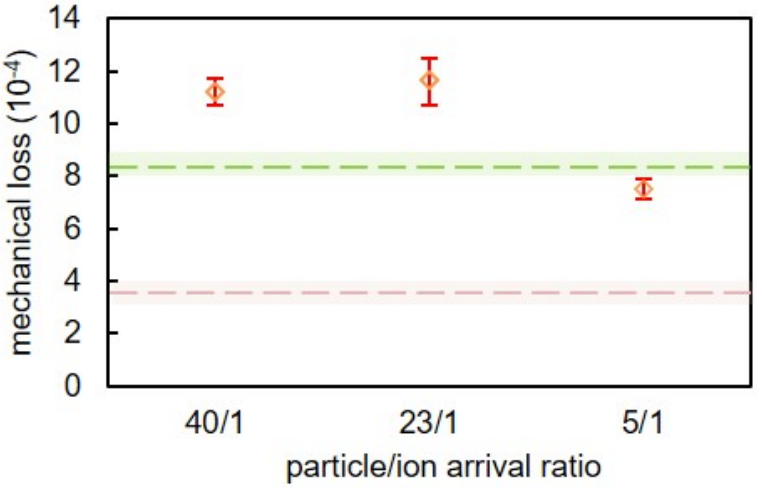


Figure 4.6: Loss angles of tantala coatings bombarded with 50 eV Xe^+ and different particle-to-ion arrival ratios. The green and red dotted lines represent the loss angle level of the as-deposited control samples and the samples after annealing, respectively. The shading indicates the experimental error.

by ion beam sputtering [83]. The decreased loss angle is suggested to correlate with an increase in the medium range order (5-40 Å) during annealing [45, 92].

Discussion

Previous work on diffusion behavior of chemi-sorbed Ge on a Si surface at high temperatures showed that the diffusivity D typically exhibits an Arrhenius behavior under ion bombardment [84, 85], obeying

$$D = \theta D_0 \exp(-E_\alpha / kT) \tag{4.1}$$

where θ is the fractional coverage of mobile adatoms, D_0 is a prefactor for intrinsic surface diffusion, E_a is the activation energy for intrinsic surface diffusion, and T is the temperature. D_0 is a parameter that is empirically correlated to bulk properties, i.e., melting point, cohesive energy and elastic constants [93]. It is also a function of geometrical parameters, i.e., effective jump distance, and jump-attempt frequency [94]. For surface diffusion under ion bombardment, it has been shown that D_0 is affected by ion energy, ion mass, and ion flux, or equivalently with the inverse of the particle-to-ion arrival ratio.

The results of the loss angle of tantala do not vary with ion mass, ion energy, or particle-to-ion arrival ratio, suggesting that surface diffusivity either does not suppress internal friction in IBS tantala or may be hindered by other mechanisms during sputtering at the conditions of the experiments.

In the IBS reactive deposition of tantala, combinations of clusters and atoms with an average energy of several eVs are sputtered from the target and deposit onto the substrate surface. The arriving particles adsorb and diffuse on the surface before bonding with other species. For

O atoms with an activation energy for mass transfer diffusion of approximately 1 eV [95] and a high fractional coverage θ, the diffusivity D would be strongly affected by assist ion bombardment. However, when chemi-sorbed particles are mostly clusters, θ is small. In the best case of the experiments in which the particle-to-ion arrival ratio is 4/1 and assuming no more than one adatom is created by breaking Ta_2O_2 clusters, the maximum ion-induced θ is 0.06. This, coupled with the large activation energy of approximately 2.5 eV for clusters [96], results in insignificant cluster diffusivity, even when considering that the steady-state substrate temperature, T, increases to 130°C during ion bombardment. Theoretically, an assist ion dose ten times larger than that accessible in the present experiments would be needed to increase the number of surface mobile atoms to a level that may affect variations in the coating mechanical loss, if any.

Reduced mobility of the chemisorbed particles is compounded by the limited time there is before the next layer is deposited. An O adatom has only 2 s to diffuse when the deposition rate is that of the experiments, 0.9 Å/s. With an estimated diffusivity D around 10^{-2} nm^2s^{-1} [94], the diffusion length is less than 2 Å at a steady-state temperature of 130°C. Even if one considers that at the location where a 100 eV assist ion impinges a temperature spike that reaches 900°C and lasts 10^{-11} s is produced, the diffusion length of O within such short length scales is less than 0.1 Å. Based on this analysis, we conclude that the surface diffusivity in IBS tantala films induced by assist ion bombardment under the conditions of the experiments is not significant to affect the coating's loss angle. The lack of surface diffusivity can also explain the relatively small variation in coatings' loss angle on high temperature sputtered tantala [83] and its behavior with annealing, which consistently lowered the loss angle to approximately 4×10^{-4} independently of deposition conditions. During a 10 h anneal at 500°C, the diffusion length of

an oxygen atom in the tantala film is around 700 Å, much larger than the few angstroms oxygen can diffuse at the conditions of our experiment.

The diffusion analysis can explain the variation of loss angle with deposition and annealing temperature of a-Si [50]. a-Si thin films deposited at room temperature and post annealed at 400°C have a loss angle of 0.5×10^{-4}. The exact same value was obtained in a-Si thin films deposited at a temperature of 400°C. In this case, surface diffusion and relaxation make it possible to improve the coating's loss angle. This is in contrast with similar experiments in tantala thin films [83], which report a loss angle of 7×10^{-4} for a sample deposited at 400°C and 5×10^{-4} for one deposited at room temperature and annealed at 400°C. Thus, ion bombardment could have an effect similar to high temperature annealing when atomic species are deposited at a rate that ensures surface relaxation before the atoms are buried by the next layer.

Nevertheless, one should note that surface diffusion is not the only factor that plays a role in affecting the room temperature coating mechanical loss. If a reduction in mechanical loss were associated with the restructuring of polyhedra from the face and edge sharing to corner sharing during the annealing process, as recently shown in amorphous Zr doped Ta_2O_5 thin films [7], a significant diffusion length would not be required. The mechanism on how oxygen diffusion would facilitate the reorganization is still unclear. It should also be pointed out that Ta_2O_5 is not an ambient-pressure glass-forming oxide [97] as oxygen coordinates to an average of more than two cations. This, along with the predominant Ta-O ionic bond character [11], forms a structure that is more difficult to modify.

The ion-induced surface diffusivity analysis with low-energy Ar^+ and Xe^+ ions ignores possible surface and bulk modifications due to other mechanisms, such as surface relaxation via viscous flow in the bulk due to displacements produced in the collision cascade process [98].

Along with these effects, there is still mass transport due to the random removal of atoms from the flat surface and the slope- and curvature-dependent sputtering [99]. Experiments with Xe^+ bombardment at a high angle of incidence could allow for more energy deposited at the surface, improving adatom mobility and isolating effects from the bulk.

4.4 Conclusions

To summarize, we investigated the influence of low-energy assist ion bombardment on the mechanical loss of optical quality tantala thin films deposited by reactive IBS. Ar^+ and Xe^+ ion beams were generated at different conditions to identify variations in the coating loss angle due to the mass and energy of the assist ion and ion dose. Most films are of excellent optical quality with an absorption loss at 1064 nm lower than 18 ppm while no preferential sputtering of oxygen by the assist ions was identified. At a microscopic level, the atomic structure of the films was found to be amorphous and the bonding states of Ta remained the same for samples prepared with and without assist ion bombardment. Surface diffusion and its impact on the tantala coating's loss angle were evaluated assuming an Arrhenius behavior. By comparing samples bombarded with Ar^+ and Xe^+, no statistically significant trend in loss angle was observed with ion mass. In the bombardment with Ar^+ or Xe^+ assist ions, the variance in the particle-to-ion arrival ratio did not result in a significant difference in the coating loss angle, either. The influence of assist ion bombardment on coating's loss angle is suggested to be minor.

The lack of evidence in ion-induced diffusivity affecting mechanical loss could be explained by the fact that chemi-sorbed particles are mainly clusters that are essentially immobile with a small proportion of chemi-sorbed adatoms. The adatoms have also insufficient time to rear-

range before being buried by the next layer within the timescales of the deposition process in these experiments.

Chapter 5

Structural Evolution that Affects the Room-Temperature Internal Friction of Binary Oxide Nanolaminates: Implications for Ultrastable Optical Cavities [8]

Internal friction in oxide thin films imposes a critical limitation to the sensitivity and stability of the ultra-high finesse optical cavities for gravitational wave detectors. Strategies like doping or creating nanolaminates are sought to introduce structural modifications that reduce internal friction. This work describes an investigation of the morphological changes SiO_2/Ta_2O_5 and TiO_2/Ta_2O_5 nanolaminates undergo with annealing and their impact on room temperature internal friction. It is demonstrated that thermal treatment results in a reduction of internal friction in both nanolaminates, but through different pathways. In the SiO_2/Ta_2O_5 nanolaminate which layers remain intact after annealing, the total reduction in internal friction follows the reduction in the composing SiO_2 and Ta_2O_5 layers. In contrast, interdiffusion initiated by annealing at the interface in the TiO_2/Ta_2O_5 nanolaminate leads to the formation of a mixed phase. It is the interfacial reaction upon annealing that dictates the more significant reduction

[8] Substantial portions of this chapter have been reproduced with permission from Le Yang, Mariana Fazio, Gabriele Vajente, Alena Ananyeva, GariLynn Billingsley, Ashot Markosyan, Riccardo Bassiri, Martin M. Fejer, and Carmen S. Menoni, *ACS Appl. Nano Mater.*, **2020**, *3*, 12308-12313 [100]. ©2020 American Chemical Society

in internal friction to $\sim 2.6 \times 10^{-4}$, a value lower than any other Ta_2O_5 mixture coating with similar cation concentration.

5.1 Introduction

Nanolaminates (NL) are representative engineered materials that consist of stacks of nanometer thick layers of two or more dissimilar materials. These two-dimensional composite thin films are extensively used in semiconductor devices [101–103], electrochemical storage devices [104], and optical coatings [105, 106]. Their unique properties arise from modifications to the environment of atoms at nanometer to subnanometer scale. For example, in nanolaminates of Al_2O_3/TiO_2 [107] and Al_2O_3/HfO_2 [108] for microelectronics a dielectric constant κ higher than SiO_2 is obtained when the individual layer thickness is reduced to a few nanometers. The large interfacial area between layers also plays a critical role in modifying the structural properties of nanolaminates. In HfO_2/Al_2O_3 [109] and HfO_2/La_2O_3 [110] nanolaminates it is found that the amorphous state of HfO_2 can be stabilized up to 800 °C annealing, an effect created by the increased contribution from surface enthalpy to the total film energy. At the interface, when chemical reactions occur, advantageous functional properties develop, as is the formation of robust Al-O-Ti and Al-O-Zr bonds that inhibit water incorporation in Al_2O_3/TiO_2 [111, 112] and Al_2O_3/ZrO_2 nanolaminates [113]. The improved water anticorrosion is ascribed to the formation of a ternary phase that is thermodynamically more stable than separate phases of the binary oxides [114, 115].

The ability to alter structural properties in nanolaminates has also stimulated great interest for their use in highly reflective mirror coatings of ultrastable optical cavities. High finesse cavities are essential components for precision measurements of time and space, such as atomic

clocks and gravitational wave detectors [116, 117]. For these applications, reducing thermally driven fluctuation is critical to stabilizing the cavity length and thus improving the system's sensitivity. For example, a factor of four reduction in internal friction (Q^{-1}) of the mirror coating in the vicinity of 100 Hz would expand the ability of the Advanced LIGO to detect astrophysical events beyond its present limit, 120 megaparsecs [79, 118, 119]. Nanolaminates are envisioned to replace the high index layers in the current mirror coatings [30,120,121]. The structural modifications associated with the nanolaminate architecture are expected to alter the medium range order and hence the sources of internal friction, which are conceptualized as two-level systems (TLSs) [48]. Experiments on TiO_2/SiO_2 nanolaminates have shown pronounced suppression of internal friction at cryogenic temperatures [44]. This behavior was attributed to the interruption of long scale building blocks associated with TLSs by constraining the layer thickness. In contrast, a direct observation and an unambiguous identification of the structural features that relate to the reduction in room temperature internal friction is still lacking. Identifying and understanding the key structural evolution that governs the internal friction behavior will accelerate the search for coating materials for the next generation gravitational wave detectors.

Herein, we describe the behavior of room temperature internal friction of the SiO_2/Ta_2O_5 and TiO_2/Ta_2O_5 nanolaminates with the goal to identify the origin of internal friction reduction in these amorphous oxide thin films. It is shown that the morphological and structural evolution of the SiO_2/Ta_2O_5 nanolaminate upon annealing is significantly different from that of the TiO_2/Ta_2O_5 nanolaminate. The interfaces between layers remain sharp up to an annealing temperature of 650°C in the SiO_2/Ta_2O_5 nanolaminate. In contrast, interdiffusion in the TiO_2/Ta_2O_5 nanolaminate is revealed by high resolution transmission electron microscopy. In both cases, annealing lowers internal friction compared to a single Ta_2O_5 layer, but from a dis-

tinct origin. The reduction in internal friction of the SiO_2/Ta_2O_5 nanolaminate results from the combined reduction in the individual Ta_2O_5 and SiO_2 nanolayers. In contrast, interdiffusion and formation of a stable ternary phase upon annealing is responsible for the reduction in the TiO_2/Ta_2O_5 nanolaminate.

5.2 Experimental

Nanolaminates of SiO_2/Ta_2O_5 and TiO_2/Ta_2O_5 were prepared by reactive ion beam sputtering using a biased target deposition system [53]. A gridless end Hall ion source was used to generate low energy Ar ions. High purity metal targets were positioned in separate holders that sat symmetrically to the ion source. A negative bias of 800 V applied to the target generated the sputter plum. During the deposition of the nanolaminates, one target at a time was sputtered while the other one was covered by the shutter. Ultra-high purity oxygen gas was introduced to the chamber near the substrate surface to grow oxides. Optimization of the oxygen flow was carried out to ensure stoichiometry ((Table 5.1)). Deposition rates of Ta_2O_5, TiO_2, and SiO_2 were measured to be 0.17, 0.022, and 0.058 Å/s, respectively. The low deposition rates offered high control in layer thickness and interfacial quality when depositing nanometer thick layers. The samples were designed to have a 6 nm top layer of Ta_2O_5 and 15 pairs of 1.6 nm SiO_2 or TiO_2 and 6 nm Ta_2O_5 (Figure 5.1). The stacks were deposited onto substrates by sequentially biasing the corresponding metal targets. For these designs, the cation concentration Si/(Si+Ta) and Ti/(Ti+Ta) was ~ 20 at.% (Appendix B). Reference mixture samples of the same cation concentration were prepared by exposing and sputtering the two targets simultaneously. The mixture cation composition was controlled by varying the target bias time in one period (Table 5.1).

The deposition of each design was repeated multiple times to produce consistent samples for various characterizations.

Table 5.1: Deposition conditions of the nanolaminates.

Nanolaminates		Target bias (V)	Discharge voltage (V)	Discharge current (A)	Oxygen flow (sccm)	Pulse width /pulse period
TiO_2/Ta_2O_5	TiO_2	800	50	5.7	3	62/100
	Ta_2O_5	800	50	5.7	3	62/100
SiO_2/Ta_2O_5	SiO_2	800	50	5.7	3	75/100
	Ta_2O_5	800	50	5.7	3	62/100

Table 5.2: Deposition conditions of the mixtures.

Mixtures		Target bias (V)	Discharge voltage (V)	Discharge current (A)	Oxygen flow (sccm)	Pulse width /pulse period
TiO_2/Ta_2O_5	TiO_2	800	50	5.7	12	2/100
	Ta_2O_5	800	50	5.7	12	53/100
SiO_2/Ta_2O_5	SiO_2	800	50	5.7	12	92/100
	Ta_2O_5	800	50	5.7	12	64/100

The nanolaminate and mixture samples were annealed in air by ramping up the temperature at 1.6°C/min and soaking at the set temperature for 10 h with a Fisher Scientific Isotemp programmable furnace. Soaking temperatures were varied in steps of 100°C up to the highest temperature at which the first sign of crystallization appeared.

The optical absorption loss at 1064 nm for each sample before and after annealing was measured with the photothermal common-path interferomety [55].

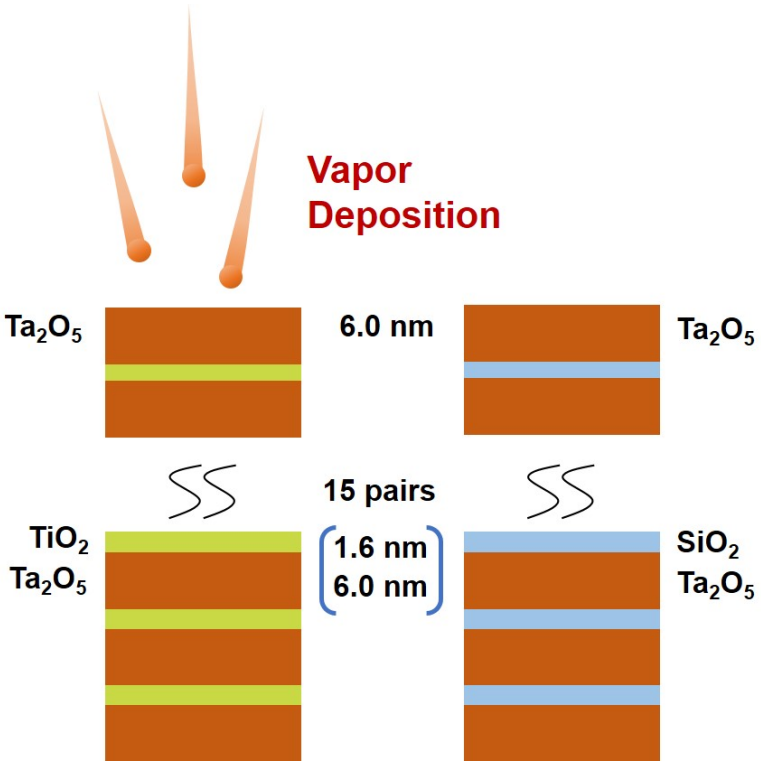


Figure 5.1: Schematic of the nanolaminate samples with a 6 nm top layer of Ta_2O_5 and 15 pairs of 1.6 nm SiO_2 or TiO_2 and 6 nm Ta_2O_5.

The structure evolution with annealing was characterized by grazing incidence x-ray diffraction (GIXRD) using a Bruker D8 thin film diffractometer operated at an incident angle of 0.5°. X-ray photoelectron spectroscopy (XPS) measurements were carried out with a Physical Electronics PE 5800 ESCA/ASE system equipped with a monochromatic Al Kα x-ray source. A take-off angle of 45° was used for all scans. The neutralizer operating at 10 μA was used to counteract the charging effect of the sample. High resolution scans were obtained from the sample surface with no sputtering. The C 1s peak position was used to calibrate the binding energy scale of the spectra. The peak profile was fitted with the Gaussian function. High resolution transmission electron microscopy images of as-deposited and annealed nanolaminates were obtained using a FEI Tecnai Osiris FEG/TEM operated at 200 kV by the EAG Laboratories.

The evaluation of the internal friction for each sample at each annealing stage was performed with a coating ring-down system [51,54,122] by Vajente et al at LIGO laboratory, Caltech. Thin film was deposited on a high quality resonator of fused silica. A gentle nodal suspension was used to support the sample within a vacuum chamber with pressure below 10^{-6} Torr. After exciting the resonant mode at each frequency f_i, the oscillation amplitude was tracked to obtain the decay time τ_i. The internal friction Q_i^{-1} for each mode was then solved through the following relation,

$$Q_i^{-1} = 1/(\pi f_i \tau_i) \tag{5.1}$$

At each frequency, 8 measurements were performed to obtain an averaged Q_i^{-1}. A mean value of Q^{-1} for each sample was then obtained by averaging the Q_i^{-1} over a frequency range of 1-20 kHz.

5.3 Results and Discussion

Figure 5.2a shows the room temperature internal friction of the SiO_2/Ta_2O_5 and TiO_2/Ta_2O_5 nanolaminates for different annealing temperatures. For as-deposited nanolaminates, TiO_2/Ta_2O_5 has a higher $Q^{-1} = (7.5 \pm 0.2) \times 10^{-4}$ than SiO_2/Ta_2O_5 with $Q^{-1} = (6.9 \pm 0.5) \times 10^{-4}$. This is due to as-deposited SiO_2 single layer having low Q^{-1} [42]. Upon increasing the annealing temperature from 400°C to 500°C, the trend is reversed in that Q^{-1} of the TiO_2/Ta_2O_5 is lower than that of the SiO_2/Ta_2O_5 nanolaminate. At 650°C, the internal friction of the TiO_2/Ta_2O_5 nanolaminate reaches its lowest value of $Q^{-1} = (2.6 \pm 0.2) \times 10^{-4}$. At this temperature, Q^{-1} is

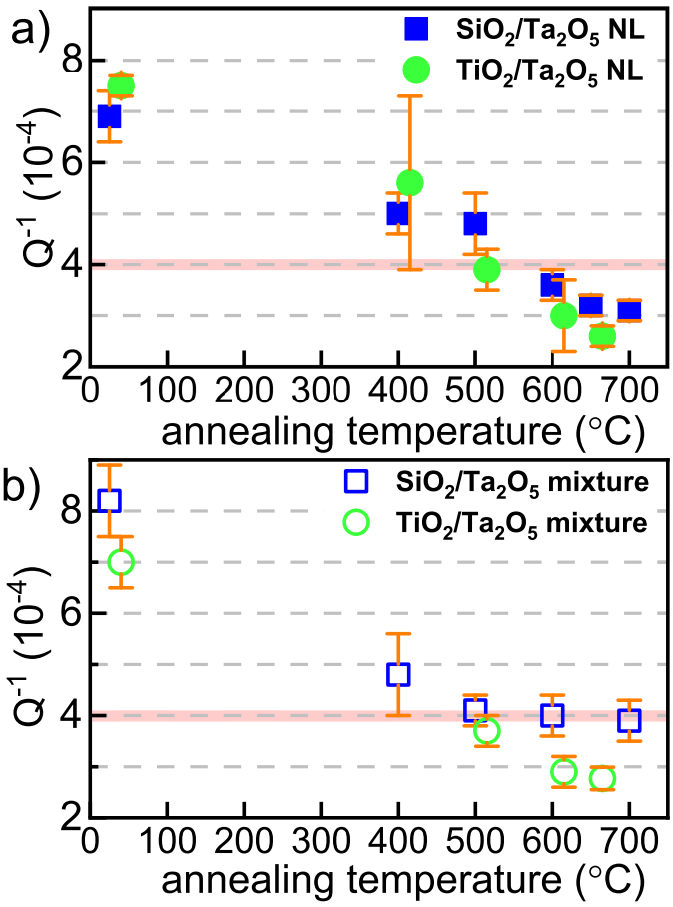


Figure 5.2: a) Room temperature internal friction of nanolaminates as-deposited and annealed at different temperatures. After annealing at 500°C, the TiO_2/Ta_2O_5 nanolaminate has a lower internal friction than the SiO_2/Ta_2O_5 nanolaminate. b) Room temperature internal friction of the SiO_2/Ta_2O_5 and TiO_2/Ta_2O_5 mixtures as-deposited and annealed at different temperatures. The red shading indicates the internal friction level of a single layer Ta_2O_5 annealed at 500°C.

$(3.1 \pm 0.2) \times 10^{-4}$ for the SiO_2/Ta_2O_5 nanolaminate. In both cases, the value is lower than the best value for a single layer Ta_2O_5 annealed at 500°C, $Q^{-1} \approx 4.0 \times 10^{-4}$ [75].

For comparison, Figure 5.2b plots the internal friction of the SiO_2/Ta_2O_5 and TiO_2/Ta_2O_5 mixtures with annealing up to the highest temperature before crystallization. For the SiO_2/Ta_2O_5 mixture, Q^{-1} is $(3.9 \pm 0.4) \times 10^{-4}$ after 700°C annealing. This value is higher than that of the annealed SiO_2/Ta_2O_5 nanolaminate. Phase separation in the SiO_2/Ta_2O_5 mixture after annealing results in a Q^{-1} value similar to that of a single layer Ta_2O_5 (Figure 5.3). Q^{-1}

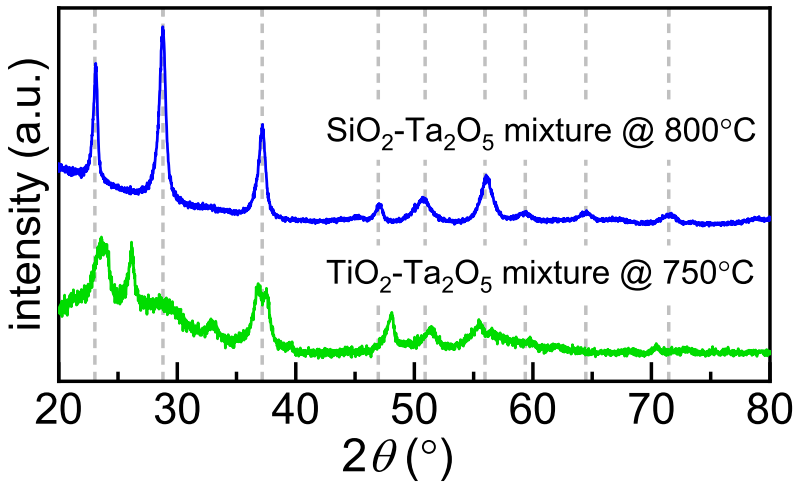


Figure 5.3: GIXRD patterns of crystallized SiO_2/Ta_2O_5 and TiO_2/Ta_2O_5 mixtures after annealing. Phase separation in the annealed SiO_2/Ta_2O_5 mixture is identified with the crystallized phase being orthorhombic Ta_2O_5. A ternary phase of $TiTa_{18}O_{47}$ is identified in the TiO_2/Ta_2O_5 mixture after annealing.

is the same within experimental errors for the TiO_2/Ta_2O_5 nanolaminate and mixture after annealing at 650°C, indicating a strong similarity. In both the mixture and nanolaminate form, the TiO_2/Ta_2O_5 system exhibits lower internal friction than the SiO_2/Ta_2O_5 one.

The optical absorption loss at 1064 nm for each nanolaminate was measured as deposited and after annealing at 650°C. The as-deposited TiO_2/Ta_2O_5 nanolaminate has an absorption loss of 5.5 ± 0.2 ppm, which then reduces to 3.5 ± 0.2 ppm after annealing at 650°C. For the SiO_2/Ta_2O_5 nanolaminate, the absorption loss for as-deposited and annealed sample is 4.6 ± 0.5 ppm and 4.0 ± 0.6 ppm, respectively.

There are significant differences in the structural evolution of the nanolaminates upon annealing that affect the internal friction behavior. The high resolution TEM images of the as-deposited SiO_2/Ta_2O_5 (Figure 5.4a) and TiO_2/Ta_2O_5 (Figure 5.4c) nanolaminates show well defined layers with sharp interfaces. Upon annealing at 650°C, the SiO_2/Ta_2O_5 nanolaminate remains unchanged (Figure 5.4b), showing intact interfaces between strongly contrasted SiO_2 and Ta_2O_5 layers. In this case, the Q^{-1} can be approximated as the weighted average of the internal

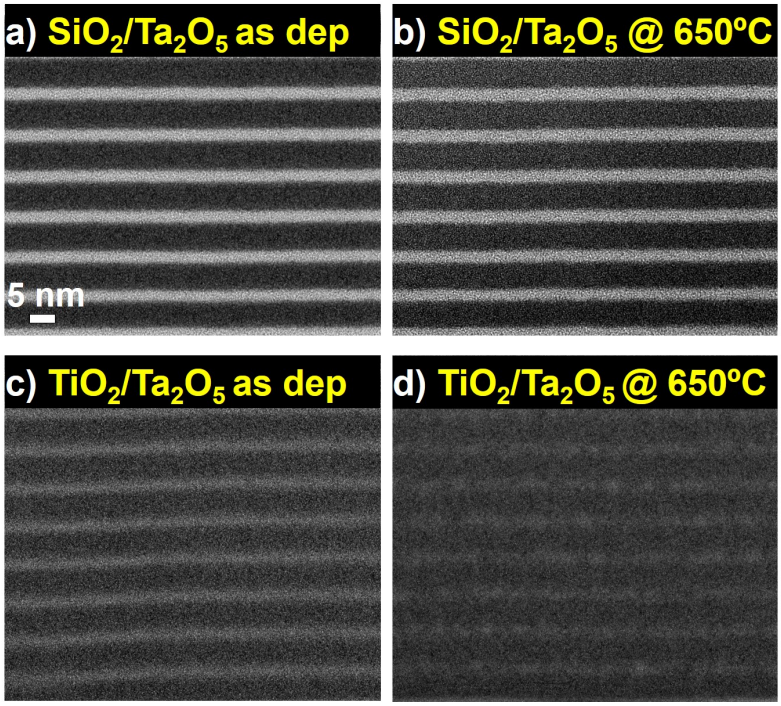


Figure 5.4: High resolution cross-sectional TEM images of nanolaminates before and after annealing at 650°C. a) SiO_2/Ta_2O_5 nanolaminate with robust layer structure before annealing, b) SiO_2/Ta_2O_5 nanolaminate with intact layer structure after annealing at 650°C, c) TiO_2/Ta_2O_5 nanolaminate with distinct layer interface before annealing, d) TiO_2/Ta_2O_5 nanolaminate showing interface blurring after annealing 650°C.

friction of the composing oxide layers (disregarding any interfacial effects) [41, 123]. This calculation estimates $Q^{-1} \approx 3.4 \times 10^{-4}$, which is in good agreement with the measured value. On the contrary, a noticeable discontinuity along the interfaces and homogenization of the two oxide materials are found in the annealed TiO_2/Ta_2O_5 nanolaminate (Figure 5.4d).

Full crystallization of the TiO_2/Ta_2O_5 and SiO_2/Ta_2O_5 nanolaminates is observed after annealing at 750°C and 800°C, respectively. The crystallization process is delayed to a higher annealing temperature in both nanolaminates compared to 675°C, the crystallization temperature of a single layer Ta_2O_5 [75]. The amorphous phase is stabilized to higher temperature due to a greater contribution from the surface enthalpy to the total Gibbs free energy change for the amorphous-to-crystalline transition [109, 120, 124]. Diffraction patterns of the crystallized

nanolaminates and the crystallized Ta_2O_5 single layer are shown in Figure 5.5. The spectrum of the crystallized SiO_2/Ta_2O_5 nanolaminate only exhibits diffraction peaks from the orthorhombic Ta_2O_5 phase [125] while no SiO_2 peak is found. The peaks feature a much broader profile than that of a single layer Ta_2O_5. Applying the Scherrer equation [126] to the peak at $2\theta = 28.7°$, the crystallite size in the SiO_2/Ta_2O_5 nanolaminate is calculated to be ~ 4.9 nm, while a size of 35.1 nm is calculated for the single layer Ta_2O_5. The crystallite size of 5 nm is fully consistent with the Ta_2O_5 layer thickness ~ 6 nm, indicating the physical constraint to crystallite growth imposed by the interfaces. The same analysis of the TiO_2/Ta_2O_5 nanolaminate yields a crystallite size of 11.2 nm that is larger than the layer thickness. The extended growth is only possible when bi-directional diffusion across the interface bridges the separated Ta_2O_5 layers.

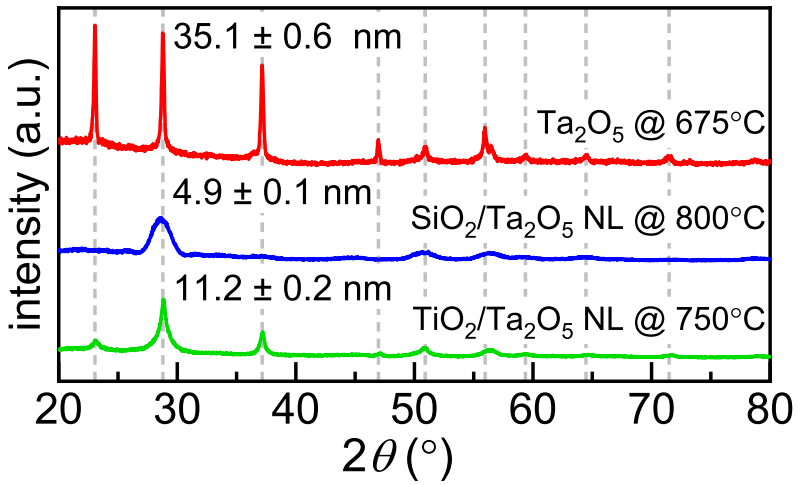


Figure 5.5: Diffraction patterns of the SiO_2/Ta_2O_5 nanolaminate annealed at 800°C (blue line) and the TiO_2/Ta_2O_5 nanolaminate annealed at 750°C (green line) after crystallization. For comparison, the diffraction spectrum of a crystallized Ta_2O_5 single layer annealed at 675°C is shown on top (red line).

The emergence of Ti 2p peaks in the XPS spectrum confirms a strong Ti cation diffusion into the top Ta_2O_5 layer in the TiO_2/Ta_2O_5 nanolaminate upon annealing (Figure 5.6). In contrast, a

Si 2p peak is almost absent in the XPS spectrum of both as-deposited and annealed SiO_2/Ta_2O_5 nanolaminate. Si cation diffusion into the Ta_2O_5 layer upon annealing is not identified.

Figure 5.7 shows the Ti 2p core level in the TiO_2/Ta_2O_5 nanolaminate after annealing at 650°C. The peak separation is determined to be 5.85 ± 0.02 eV, which is significantly different from 5.7 eV for Ti in a TiO_2(IV) environment [127]. The change in the peak separation is ascribed to the change of the Ti bonding as previously shown [43], and indicates an atomic mixture. The mixing of TiO_2 and Ta_2O_5 in this sample is similar to what has been observed in a TiO_2/Ta_2O_5 mixture upon annealing, which leads to the formation of a ternary compound identified as $TiTa_{18}O_{47}$ that is thermodynamically more stable than separate phases of TiO_2 and Ta_2O_5 [43]. The existence of a stable ternary phase between oxides in nanolaminates has been well demonstrated in systems such as Al_2O_3/TiO_2 [111, 112] and Al_2O_3/ZrO_2 [113, 115], where the presence of the mixed phase gives superior physical and/or chemical properties that can be used in various applications. In the absence of a stable ternary phase, a cross-interface diffusion of oxides between layers should not occur as it will not lead to a reduction in Gibbs free energy for the whole system. Such picture is supported by the observation of well-spaced layers after annealing in the SiO_2/Ta_2O_5 (Figure 5.4) and SiO_2/TiO_2 [44] nanolaminates.

These results show that in these binary oxide systems, the more significant reduction in room temperature internal friction is dominated by the formation of a stable mixed phase rather than the effect of nanolayering of the two oxide materials. For the TiO_2/Ta_2O_5 nanolaminate, it is the reorganization that occurs during the mixing that has a major influence on reducing the room temperature internal friction. Elevated annealing temperature in the SiO_2/Ta_2O_5 nanolaminate improves the internal friction with respect to a single layer Ta_2O_5 due to a reduction of internal friction in both the SiO_2 and Ta_2O_5 layers. The internal friction of a SiO_2

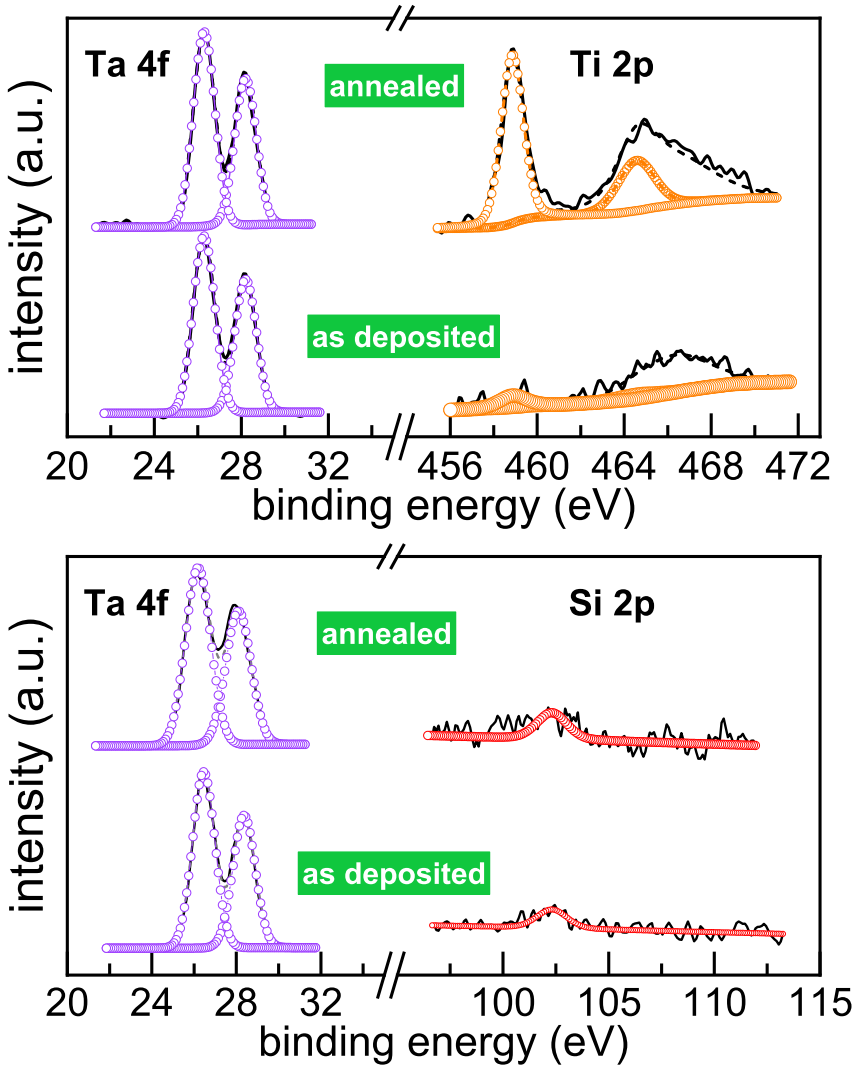


Figure 5.6: X-ray photoelectron spectra for as-deposited and annealed nanolaminates. Top, Ta 4f and Ti 2p peaks for the TiO_2/Ta_2O_5 nanolaminate as deposited and after annealing at 650°C. The emergence of Ti 2p peaks after annealing indicates a significant Ti cation diffusion into the top Ta_2O_5 layer. Bottom, Ta 4f and Si 2p peaks for the SiO_2/Ta_2O_5 nanolaminate as deposited and after annealing at 650°C. A negligible amount of Si is present in the top Ta_2O_5 layer before and after annealing. The peak area ratio between the Ta 4f and Si 2p peaks remains constant for as deposited and annealed samples.

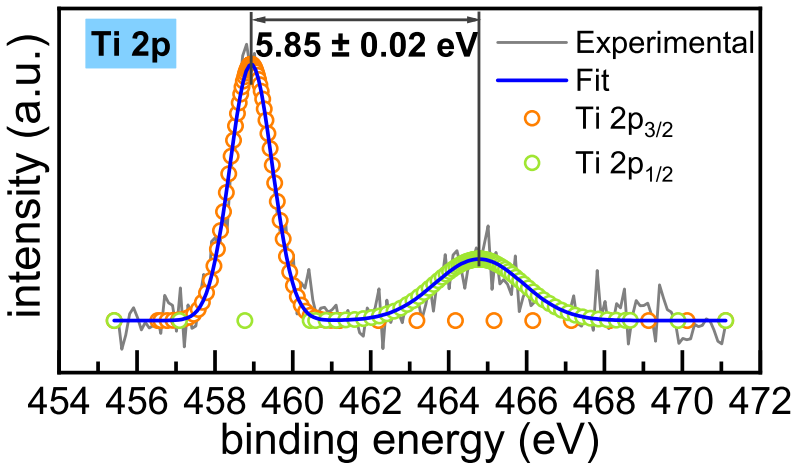


Figure 5.7: X-ray photoelectron spectrum of Ti 2p in the TiO_2/Ta_2O_5 nanolaminate after annealing at 650°C. The peak separation is determined to be 5.85 ± 0.02 eV.

layer after annealing reaches $Q^{-1} \approx 0.5 \times 10^{-4}$ that is the lowest value among all binary oxide films [42, 128]. Yet the reduction is not as profound as from mixing in the TiO_2/Ta_2O_5 nanolaminate. This behavior is different from what has been observed for the cryogenic internal friction of SiO_2/TiO_2 nanolaminates, which manifests itself by a decrease in internal friction with a decrease in layer thickness [44]. Such effect is ascribed to the elimination of two-level system transitions with characteristic dimensions that exceed the layer thickness. At room temperature, however, contribution from those cryogenic two-level systems to the internal friction is negligibly small [129] so that the effect from nanolayering does not lead to lower internal friction. On the contrary, observation of the structural evolution in the TiO_2/Ta_2O_5 nanolaminate with annealing suggests that the formation of a more stable phase might result in the modified distribution of two-level systems that is responsible for lowering the room temperature internal friction. During the mixing process, significant atomic rearrangements might contribute to increasing the atomic order at the medium range, which has been found to be correlated with the improved internal friction for oxides such as the Ta_2O_5/ZrO_2 mixture [7].

5.4 Conclusions

An unambiguous identification of the morphological changes that involve layer breakup and mixture formation in the TiO_2/Ta_2O_5 nanolaminate is demonstrated. The mixing of TiO_2 and Ta_2O_5, which is thermodynamically favored upon annealing, results in the major improvements in the room temperature internal friction of the TiO_2/Ta_2O_5 nanolaminate. In the absence of mixing, the reduction in room temperature internal friction of a nanolaminate with annealing can be predicted from the changes in the composing layers, as is the case of the SiO_2/Ta_2O_5 nanolaminate. A modified distribution of two-level systems in the mixed phase rather than size effects is argued to be responsible for the more profoundly reduced room temperature internal friction in the TiO_2/Ta_2O_5 nanolaminate. These results highlight the different morphological changes with annealing in nanolaminates and their effects on the room temperature internal friction, providing more insights into the selection of coating materials for the next generation gravitational wave detectors.

Chapter 6

Enhanced Medium Range Order in Vapor Deposited Germania Glasses at Elevated Temperatures[9]

Glasses are nonequilibrium solids with properties highly dependent on their method of preparation. It is established that in vapor-deposited molecular glasses structural organization and properties could be readily tuned with deposition rate and substrate temperature. In contrast, it has not yet been demonstrated whether the atomic packing of strong network forming glasses such as GeO_2 could be modified at short and medium range (< 2 nm) through vapor deposition at elevated temperatures. In this work, we show that the structure of amorphous GeO_2 (a-GeO_2) characterized by GeO_4 tetrahedra connected in rings of various sizes evolves into a more ordered configuration containing an increased population of 6-membered rings when vapor deposited at elevated temperatures. It is also demonstrated that deposition near the glass transition temperature (T_g) is more efficient than post-growth annealing in modifying the atomic organization at medium range, as expected from an ultrastable glass behavior. The fingerprints of the more ordered configuration correlate with the internal friction of a-GeO_2 which decreases by as much as 44% when deposited at 0.83 T_g. In combination, these results show a strong correlation between medium range order and internal friction as predicted by theory. Identifying the microscopic origin of internal friction in amorphous oxides is

[9]Substantial portions of this chapter have been reproduced with permission from Le Yang, Gabriele Vajente, Mariana Fazio, Alena Ananyeva, GariLynn Billingsley, Ashot Markosyan, Riccardo Bassiri, Martin M. Fejer, and Carmen S. Menoni, submitted [130].

paramount to designing ultrastable coatings for mirrors of the end test-masses of gravitational wave interferometers, in which the coatings' internal friction is a main source of noise limiting their sensitivity.

6.1 Introduction

Glasses are nonequilibrium amorphous solids that retain in their structure at short and medium range (< 2 nm) information about the history of preparation [20, 131]. For melt-quenched glasses, a slow cooling rate towards the glass transition temperature (T_g) allows for an adequate configurational sampling that drives the system to lower energy states in the potential energy landscape. Physical vapor deposition (PVD) is an efficient means of rapid cooling to produce glassy materials. Altering the deposition conditions, such as substrate temperature (T_{sub}) and deposition rate, makes it possible to manipulate the atomic ordering that in turn shapes the properties of the vapor-deposited glasses [15, 19, 132, 133]. For example, in vapor-deposited thin films of itraconazole, a glass-forming smectic liquid crystal, the orientation of the molecule's long axis tends to align with the surface normal when the deposition rate is around 0.2 Å/s, whereas nearly isotropic orientation is preferred when the deposition rate is 3 orders of magnitude higher [14]. In a similar fashion, the substrate temperature plays a role in affecting the molecular packing in thin-film organic glasses. Depositing *N*,*N*'-bis(3-methylphenyl)-*N*,*N*'-diphenylbenzidine at around 0.8 T_g produces glasses with a strong horizontal orientation, while at 0.95 T_g weak vertical orientation is observed [15, 16]. It remains to be answered whether or not the atomic packing of strong network-forming glasses, such as a-SiO_2 and a-GeO_2, could be modified by altering the substrate temperature, since restructuring of strong covalent bonds is involved. *In silico* vapor deposition of glasses predicts that when de-

positing at the Kauzmann temperature, where the configurational entropy vanishes, it would be possible to achieve a uniform structural configuration characteristic of ultrastable glassy materials [134].

A further question that follows is whether elevated temperature deposition would result in an atomic configuration that reduces two-level systems (TLS) induced by structural relaxation in glassy materials. Recent insights into the properties of vapor-deposited glasses show that TLS, which arise from atomic disorder, could possibly be eliminated at selected deposition condition [131]. In indomethacin thin film glasses grown at 0.85 T_g, a remarkable suppression of TLS was found due to the particular molecular arrangement influenced by the deposition condition [29]. For network forming glasses such as a-Si, the density of TLS has been shown to reduce by at least one order of magnitude when the substrate temperature increased from 473 K to 673 K T_g [27, 28]. This behavior has been ascribed to a more ordered amorphous network achieved with elevated temperature deposition. Motivated by these results, the gravitational wave community has explored the possibility to lower the density of TLS through elevated temperature deposition of a-Ta_2O_5 as a way to reduce internal friction (Q^{-1}) in the coatings of the end test mass mirrors [30,83]. Internal friction in amorphous materials originates from the coupling of an ensemble of TLS with an elastic field [24,25]. This coupling leads to thermally driven fluctuations that limit the sensitivity of gravitational wave detectors [51, 79, 118]. Recent work in a-Si thin films has demonstrated that the internal friction was substantially reduced by 75% when the substrate temperature increased from 293 K to 673 K($\sim$ 0.8 T_g) [50]. Nevertheless, a precise correlation between structural organization and internal friction for strong network forming glasses deposited at elevated substrate temperature is still lacking.

Herein, we describe the modifications in the atomic configuration of a-GeO_2 thin films vapor deposited at elevated substrate temperatures. The lower T_g of GeO_2, around 788 K [135], in comparison with T_g around 1475 K for SiO_2 [136] makes the deposition at $T_{sub} \sim T_g$ accessible. The signatures of structural ordering, obtained from Raman spectroscopy, distinctively show the arrangement of GeO_4 tetrahedra into 6-membered rings increases at the expense of 3-membered rings when depositing at elevated substrate temperatures. It is also demonstrated that the deposition near T_g is more efficient than post-growth annealing in modifying the atomic structure at medium range, as expected from an ultrastable glass behavior. These structural modifications correlate with internal friction of the a-GeO_2 thin films, which decreases by as much as 44% when the film is deposited at 0.83 T_g. In combination the results demonstrate a strong correlation between medium range order and internal friction as predicted by theory.

6.2 Experimental

Deposition of a-GeO_2 Thin Films

a-GeO_2 thin films were deposited with a 4Wave LANS physical vapor deposition system [53, 100]. A gridless ion source was used to generate low energy Ar ions that were accelerated towards a high purity Ge target negatively biased at 800 V. This created a sputter plume that deposited onto the substrate. Oxidation was achieved by flowing 6 sccm of oxygen near the substrate surface. For high temperature deposition, a heating lamp was positioned under the rotating substrate stage. The stage temperature was increased to the set point 10 minutes before deposition for equilibration purposes and maintained through the process. The rate for

room temperature and high temperature deposition was kept at 1.1 and 1.2 Å/s, respectively. The use of approximately the same deposition rate ruled out the influence of this parameter in atomic reorganization.

Thermal annealing of each sample after deposition was carried out at ambient conditions using a Fisher Scientific Isotemp muffle furnace. The process includes ramping up the temperature by 100 K/h and soaking the sample at each set temperature for 10 h.

Raman Scattering of a-GeO_2 Thin Films

Raman scattering was performed with a Horiba LabRAM HR Evolution Spectrometer. A frequency doubled Nd:YAG laser of 532 nm wavelength and 10 mW average power was used for excitation. The laser beam was focused onto the sample's surface using a ×100 objective. Three spectra of 60 seconds acquisition time were collected for each sample and averaged to improve signal to noise. Deconvolution of the peaks in the Raman spectrum was carried out by fitting the peaks with Gaussian lineshapes.

Internal Friction Measurements

Internal friction (Q^{-1}) of the a-GeO_2 thin films was measured with a ring down system [54, 122]. The ~ 500-nm-thick a-GeO_2 samples for this purpose were deposited on high quality fused silica disk of 75-mm diameter and 1-mm thickness. A gentle nodal suspension method was used to support the sample inside a vacuum chamber held at a pressure below 10^{-6} Torr. After exciting the resonant mode, the oscillation amplitude at each frequency f_i was tracked to obtain the decay time τ_i. The internal friction Q_i^{-1} for each mode was then computed through the following relation,

$$Q_i^{-1} = \frac{1}{\pi f_i \tau_i} \tag{6.1}$$

At each frequency, 8 measurements were performed to obtain an averaged Q_i^{-1}. A mean value of Q^{-1} for each sample was then obtained by averaging the Q_i^{-1} over a frequency range of 1-20 kHz.

6.3 Results and Discussion

The physical vapor deposition of amorphous oxides is characterized by hit and stick processes in which the atomic relaxation and formation of a more stable structure are constrained when the substrate temperature is low. Elevated T_{sub} and post-deposition annealing alter the organizational state of the deposited glasses by enabling the system to explore nearby lower minima in the energy landscape through atomic rearrangements. For a-GeO_2 that has strong directional covalent bonding, the most dominant structural order is at the medium range, which can be defined in terms of the connection of the tetrahedra [2,137,138]. The (Ge-O-Ge) connection chain has a ring shape with a size that is determined by the number of Ge atoms within the closed path. Rings of various sizes ranging from 3 to 10 with a maximum distribution around 6-membered rings are predicted by models of a-GeO_2 [3]. This structural information can be obtained from x-ray and neutron diffraction in combination with modeling [3, 139], or alternatively from Raman spectroscopy that is sensitive to local vibration at the medium range in glasses.

The Raman spectra of a-GeO_2 thin films, shown in Figure 6.1, are characterized by strong peaks at 420 cm^{-1} and 516 cm^{-1}. The former corresponds to the symmetric stretching of bridg-

ing oxygen in 6-membered rings [5] and the latter corresponds to the oxygen-breathing mode associated with 3-membered rings [57, 58]. We therefore use the ratio between the areas of the peaks corresponding to 6 and 3-membered rings, A_6/A_3, to characterize the ring distribution in a-GeO_2 samples. Figure 6.1a and Figure 6.1b qualitatively contrast the difference in the ring distribution of a-GeO_2 samples deposited at T_{sub} = room temperature and $T_{sub} = 0.83\ T_g$, which indicates that high temperature deposition favors a larger fraction of 6-membered rings, i.e., a more ordered structure, as described below.

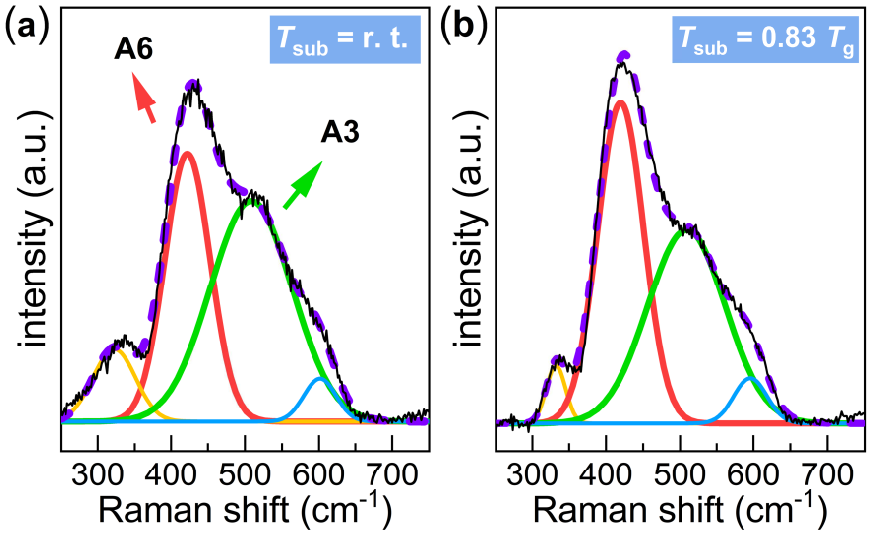


Figure 6.1: Raman scattering spectra of a-GeO_2 thin films deposited at (a) T_{sub} = room temperature deposited and (b) T_{sub} = 0.83 T_g. The red peak at 420 cm^{-1} corresponds to the symmetric stretching of bridging oxygen in a 6-membered ring. The green peak at 520 cm^{-1} corresponds to the breathing motion of bridging oxygen in a 3-membered ring. The yellow peak at 333 cm^{-1} is possibly due to Ge motion within the network. The blue peak at 595 cm^{-1} is assigned to Ge-O-Ge bending modes [57, 58]

We focus first on the evolution of ring distribution in a-GeO_2 as the system approaches lower energy states with post-deposition annealing, visualized as changes in A_6/A_3 in Figure 6.2. A_6/A_3 undergoes a 6% increase from 0.68 ± 0.02 to 0.72 ± 0.02 after the first annealing step at annealing temperature T_{an} = 573 K and a more pronounced 46% increase to 1.03 ± 0.05 after

the annealing at T_{an} = 623 K. Annealing to higher temperature continues to relax the atomic structure, leading to an increase of A_6/A_3 to 1.20 ± 0.12. It needs to be pointed out that the increase in A_6/A_3 comes from both the increase in A_6 and the decrease in A_3, which is confirmed by comparing to a reference peak from the substrate in the Raman spectrum. Overall, the trend illustrates that the population of small rings decreases, whereas that of 6-membered rings increases with thermal annealing. The breakup of small rings of threefold or fourfold rings could be attributed to heavily strained intertetrahedral bridging bonds [6, 140]. The increase in the population of 6-membered rings indicates that an increased medium range order is achieved in a-GeO_2 thin films upon annealing.

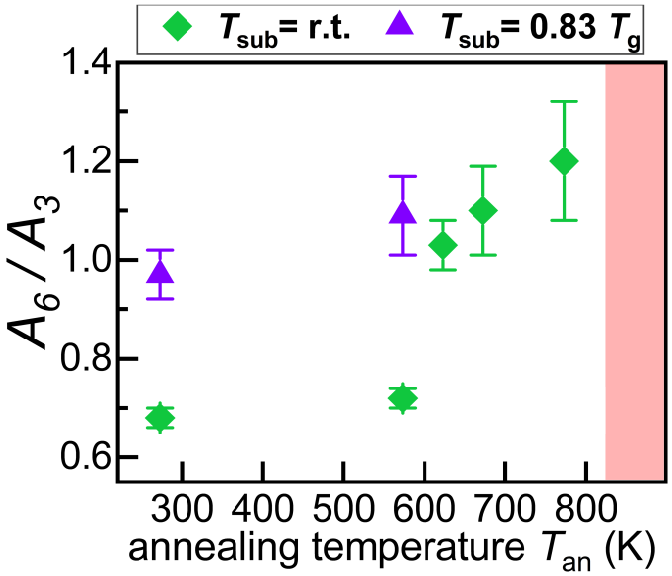


Figure 6.2: Structural relaxation with annealing characterized by the A_6/A_3 ratio for a-GeO_2 thin films deposited at T_{sub} = room temperature (green) and T_{sub} = 0.83 T_g (purple). The red shaded region in the figure indicates the start of crystallization. (Appendix C)

Deposition at elevated T_{sub} brings more significant changes to the ring distribution in a-GeO_2, as shown in Figure 6.2. A_6/A_3 is 0.97 ± 0.05 for the sample deposited at T_{sub} = 0.83 T_g, and 0.68 ± 0.02 for the sample deposited at T_{sub} = room temperature. The larger fraction of

6-membered rings confirms the formation of a more ordered atomic structure at elevated T_{sub}. Moreover, the results show that the annealing temperature required to achieve the high medium range order before crystallization, identified by $A_6/A_3 \approx 1.1$, is lower at $T_{an} = 580$ K, when a-GeO_2 is deposited at $T_{sub} = 0.83\ T_g$, in comparison to $T_{an} = 673$ K for the a-GeO_2 deposited at T_{sub} = room temperature. During room temperature deposition, incident sputtered particles rapidly lose their energy to the substrate before exploring the entire configuration space [141], whereas elevated substrate temperature promotes a larger sampling that leads to a higher degree of organization. It is through elevated substrate temperature that vapor-deposited glasses are able to achieve a structural organization that resembles that of an ultrastable glass [134].

The structural rearrangements at medium range are key to lowering the potential energy of the glass system, and are strongly dependent on the substrate temperature, as recently shown in molecular dynamics simulations of vapor-deposited a-SiO_2 films [142]. In comparison to a-SiO_2 films deposited at T_{sub} far away from T_g, the films with low potential energy prepared at the optimal T_{sub} near T_g have a higher fraction and a narrower distribution of rings more centered at 6-membered rings, suggesting a greater structural uniformity. This behavior, observed in a-GeO_2 as well, is characteristic of stable glasses prepared at the optimal substrate temperature as predicted by vapor deposition simulations [134].

The effect of increased medium range order on modifying TLS in a-GeO_2 is assessed from internal friction Q^{-1} of thin films deposited at different T_{sub} and post-deposition annealed. Previous modeling of oxides, such as a-Ta_2O_5, has identified that an increased medium range order correlates with the reduction in Q^{-1} [45]. The evolution of Q^{-1} for a-GeO_2 deposited at T_{sub} = room temperature with annealing is shown in Figure 6.3a. The as-prepared a-GeO_2 thin film has Q^{-1} of $(2.98 \pm 0.27) \times 10^{-4}$, which reduces to $(2.56 \pm 0.52) \times 10^{-4}$ after the first

annealing step at T_{an} = 573 K. A significant decrease by 49% is obtained after the T_{an} = 623 K annealing step. Notably, the annealing temperature T_{an} after which Q^{-1} undergoes a sharp decrease coincides with the turning point in the increase of A_6/A_3 ratio in Figure 6.2. Beyond T_{an} = 673 K, Q^{-1} plateaus at a value of $(1.00 \pm 0.13) \times 10^{-4}$.

Comparison of Q^{-1} for as-prepared a-GeO_2 deposited at T_{sub} = room temperature, T_{sub} = 0.60 T_g, and T_{sub} = 0.83 T_g shows a steady decrease with an increase in T_{sub}. The a-GeO_2 sample deposited at 0.83 T_g has the lowest $Q^{-1} = (1.66 \pm 0.14) \times 10^{-4}$, which is 44% less than Q^{-1} of the sample deposited at room temperature. Figure 6.3 shows a reduction in Q^{-1} with annealing for all samples, although the rate at which Q^{-1} reaches the plateau is different for each one. The a-GeO_2 thin film prepared at T_{sub} = 0.60 T_g reaches 1.00×10^{-4} after annealing at T_{an} = 623 K, yet the one prepared at T_{sub} = 0.83 T_g achieves this Q^{-1} after annealing at T_{an} = 573 K. Annealing beyond T_{an} = 623 K does not decrease Q^{-1} below 1.00×10^{-4} for the high temperature grown samples. It is also worth noting that the a-GeO_2 thin film deposited at T_{sub} = 0.60 T_g (473 K) without thermal treatment has $Q^{-1} = (2.39 \pm 0.15) \times 10^{-4}$, which is comparable to Q^{-1} = (2.56 $\pm$ 0.52) $\times 10^{-4}$ for the sample deposited at T_{sub} = room temperature and annealed at T_{an} = 573 K for 10 hours. Considering that the same Q^{-1} is obtained at a lower T_{an} during a significantly shorter deposition time of around 1 hour compared to the annealing for 10 hours, it indicates a higher efficiency of elevated temperature deposition over annealing for reducing Q^{-1} of a-GeO_2 thin films.

The inverse relationship of Q^{-1} with A_6/A_3 in Figure 6.4 demonstrates a strong correlation between lowering Q^{-1} and increasing medium range order characterized by a larger fraction of 6-membered rings in a-GeO_2. Such observation echoes what has been found for vapor-deposited a-SiO_2 in Ref [128], where a steady decrease in the population of 3-membered rings

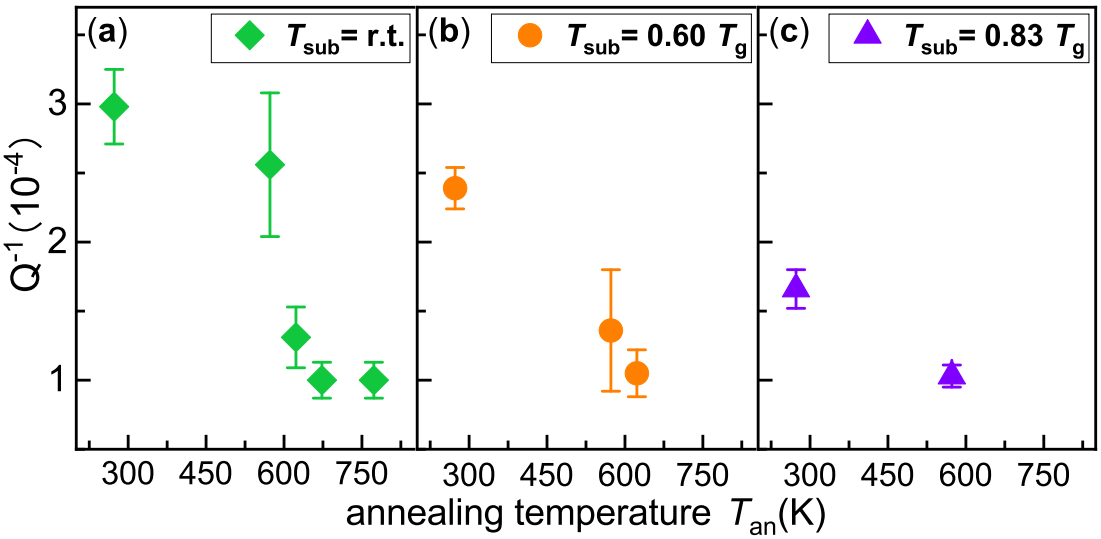


Figure 6.3: Internal friction Q^{-1} of a-GeO_2 thin films deposited at (a) T_{sub} = room temperature (green), (b) T_{sub} = 0.60 T_g (orange), and (c) T_{sub} = 0.83 T_g (purple). The annealing temperature to reach the lowest internal friction is T_{an} = 673 K, T_{an} = 623 K, and T_{an} = 573 K for samples deposited at T_{sub} = room temperature (green), T_{sub} = 0.60 T_g (orange), and T_{sub} = 0.83 T_g (purple), respectively.

is linked to the reduction in Q^{-1} during extended annealing. Similar behavior has also been observed in Ref [7], in which analyses of grazing-incidence pair distribution functions of ZrO_2-doped Ta_2O_5 reveal a systematic change in the medium range order with annealing temperature. Modeling shows that the atomic rearrangements involve a decrease in the population of edge- and face-sharing polyhedra and an increase in corner-sharing ones, which agree with an expansion in the polyhedral connection ring. These modifications correlate with a steady decrease in Q^{-1}. Further evidence directly linking the structural changes with TLS for ZrO_2-doped Ta_2O_5 is obtained from Ref [49]. In this work, the energy landscape of ZrO_2-doped Ta_2O_5 was explored by searching for TLS using molecular dynamics simulations. It is found that the TLS can be sorted into two types depending on whether the cation-oxygen bond within the polyhedron breaks, namely cage-breaking and non-cage breaking transitions. The simulations show that a significant number of TLS from cage-breaking events are responsible for room temperature Q^{-1} in the amorphous oxide. Elimination of such transitions by expanding the polyhedral

connections, i.e., increasing the ring size, would thus result in lower Q^{-1}. In combination, these theories provide a consistent interpretation of the correlation between Q^{-1} and medium range order observed in a-GeO_2 thin films.

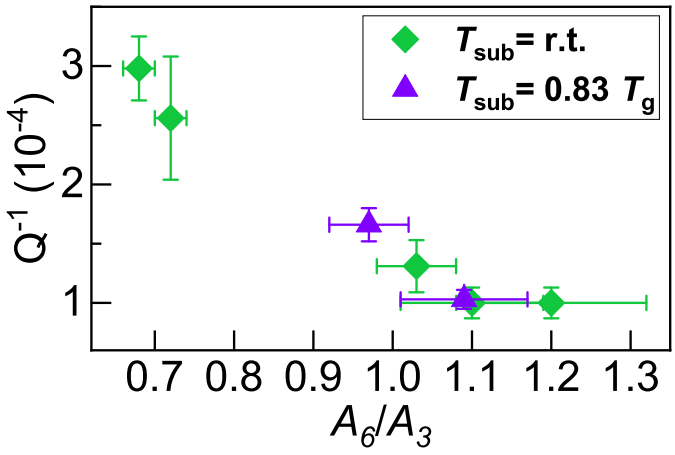


Figure 6.4: Internal friction Q^{-1} as a function of A_6/A_3 of a-GeO_2 thin films deposited at T_{sub} = room temperature (green) and T_{sub} = 0.83 T_g (purple).

6.4 Conclusion

The results conclusively show the atomic packing of strong network forming a-GeO_2 can be modified with elevated temperature deposition, similar to the behavior observed in organic glasses. The changes in the atomic packing are characterized by an increase in the fraction of 6-membered rings at the expense of 3-membered rings. This structural reorganization corresponds to an increase in medium range order, which is more significant when a-GeO_2 is deposited at T_{sub} = 0.83 T_g compared to films deposited at T_{sub} = room temperature and subsequently annealed.

Furthermore, the results establish a strong correlation between medium range order and room temperature internal friction in a-GeO_2. The increased packing organization leads to a

reduction in internal friction of as much as 44% when the film is deposited at T_{sub} = 0.83 T_g compared to T_{sub} = room temperature. Under optimum deposition and annealing conditions, the internal friction of a-GeO_2 reaches a value of $Q^{-1} = 1.00 \times 10^{-4}$, which is among the lowest in amorphous oxides and comparable to a-SiO_2. These findings are relevant for identifying suitable amorphous oxide candidates for mirror coatings of the end-test masses of gravitational wave interferometers, in which the coating's internal friction is the main source of noise limiting their sensitivity.

Chapter 7

Reduced Room-Temperature Thermal Noise in TiO_2-Doped GeO_2-Based Coatings for Gravitational Wave Detectors[10]

The sensitivity of current and planned gravitational wave interferometric detectors is limited, in the most sensitive frequency region, by a combination of quantum noise and thermal noise. The latter is dominated by Brownian noise in the dielectric coatings used in the mirrors, which in turn is related to the elastic energy loss in the thin film materials. We report the manufacturing of thin films of mixed titanium dioxide and germanium dioxide, and the measurement of elastic energy loss low enough to provide almost a factor of two improvement on the level of Brownian noise with respect to the materials currently used. This is a crucial step forward to produce the mirrors needed to meet the planned short and long term upgrades of the Advanced LIGO and Virgo detectors.

7.1 Introduction

Gravitational wave (GW) detectors are highly sensitive instruments that aim to measure the very small distance changes produced by astrophysical signals [76]. The current generation of GW detectors are km-scale laser interferometers [88, 118] with several hundreds of kW of

[10] Substantial portions of this chapter have been reproduced with permission from Gabriele Vajente, Le Yang, Mariana Fazio, Alena Ananyeva, Liyuan Zhang, GariLynn Billingsley, Kiran Prasai, Ashot Markosyan, Riccardo Bassiri, Martin M. Fejer, Martin Chicoine, François Schiettekatte, and Carmen S. Menoni, submitted.

circulating power. The test masses are made of high purity fused silica substrates, coated with high reflectivity multilayer dielectric thin film stacks [143] with transmission at the part per million level and very stringent surface and figure uniformity requirements [63]. The sensitivity of the current detectors [144, 145] is limited by a combination of laser quantum noise [146] and displacement noise generated by the Brownian motion of the coatings [40, 147]. Therefore, to increase the astrophysical reach of future detectors, it is crucial to reduce coating Brownian noise, which in turn amounts to reducing the mechanical energy loss in the thin film materials composing the multilayer coatings. In a simplified form, the power spectral density of Brownian noise at a frequency f is given by

$$S_{\text{Brownian}}(f) = \frac{k_B T}{\pi^2 f} \frac{d\phi(f)}{w^2 Y_S} \left(\frac{Y_C}{Y_S} + \frac{Y_S}{Y_C} \right) \tag{7.1}$$

where k_B is the Boltzman's constant, T is the ambient temperature, w is the spot size of the laser beam probing the mirror motion, Y_s and Y_c are the Young's modulus of the substrate and coating, respectively, $\phi(f)$ is the mechanical loss angle of the multilayer coating (possibly frequency dependent) and d is the total thickness of the multilayer dielectric coating stack. The coating is composed of multiple pairs of high and low refractive index metal oxide thin films, making a Bragg reflector structure. The Young's modulus and the loss angle of the coating are, in good approximation, given by the average of the values for the two materials, weighted by the amount of elastic energy stored in each layer (see [148] for a more precise and detailed discussion). The coatings used in the current Advanced LIGO (aLIGO) mirrors are composed of alternating layers of amorphous SiO_2 of low refractive index $n_{SiO_2} = 1.45$ at 1064 nm and TiO_2:Ta_2O_5 (titania-doped tantala) of high refractive index $n_{TiO_2:Ta_2O_5} = 2.10$ at 1064 nm [149]. The TiO_2:Ta_2O_5 layers have

a loss angle much larger than the SiO_2 layers ($\sim 3-4\times10^{-4}$ compared to $\sim 2\times10^{-5}$ [149]) and therefore they dominate in the contribution to the coating Brownian noise.

The goal for the next upgrade to the LIGO detectors, called Advanced LIGO+ [30, 79] is a reduction of the coating noise by about a factor of two, with a target Brownian noise of $0.66\times10^{-20}\mathrm{m}/\sqrt{\mathrm{Hz}}$ at a frequency of 100 Hz. The SiO_2 layers can already be produced with low enough mechanical loss angle [149], so the main focus of the current research is on manufacturing high refractive index materials with lower mechanical loss angles. Several different approaches were being investigated to reduce the mechanical loss of the materials, including deposition of oxides at elevated substrate temperatures [26, 83] and with assist ion bombardment [59, 75], doping and nanolayering of Ta_2O_5 [42, 43, 100], and the use of nitrides [149]. Here we report results on amorphous oxide coatings based on germania (GeO_2), in particular mixtures of GeO_2 and TiO_2, and how this novel material could be used to engineer high reflectivity coatings for the next room-temperature gravitational wave detectors, achieving a level of Brownian noise almost a factor of two lower than aLIGO and very close to the requirements for Advanced LIGO+.

The initial motivation to investigate coatings based on germania was the discovery of a correlation between the room-temperature mechanical loss angle and the fraction of edge-sharing versus face-sharing polyhedra in the medium-range order, as reported in [7] for ZrO_2:Ta_2O_5. SiO_2 has also a prevalence of corner-sharing structures, and exhibits very low mechanical loss angle. Additionally, the mechanical loss angle of GeO_2 at low temperatures [150] ($\lesssim 100$ K) exhibits a peak similar to the one found in SiO_2 [151], suggesting a decrease at room temperature. In recent experiments on GeO_2 [130], we confirmed that the atomic packing can be altered to improve medium range order by annealing and high temperature deposition.

From the optical perspective, however, GeO_2 has a refractive index n = 1.60 at 1064 nm that makes it unsuitable as high index layer in a high reflector, as hundreds of layers would be required to achieve the low transmissivity for the Advanced LIGO+ end test mass mirrors (5 ppm). The increase in the total thickness of a GeO_2/SiO_2 Bragg reflector would balance out the reduced mechanical loss of the high index layer, with no net improvement in the coating Brownian noise (see Table 7.2). To increase the refractive index at the laser wavelength of 1064 nm, GeO_2 was homogeneously mixed with TiO_2 with different cation concentrations. Among the various concentrations that we tested, we found that for a TiO_2 cation ratio of 44%, a TiO_2:GeO_2 mixture achieves a mechanical loss angle value around 1×10^{-4} upon annealing at 600°C. This value is more than a factor of 2 lower than state-of-the-art TiO_2:Ta_2O_5. Using the measured refractive index of 1.88 at 1064 nm for the TiO_2:GeO_2 thin film, we designed multilayer stacks for the input and end test masses for Advanced LIGO+. We show that the TiO_2:GeO_2/SiO_2 high reflectors annealed at 600°C can achieve a thermal noise of $0.74 \times 10^{-20} \mathrm{m}/\sqrt{\mathrm{Hz}}$, which is only 11% larger than the benchmark specified for Advanced LIGO+. These results identify TiO_2:GeO_2 as a promising alternative to TiO_2:Ta_2O_5 in the high reflector coatings of Advanced LIGO+. Further optimization studies are on-going to better characterize the optimal material mixture.

7.2 Material Properties

Structural and Optical Properties

Thin films of TiO_2:GeO_2 with Ti concentrations of 0%, 27%, and 44% were deposited by ion beam sputtering using a biased target deposition system [53]. Homogeneous oxide mixtures were formed by co-sputtering Ge and Ti targets with Ar^+ ions in a reactive oxygen atmosphere.

In this process, the selected dopant concentrations were obtained by adjusting the length of the pulses biasing the Ti and Ge targets. In addition, the oxygen partial pressure was adjusted to achieve nearly stoichiometric thin films with high optical quality. Mixed TiO_2:GeO_2 thin films of thickness between 200 and 500 nm were deposited on fused silica and silicon substrates for structural and optical characterizations.

The cation concentration, defined as Ti/(Ti+Ge), of the films was determined from Rutherford backscattering measurements [152]. The thickness and refractive index of the TiO_2:GeO_2 thin films were obtained from spectroscopic ellipsometry. The absorption loss at the wavelength of 1064 nm was assessed from photothermal common-path interferometry [55]. The mixture thin films were annealed in air up to a temperature where the first sign of crystallization was observed. All annealing cycles were carried out by ramping up the temperature by 100°C/h, holding at the maximum for 10 hours or longer, and then ramping down at 100°C/h. Annealing has been shown to reduce absorption loss and mechanical loss.

Figure 7.1 plots the variation in the refractive index at 1064 nm for the different TiO_2:GeO_2 mixtures. The refractive index of the different TiO_2:GeO_2 mixtures follows a monotonic relation with Ti content. For the Ti cation concentration of 44%, the refractive index at 1064 nm is $n_{TiO_2:GeO_2} = 1.88$. The absorption loss normalized to a quarter wavelength (141 nm) is 2.3 ± 0.1 ppm and 1.5 ± 0.1 ppm at λ = 1064 nm for the annealed 44% and 27% mixtures, respectively. The absorption loss of pure GeO_2 after annealing at 500°C is below 1 ppm at λ = 1064 nm.

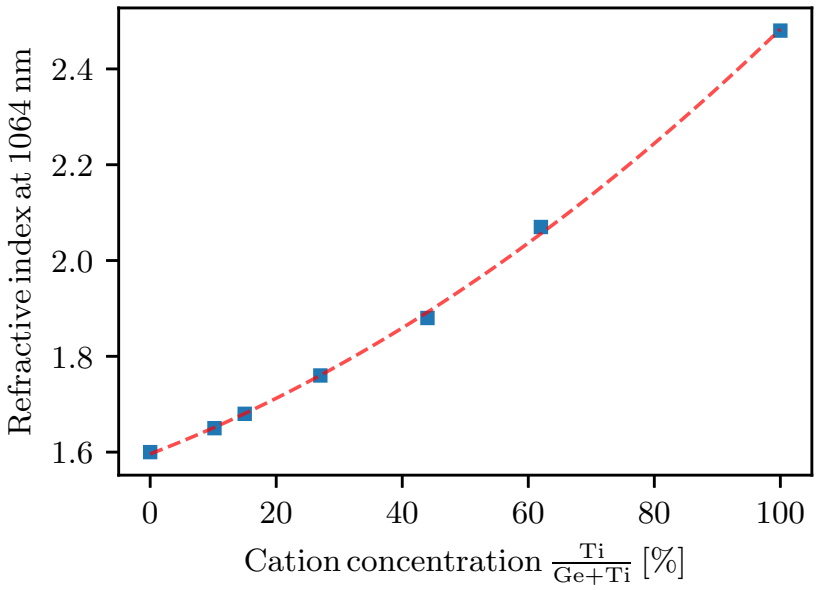


Figure 7.1: Measured refractive index n at 1064 nm as a function of the Ti/(Ti+Ge) concentration for different TiO_2:GeO_2 mixtures.

Grazing incidence x-ray diffraction shows all mixture films are amorphous upon annealing at 600°C. Figure 7.2 shows the spectra of the 27% and 44% TiO_2:GeO_2 thin films annealed at 600°C and 700°C for 10 hours. The thin films are amorphous after 600°C annealing and show incipient crystallization, identified by the peak at 25.3° from anatase TiO_2 phase, when annealed at 700°C. Annealing to 800°C for 10 hours revealed a full crystallization in the 44% mixture sample. It was also confirmed that the 44% sample did not show signs of crystallization upon annealing at 600°C for 108 hours.

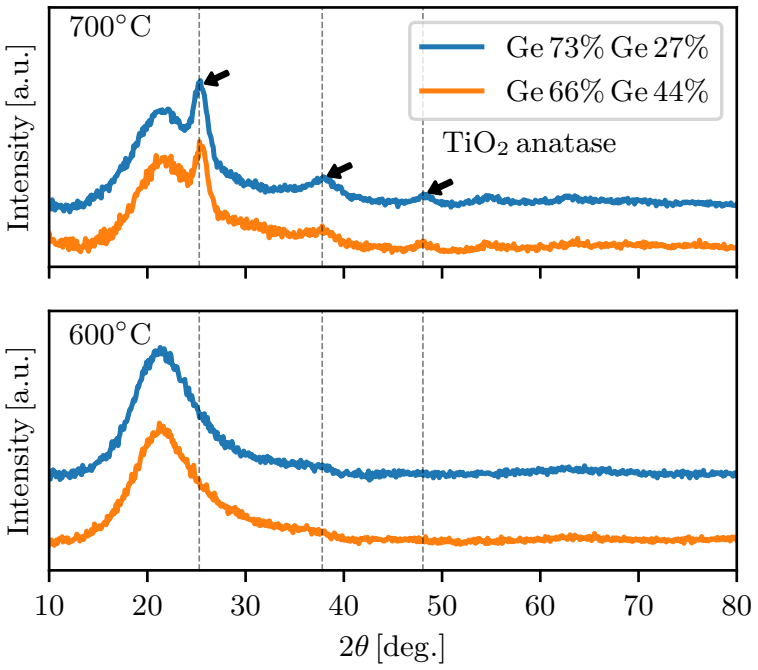


Figure 7.2: Grazing incidence x-ray diffractograms from 44% TiO_2:GeO_2 thin films annealed in air at 600 °C and 700°C for 10 hours. The broad peak at around 22° corresponds to the fused silica substrate. The peaks at 25.4°, 37.9°, and 48.0°, marked with arrows in the figure, are assigned to the TiO_2 anatase phase (JCPDS 84-1286 [153]).

Elastic Properties

The thin films were also deposited on 75-mm-diameter, 1-mm-thick silica disks, to measure the elastic properties of the material. The un-coated substrates were polished on all surfaces to a standard optical grade and annealed at 900°C for 10 hours, to obtain high quality factors of the substrate [154, 155]. The disk acts a resonator: the resonant modes between 1 kHz and 30 kHz were measured in a gentle nodal suspension [122, 155] to obtain the precise frequency and decay time of each mode. After the thin film is deposited on the substrate, the resonant frequencies are shifted by amounts depending on the mechanical and elastic properties of the film. The Young's modulus and Poisson ratio can then be estimated with a Bayesian regression

from the measured resonant frequency shifts [54, 149]. The decay time of the coated substrate modes is significantly shorter than for base substrate, due to the excess mechanical energy loss induced by the presence of the thin film. Using the measured material elastic properties, one can compute the fraction of elastic energy in the film for each resonant mode and use it to extract the loss angle ϕ of the thin film material [156].

Figure 7.3 shows the measured loss angle (averaged over all measured modes) and Young's modulus for several different concentrations of the oxides, from pure GeO_2 to 44% TiO_2. The pure GeO_2 films were annealed up to 500°C and remained amorphous, reaching the lowest loss angle measured in this campaign, at $(0.6 \pm 0.2) \times 10^{-4}$. Annealing at temperatures higher than 500°C showed signs of crystallization.

Of the two concentrations of TiO_2 and GeO_2 studied in detail here, the most promising results are from a mixture of almost equal parts (44% TiO_2 and 56% GeO_2). We annealed this film for 10 hours up to a temperature of 700°C, at which we obtained the lowest value of the loss angle for this material, at $(0.63 \pm 0.23) \times 10^{-4}$. However, as shown in Figure 7.2, the spectra show signs of crystallization. It can also be noted that the Young's modulus for the film shows a significant trend for annealing temperatures above 600°C, another indication of incipient crystallization. Further studies of the dynamics of the annealing process are underway to determine optimal conditions.

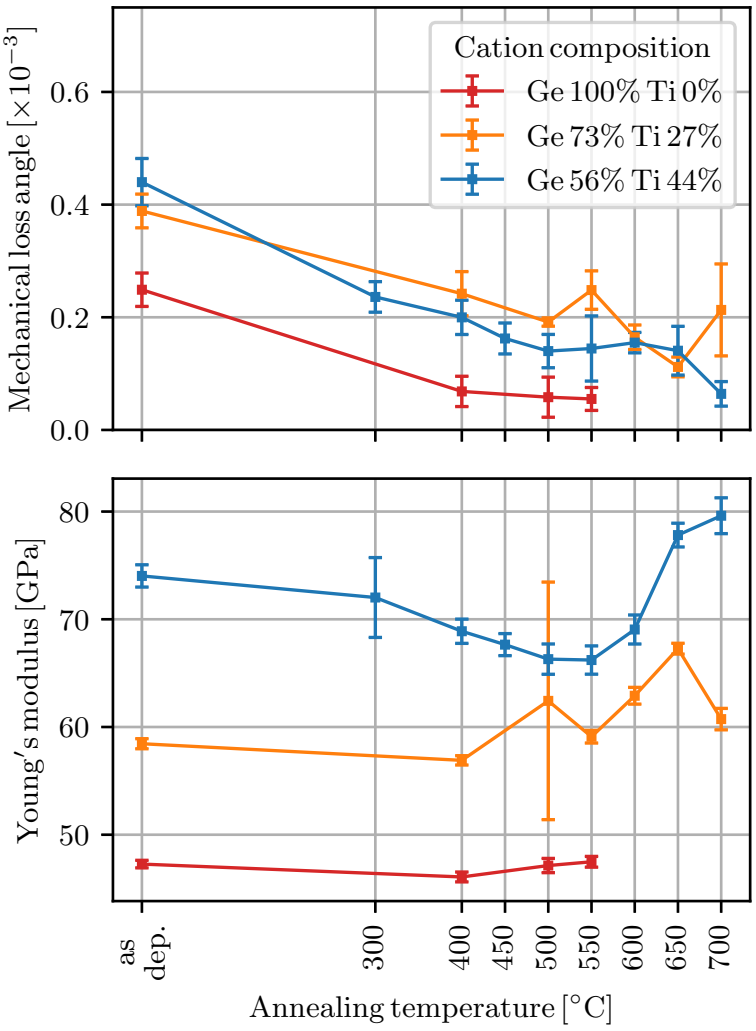


Figure 7.3: Measured loss angle (top) and Young's modulus (bottom) of mixed titanium oxide and germanium oxide, for the samples as deposited and after 10-hours-long heat treatments (annealing) in air, at increasing temperatures. Different color lines correspond to the cation composition listed in the legend. Only one sample for each concentration is shown here for simplicity. The other samples showed equal values within the error bars.

Another parameter that we explored to reduce the loss angle was the annealing duration. We tested heat treatments of 1 hour, 10 hours, 20 hours, 108 hours, and 216 hours in total, for temperatures of 500, 550, and 600°C. Figure 7.4 shows the effect of annealing time on the loss angle of the 44% TiO_2:GeO_2 mixture. It is found that extended annealing shows less effect at

lower annealing temperatures, resulting in almost no improvement in loss angle after 108 hours annealing at 500 and 550°C. Instead, after annealing at 600°C for 108 hours, the loss angle is reduced to $(0.96 \pm 0.18) \times 10^{-4}$, and the film is still amorphous. Annealing the same film for 108 more hours further reduced the loss angle, but also increased the Young's modulus such that the resulting coating Brownian noise would be worse.

Table 7.1 summarizes the measured properties of the 44% TiO_2:GeO_2 mixture annealed at 600°C for 108 hours that achieved both low mechanical loss and parts-per-million absorption loss at 1064 nm. Therefore, this TiO_2:GeO_2 mixture is the most promising material for the Advanced LIGO+ mirrors, among those tested in this work.

Table 7.1: Measured parameters for the best TiO_2:GeO_2 mixture, after annealing at 600°C for 108 hours.

Parameter	**Value**
Cation concentration, Ti/(Ti+Ge)	44%
Refractive index at 1064 nm	1.88
Density	3700 kg/m^3
Young's modulus	90.3 ± 1.3 GPa
Poisson ratio	0.24 ± 0.05
Loss angle	$0.96 \pm 0.18 \times 10^{-4}$
Optical absorption for a QWL	2.3 ± 0.1 ppm

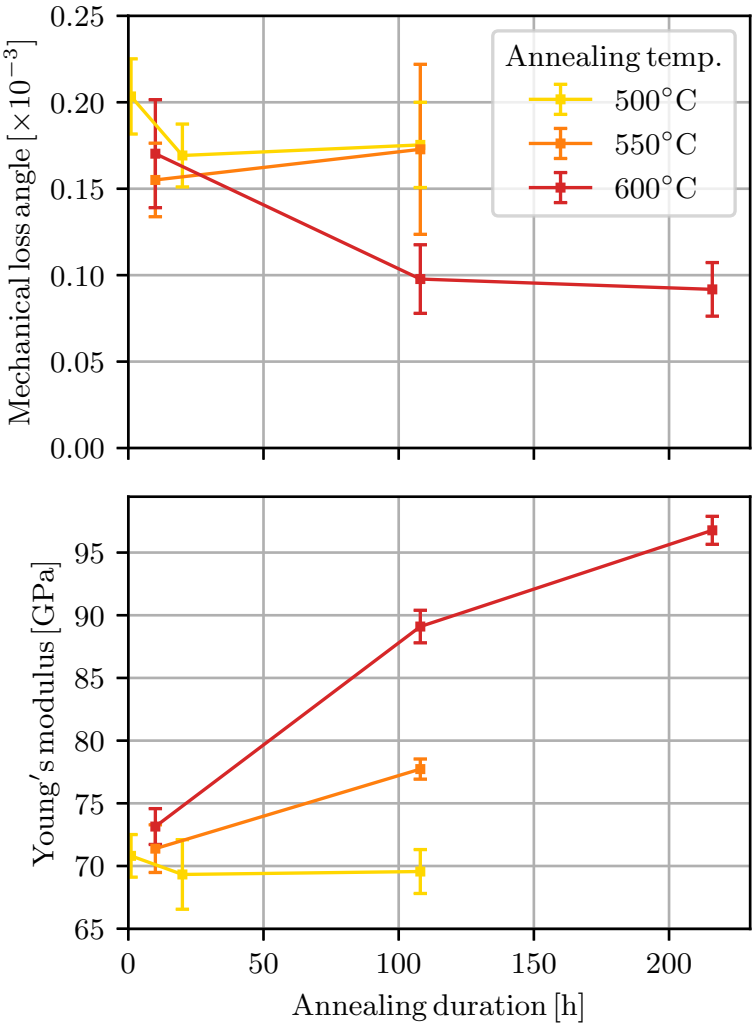


Figure 7.4: Effect of the annealing time on the measured mechanical loss angle (top) and Young's modulus (bottom) for the 44% TiO_2:GeO_2 sample.

7.3 Coating Design for Future Gravitational Wave Detectors

The transmission requirements for the Advanced LIGO+ test masses are similar to those for Advanced LIGO: the input mirror test masses (ITM) should have a transmission of 1.4% and the end test masses (ETM) of 5 ppm. For the ITM and ETM coating design, the stacks consist of doublets of high index and low index materials, with each layer having an optical thickness

close to a quarter wavelength at 1064 nm. The structure is capped with a half wavelength thick low index (SiO_2) layer. The number of doublets is initially chosen to obtain a transmission coefficient as close as possible to the design value. Then the thickness of the high index and low index layers are changed to match exactly the desired transmission, maintaining the sum equal to $\lambda/2$. The solution with less high index material is chosen since it also corresponds to lower Brownian noise.

Using the materials' parameters measured for the 44% TiO_2:GeO_2 in Table 7.1, we designed a high reflector multilayer coating consisting of doublets of TiO_2:GeO_2 and SiO_2 and calculated the Brownian noise [149, 157]. Table 7.2 summarizes the predicted Brownian noise for the four test masses and compares the results to literature values for the reference TiO_2:Ta_2O_5 and SiO_2 multilayer stacks used in aLIGO [149, 157]. We assume no excess loss or noise due to the substrate surface or interfaces between the layers [36].

The best material, 44% TiO_2:GeO_2 annealed for 10 hours at 700°C, gives a Brownian noise level on target for the Advanced LIGO+ design. As shown in Figure 7.2, this material shows signs of crystallization, which will require evaluation of how this affects the scattering in the coating. The same material, annealed at 600°C for longer times (108 hours), remains amorphous and shows a significant improvement in Brownian noise with respect to the TiO_2:Ta_2O_5 used currently in aLIGO, reaching a level only 11% larger than the design target.

Table 7.2: Computed Brownian noise for Advanced LIGO+ multilayer coatings, based on the measured material properties. The Input Test Mass (ITM) target transmission is 1.4% and the End Test Mass (ETM) is 5 ppm. The reference Advanced LIGO Brownian noise is obtained using the loss angle measured in the literature for titania-doped tantala [157]. The target Advanced LIGO+ noise level is taken from [30].

High index material	**ETM**		**ITM**		**Total Noise @ 100 Hz**	**Ratio w.r.t aLIGO**	**Ratio w.r.t. A+ design**
	Num. layers	Noise @ 100 Hz $\times 10^{-20}$ m/$\sqrt{\text{Hz}}$	Num. layers	Noise @ 100 Hz $\times 10^{-20}$ m/$\sqrt{\text{Hz}}$	$\times 10^{-20}$ m/$\sqrt{\text{Hz}}$	1.13×10^{-20} m/$\sqrt{\text{Hz}}$	0.66×10^{-20} m/$\sqrt{\text{Hz}}$
TiO_2:Ta_2O_5 (aLIGO)	38	0.65	16	0.46	1.13	1.00	1.71
GeO_2	138	0.61	56	0.44	1.07	0.94	1.61
44% TiO_2:GeO_2 annealed 10 hours at 700°C	52	0.37	22	0.26	0.64	0.57	0.97
44% TiO_2:GeO_2 annealed 108 hours at 600°C	52	0.42	22	0.30	0.74	0.65	1.11

7.4 Conclusions

We demonstrated that the TiO_2:GeO_2 offers excellent optical quality and low mechanical loss, which makes it suitable for use as high index layer in the high reflector coatings for the test mass of the Advanced LIGO+ interferometric gravitational wave detector. A mixture of 44% TiO_2 and 56% GeO_2 is the most promising material among those studied since we measured a loss angle of $(0.96 \pm 0.18) \times 10^{-4}$ after annealing in air at 600°C for 108 hours. Together with SiO_2, this new material would allow manufacturing coatings for Advanced LIGO+ with significantly reduced Brownian noise (only 11% larger than the design target). Together with the already demonstrated frequency dependent squeezing upgrade [158], this result would allow Advanced LIGO+ to reach a sensitivity 1.6 times better than the Advanced LIGO design at 100 Hz, improving the astrophysical reach for binary neutron stars by a factor of 1.6 and for binary black holes with a total mass of 60 $M_\odot$ by a factor of 1.4 [159].

Studies are on-going to further improve mechanical and absorption losses towards the goal of engineering a high reflection coating based on TiO_2:GeO_2 and SiO_2. We are also planning to directly measure the Brownian noise of these optimized high reflection mirrors designed for Advanced LIGO+.

Chapter 8

Summary and Outlook

Towards the goal of understanding the origin of mechanical loss in amorphous oxides, two systems are investigated: Ta_2O_5 and Ta_2O_5 based alloys, and GeO_2 and GeO_2 based alloys. The atomic structures of both Ta_2O_5 and GeO_2 can be viewed as a three-dimensional network linked by metal-centered oxygen polyhedra. The polyhedral connection could be corner, edge, or face-sharing, depending on how many oxygen atoms are shared between two polyhedra. For GeO_2, the covalent bonds are more directional and constrained so that the majority of the tetrahedra are connected at the corners. The inter-polyhedral M-O-M bond angle and the number of polyhedra linked in one ring determine the medium range order of these oxides.

It was found that for Ta_2O_5 the configurations at the medium range were not modified by low energy assist ion bombardment within the deposition conditions employed in this work. The coating mechanical losses of the Ta_2O_5 thin films bombarded by Ar^+ and Xe^+, regardless of the ion energy and ion dose, were comparable to that of the control samples with no assist ion bombardment (Chapter 3, Chapter 4). An analysis of the surface diffusivity suggested that the sputtered particles were mainly clusters that were essentially immobile. The bombarding ions were able to affect at most the short-range order at the point of incidence. The inability to affect ion-bombarded Ta_2O_5 at the medium range order is ascribed to the large difference between the number of sputtered particles arriving at the substrate and the ion dose.

Alternative ways to modify the medium range order of Ta_2O_5 were sought through the incorporation of dopants and nanolayers in the Ta_2O_5 matrix. The introduction of structure motifs

of SiO_2 with a high degree of medium range order was expected to improve the mechanical loss of the resulting mixtures and nanolaminates. However, the findings in Chapter 5 showed that when the Ta_2O_5/SiO_2 systems were annealed, the two binaries stayed as separate phases. In this case, the mechanical loss of the Ta_2O_5/SiO_2 mixture was similar to that of a single layer Ta_2O_5 as the medium range was not modified by the SiO_2 motifs. In contrast, the mixing of TiO_2 and Ta_2O_5 was thermodynamically favored upon annealing, and was associated with a significant improvement in the mechanical loss of the TiO_2/Ta_2O_5 system compared to the SiO_2/Ta_2O_5 system. The formation of a stable ternary phase was found to be key to altering the medium range order in Ta_2O_5.

The critical role medium range order plays in affecting the mechanical loss was further demonstrated in the GeO_2 system that has a high degree of medium range order similar to that of SiO_2. In experiments in which the medium range order was assessed from Raman spectroscopy, it was found that elevated substrate temperature and post-deposition annealing were both effective at improving the atomic packing at the medium range order of the GeO_2. The change at this range was characterized by a significantly increased fraction of 6-membered rings at the expense of 3-membered rings in the atomic network (Chapter 6). The increased medium range order showed a strong correlation with the decreasing mechanical loss of the GeO_2 thin films, which reduced to the lowest value around 1×10^{-4} among all oxides. This work is novel in that it conclusively showed the interplay in the increase in medium range order defined by polyhedral connection and the room temperature mechanical loss. The elimination of strained 3-membered rings suppressed the two-level system transitions associated with room temperature mechanical loss.

The above-mentioned work has demonstrated that the medium range order in the oxides, defined by the polyhedral connection, could be beneficially modified by the formation of a thermodynamically stable phase, elevated deposition temperature, and alternatively thermal annealing at high temperatures. Such rearrangements in the polyhedral connecting rings play a critical role in reducing the room temperature mechanical loss of the oxides.

To achieve the ultimate goal of realizing a high-index material for the mirror coating of next generation gravitational wave detectors, further engineering of GeO_2 by doping TiO_2 was carried out in Chapter 7. The 44% TiO_2:GeO_2 mixture was found to have both excellent optical quality and low mechanical loss. Together with SiO_2, this new material would allow manufacturing coatings with reduced Brownian noise near the benchmark for Advanced LIGO+.

For future work, characterization of the cryogenic mechanical loss behavior of the GeO_2 thin films would be crucial to understanding the link between the low temperature and room temperature mechanical loss in the amorphous thin films. The cryogenic mechanical loss measurements would allow for a direct calculation of the population of associated two-level systems in the thin films [28]. Preliminary results of the atomic modeling in work [49] have shown that the two-level systems responsible for the cryogenic and room temperature mechanical loss are different. The prior one is mainly associated with polyhedra rotating around the connecting point and the latter one involves bond breaking within the polyhedra. As such, the correlation between the expansion in the connecting ring and the cryogenic mechanical loss is expected to be not significant for samples annealed at different temperatures. This would further strengthen the conclusion that medium range order is related to the room temperature mechanical loss of the amorphous thin films.

Bibliography

[1] Daisuke Yokoyama. Molecular orientation in small-molecule organic light-emitting diodes. *Journal of Materials Chemistry*, 21(48):19187–19202, 2011.

[2] Stephen R Elliott. Medium-range structural order in covalent amorphous solids. *Nature*, 354(6353):445–452, 1991.

[3] Shinji Kohara and Kentaro Suzuya. Intermediate-range order in vitreous sio2 and geo2. *Journal of Physics: Condensed Matter*, 17(5):S77, 2005.

[4] R Dupree, D Holland, Peter W McMillan, and RF Pettifer. The structure of soda-silica glasses: a mas nmr study. *Journal of Non-Crystalline Solids*, 68(2-3):399–410, 1984.

[5] Dan J Durben and George H Wolf. Raman spectroscopic study of the pressure-induced coordination change in geo 2 glass. *Physical Review B*, 43(3):2355, 1991.

[6] Weiying Song, Xin Li, Bu Wang, NM Anoop Krishnan, Sushmit Goyal, Morten M Smedskjaer, John C Mauro, Christian G Hoover, and Mathieu Bauchy. Atomic picture of structural relaxation in silicate glasses. *Applied Physics Letters*, 114(23):233703, 2019.

[7] Kiran Prasai, Jun Jiang, Alec Mishkin, B Shyam, S Angelova, R Birney, DA Drabold, M Fazio, EK Gustafson, G Harry, et al. High precision detection of change in intermediate range order of amorphous zirconia-doped tantala thin films due to annealing. *Physical review letters*, 123(4):045501, 2019.

[8] Lawrence Kazmerski. *Polycrystalline and amorphous thin films and devices*. Elsevier, 2012.

[9] Hideaki Hikawa, Masaharu Oguni, and Hiroshi Suga. Construction of an adiabatic calorimeter for a vapor-deposited sample and thermal characterization of amorphous butyronitrile. *Journal of non-crystalline solids*, 101(1):90–100, 1988.

[10] Shashank C Deshmukh and Eray S Aydil. Low-temperature plasma enhanced chemical vapor deposition of sio2. *Applied physics letters*, 65(25):3185–3187, 1994.

[11] Namjun Kim and Jonathan F Stebbins. Structure of amorphous tantalum oxide and titania-doped tantala: 17o nmr results for sol–gel and ion-beam-sputtered materials. *Chemistry of Materials*, 23(15):3460–3465, 2011.

[12] Daniel R Reid, Ivan Lyubimov, MD Ediger, and Juan J De Pablo. Age and structure of a model vapour-deposited glass. *Nature communications*, 7(1):1–9, 2016.

[13] Giorgio Parisi and Francesco Sciortino. Flying to the bottom. *Nature materials*, 12(2):94–95, 2013.

[14] Camille Bishop, Ankit Gujral, Michael F Toney, Lian Yu, and Mark D Ediger. Vapor-deposited glass structure determined by deposition rate–substrate temperature superposition principle. *The journal of physical chemistry letters*, 10(13):3536–3542, 2019.

[15] Shakeel S Dalal, Diane M Walters, Ivan Lyubimov, Juan J de Pablo, and MD Ediger. Tunable molecular orientation and elevated thermal stability of vapor-deposited organic semiconductors. *Proceedings of the National Academy of Sciences*, 112(14):4227–4232, 2015.

[16] Ankit Gujral, Kathryn A O'Hara, Michael F Toney, Michael L Chabinyc, and MD Ediger. Structural characterization of vapor-deposited glasses of an organic hole transport material with x-ray scattering. *Chemistry of Materials*, 27(9):3341–3348, 2015.

[17] W Ensinger. Low energy ion assist during deposition—an effective tool for controlling thin film microstructure. *Nuclear Instruments and Methods in Physics Research Section B: Beam Interactions with Materials and Atoms*, 127:796–808, 1997.

[18] Israel Perez, Víctor Sosa, Fidel Gamboa Perera, José Trinidad Elizalde Galindo, José L Enríquez-Carrejo, and Pierre Giovanni Mani González. Effect of ion bombardment on the chemical properties of crystalline tantalum pentoxide films. *Vacuum*, 165:274–282, 2019.

[19] Stephen F Swallen, Kenneth L Kearns, Marie K Mapes, Yong Seol Kim, Robert J McMahon, Mark D Ediger, Tian Wu, Lian Yu, and Sushil Satija. Organic glasses with exceptional thermodynamic and kinetic stability. *Science*, 315(5810):353–356, 2007.

[20] Pablo G Debenedetti and Frank H Stillinger. Supercooled liquids and the glass transition. *Nature*, 410(6825):259–267, 2001.

[21] RC Zeller and RO Pohl. Thermal conductivity and specific heat of noncrystalline solids. *Physical Review B*, 4(6):2029, 1971.

[22] Robert O Pohl, Xiao Liu, and EunJoo Thompson. Low-temperature thermal conductivity and acoustic attenuation in amorphous solids. *Reviews of Modern Physics*, 74(4):991, 2002.

[23] WA Phillips. Two-level states in glasses. *Reports on Progress in Physics*, 50(12):1657, 1987.

[24] KS Gilroy and WA Phillips. An asymmetric double-well potential model for structural relaxation processes in amorphous materials. *Philosophical Magazine B*, 43(5):735–746, 1981.

[25] Rashid Hamdan, Jonathan P Trinastic, and HP Cheng. Molecular dynamics study of the mechanical loss in amorphous pure and doped silica. *The Journal of chemical physics*, 141(5):054501, 2014.

[26] Xiao Liu, Daniel R Queen, Thomas H Metcalf, Julie E Karel, and Frances Hellman. Hydrogen-free amorphous silicon with no tunneling states. *Physical review letters*, 113(2):025503, 2014.

[27] DR Queen, X Liu, J Karel, TH Metcalf, and F Hellman. Excess specific heat in evaporated amorphous silicon. *Physical review letters*, 110(13):135901, 2013.

[28] DR Queen, X Liu, J Karel, HC Jacks, TH Metcalf, and F Hellman. Two-level systems in evaporated amorphous silicon. *Journal of Non-Crystalline Solids*, 426:19–24, 2015.

[29] Tomás Pérez-Castañeda, Cristian Rodríguez-Tinoco, Javier Rodríguez-Viejo, and Miguel A Ramos. Suppression of tunneling two-level systems in ultrastable glasses of indomethacin. *Proceedings of the National Academy of Sciences*, 111(31):11275–11280, 2014.

[30] L. S. Collaboration. Instrument science white paper 2020. 2020.

[31] A Einstein. Die grundlage der allgemeinen relativitätstheorie [adp 49, 769 (1916)]. *Annalen der Physik*, 354(7):769–822, 1916.

[32] Iain William Martin. *Studies of materials for use in future interferometric gravitational wave detectors*. PhD thesis, University of Glasgow, 2009.

[33] Benjamin P Abbott, R Abbott, TD Abbott, MR Abernathy, F Acernese, K Ackley, C Adams, T Adams, P Addesso, RX Adhikari, et al. Gw150914: The advanced ligo detectors in the era of first discoveries. *Physical review letters*, 116(13):131103, 2016.

[34] Stuart Reid and Iain W Martin. Development of mirror coatings for gravitational wave detectors. *Coatings*, 6(4):61, 2016.

[35] Gregory M Harry, Matthew R Abernathy, Andres E Becerra-Toledo, Helena Armandula, Eric Black, Kate Dooley, Matt Eichenfield, Chinyere Nwabugwu, Akira Villar, DRM Crooks, et al. Titania-doped tantala/silica coatings for gravitational-wave detection. *Classical and Quantum Gravity*, 24(2):405, 2006.

[36] Massimo Granata, Emeline Saracco, Nazario Morgado, Alix Cajgfinger, Gianpietro Cagnoli, Jérôme Degallaix, Vincent Dolique, Danièle Forest, Janyce Franc, Christophe Michel, et al. Mechanical loss in state-of-the-art amorphous optical coatings. *Physical Review D*, 93(1):012007, 2016.

[37] Cheng-Chung Lee, Jin-Cherng Hsu, and Daw-Heng Wong. The characteristics of some metallic oxides prepared in high vacuum by ion beam sputtering. *Applied surface science*, 171(1-2):151–156, 2001.

[38] PF Langston, E Krous, D Schiltz, D Patel, L Emmert, A Markosyan, B Reagan, K Wernsing, Y Xu, Z Sun, et al. Point defects in sc 2 o 3 thin films by ion beam sputtering. *Applied optics*, 53(4):A276–A280, 2014.

[39] L Anghinolfi, M Prato, A Chtanov, M Gross, A Chincarini, M Neri, G Gemme, and M Canepa. Optical properties of uniform, porous, amorphous ta2o5 coatings on silica: temperature effects. *Journal of Physics D: Applied Physics*, 46(45):455301, 2013.

[40] Yu Levin. Internal thermal noise in the ligo test masses: A direct approach. *Physical Review D*, 57(2):659, 1998.

[41] Steven D Penn, Peter H Sneddon, Helena Armandula, Joseph C Betzwieser, Gianpietro Cagnoli, Jordan Camp, DRM Crooks, Martin M Fejer, Andri M Gretarsson, Gregory M Harry, et al. Mechanical loss in tantala/silica dielectric mirror coatings. *Classical and Quantum Gravity*, 20(13):2917, 2003.

[42] Raffaele Flaminio, Janyce Franc, Christine Michel, Nazario Morgado, Laurent Pinard, and Benoit Sassolas. A study of coating mechanical and optical losses in view of reducing mirror thermal noise in gravitational wave detectors. *Classical and Quantum Gravity*, 27(8):084030, 2010.

[43] Mariana Fazio, Gabriele Vajente, Alena Ananyeva, Ashot Markosyan, Riccardo Bassiri, Martin Fejer, and Carmen S Menoni. Structure and morphology of low mechanical loss tio_2-doped ta_2o_5. *Opt. Mater. Express*, 10(7):1687, 2020.

[44] Ling-Chi Kuo, Huang-Wei Pan, Chi-Li Chang, and Shiuh Chao. Low cryogenic mechanical loss composite silica thin film for low thermal noise dielectric mirror coatings. *Optics letters*, 44(2):247–250, 2019.

[45] Martin J Hart, Riccardo Bassiri, Konstantin B Borisenko, Muriel Véron, Edgar F Rauch, Iain W Martin, Sheila Rowan, Martin M Fejer, and Ian MacLaren. Medium range struc-

tural order in amorphous tantala spatially resolved with changes to atomic structure by thermal annealing. *Journal of Non-Crystalline Solids*, 438:10–17, 2016.

[46] R Bassiri, K Evans, KB Borisenko, MM Fejer, J Hough, I MacLaren, IW Martin, RK Route, and S Rowan. Correlations between the mechanical loss and atomic structure of amorphous tio2-doped ta2o5 coatings. *Acta Materialia*, 61(4):1070–1077, 2013.

[47] Jonathan P Trinastic, Rashid Hamdan, Chris Billman, and Hai-Ping Cheng. Molecular dynamics modeling of mechanical loss in amorphous tantala and titania-doped tantala. *Physical Review B*, 93(1):014105, 2016.

[48] Chris R Billman, Jonathan P Trinastic, Dustin J Davis, Rashid Hamdan, and Hai-Ping Cheng. Origin of the second peak in the mechanical loss function of amorphous silica. *Physical Review B*, 95(1):014109, 2017.

[49] Jun Jiang, Alec Mishkin, Kiran Prasai, Rui Zhang, Maher Yazback, Riccardo Bassiri, Martin Fejer, and Hai-ping Cheng. Analysis of two-level systems and mechanical loss in amorphous zro2-doped ta2o5 by non-cage-breaking and cage-breaking transitions. *xx*, x(x):xxx, 3021.

[50] Ross Birney, J Steinlechner, Z Tornasi, Sean MacFoy, David Vine, AS Bell, Desmond Gibson, Jim Hough, Sheila Rowan, P Sortais, et al. Amorphous silicon with extremely low absorption: beating thermal noise in gravitational astronomy. *Physical review letters*, 121(19):191101, 2018.

[51] Massimo Granata, Alex Amato, Gianpietro Cagnoli, Matthieu Coulon, Jérôme Degallaix, Danièle Forest, Lorenzo Mereni, Christophe Michel, Laurent Pinard, Benoît Sassolas,

et al. Progress in the measurement and reduction of thermal noise in optical coatings for gravitational-wave detectors. *Applied Optics*, 59(5):A229–A235, 2020.

[52] Steven D Penn, Maya M Kinley-Hanlon, Ian AO MacMillan, Paula Heu, David Follman, Christoph Deutsch, Garrett D Cole, and Gregory M Harry. Mechanical ringdown studies of large-area substrate-transferred gaas/algaas crystalline coatings. *JOSA B*, 36(4):C15–C21, 2019.

[53] Kevin G West, Jiwei Lu, Jiani Yu, David Kirkwood, Wei Chen, Yonghang Pei, John Claassen, and Stuart A Wolf. Growth and characterization of vanadium dioxide thin films prepared by reactive-biased target ion beam deposition. *Journal of Vacuum Science & Technology A: Vacuum, Surfaces, and Films*, 26(1):133–139, 2008.

[54] G Vajente, A Ananyeva, G Billingsley, E Gustafson, A Heptonstall, E Sanchez, and C Torrie. A high throughput instrument to measure mechanical losses in thin film coatings. *Review of Scientific Instruments*, 88(7):073901, 2017.

[55] Alexei Alexandrovski, Martin Fejer, A Markosian, and Roger Route. Photothermal common-path interferometry (pci): new developments. In *Solid State Lasers XVIII: Technology and Devices*, volume 7193, page 71930D. International Society for Optics and Photonics, 2009.

[56] Erik Krous. Characterization of scandium oxide thin films for use in interference coatings for high-power lasers operating in the near-infrared. Master's thesis, Department of Electrical and Computer Engineering, Colorado State University, Fort Collins, CO, 2010.

[57] Matthieu Micoulaut, L Cormier, and GS Henderson. The structure of amorphous, crystalline and liquid geo2. *Journal of Physics: Condensed Matter*, 18(45):R753, 2006.

[58] Grant S Henderson, Daniel R Neuville, Benjamin Cochain, and Laurent Cormier. The structure of geo2–sio2 glasses and melts: A raman spectroscopy study. *Journal of Non-Crystalline Solids*, 355(8):468–474, 2009.

[59] Le Yang, Emmett Randel, Gabriele Vajente, Alena Ananyeva, Eric Gustafson, Ashot Markosyan, Riccardo Bassiri, Martin Fejer, and Carmen Menoni. Modifications of ion beam sputtered tantala thin films by secondary argon and oxygen bombardment. *Applied optics*, 59(5):A150–A154, 2020.

[60] Andrew Brown, Albert Ogloza, Lucas Taylor, Jeff Thomas, and Joseph Talghader. Continuous-wave laser damage and conditioning of particle contaminated optics. *Applied optics*, 54(16):5216–5222, 2015.

[61] Drew Schiltz, Dinesh Patel, Cory Baumgarten, Brendan A Reagan, Jorge J Rocca, and Carmen S Menoni. Strategies to increase laser damage performance of ta 2 o 5/sio 2 mirrors by modifications of the top layer design. *Applied Optics*, 56(4):C136–C139, 2017.

[62] Dorian Gangloff, Molu Shi, Tailin Wu, Alexei Bylinskii, Boris Braverman, Michael Gutierrez, Rosanna Nichols, Junru Li, Kai Aichholz, Marko Cetina, et al. Preventing and reversing vacuum-induced optical losses in high-finesse tantalum (v) oxide mirror coatings. *Optics express*, 23(14):18014–18028, 2015.

[63] L Pinard, C Michel, B Sassolas, L Balzarini, J Degallaix, V Dolique, R Flaminio, D Forest, M Granata, B Lagrange, et al. Mirrors used in the ligo interferometers for first detection of gravitational waves. *Applied optics*, 56(4):C11–C15, 2017.

[64] Junaid Aasi, BP Abbott, Richard Abbott, Thomas Abbott, MR Abernathy, Kendall Ackley, Carl Adams, Thomas Adams, Paolo Addesso, RX Adhikari, et al. Advanced ligo. *Classical and quantum gravity*, 32(7):074001, 2015.

[65] PJ Martin, RP Netterfield, and WG Sainty. Modification of the optical and structural properties of dielectric zro2 films by ion-assisted deposition. *Journal of Applied Physics*, 55(1):235–241, 1984.

[66] Eda Çetinörgü, Bill Baloukas, Oleg Zabeida, Jolanta E Klemberg-Sapieha, and Ludvik Martinu. Mechanical and thermoelastic characteristics of optical thin films deposited by dual ion beam sputtering. *Applied optics*, 48(23):4536–4544, 2009.

[67] Cheng-Chung Lee, Jin-Cherng Hsu, David T Wei, and Jiun-Horng Lin. Morphology of dual beam ion sputtered films investigated by atomic force microscopy. *Thin Solid Films*, 308:74–78, 1997.

[68] MF Lambrinos, R Valizadeh, and JS Colligon. Effects of bombardment on optical properties during the deposition of silicon nitride by reactive ion-beam sputtering. *Applied optics*, 35(19):3620–3626, 1996.

[69] AS Markosyan, R Route, MM Fejer, D Patel, and C Menoni. Study of spontaneous and induced absorption in amorphous ta2o5 and sio2 dielectric thin films. *Journal of Applied Physics*, 113(13):133104, 2013.

[70] Nicholas Winograd. The magic of cluster sims, 2005.

[71] Trevor J Bright, JI Watjen, ZM Zhang, Christopher Muratore, Andrey A Voevodin, DI Koukis, David B Tanner, and Daniel J Arenas. Infrared optical properties of amorphous and nanocrystalline ta2o5 thin films. *Journal of Applied Physics*, 114(8):083515, 2013.

[72] Mirza Cevro and George Carter. Ion-beam and dual-ion-beam sputter deposition of tantalum oxide films. *Optical Engineering*, 34(2):596–607, 1995.

[73] Cedric Mannequin, Tohru Tsuruoka, Tsuyoshi Hasegawa, and Masakazu Aono. Identification and roles of nonstoichiometric oxygen in amorphous ta2o5 thin films deposited by electron beam and sputtering processes. *Applied Surface Science*, 385:426–435, 2016.

[74] DRM Crooks, G Cagnoli, MM Fejer, A Gretarsson, Gregory Harry, James Hough, N Nakagawa, S Penn, R Route, S Rowan, et al. Experimental measurements of coating mechanical loss factors. *Classical and Quantum Gravity*, 21(5):S1059, 2004.

[75] Le Yang, Emmett Randel, Gabriele Vajente, Alena Ananyeva, Eric Gustafson, Ashot Markosyan, Riccardo Bassiri, Martin M Fejer, and Carmen S Menoni. Investigation of effects of assisted ion bombardment on mechanical loss of sputtered tantala thin films for gravitational wave interferometers. *Physical Review D*, 100(12):122004, 2019.

[76] Benjamin P Abbott, Richard Abbott, TD Abbott, MR Abernathy, Fausto Acernese, Kendall Ackley, Carl Adams, Thomas Adams, Paolo Addesso, RX Adhikari, et al. Observation of gravitational waves from a binary black hole merger. *Physical review letters*, 116(6):061102, 2016.

[77] Benjamin P Abbott, Rich Abbott, TD Abbott, Fausto Acernese, Kendall Ackley, Carl Adams, Thomas Adams, Paolo Addesso, RX Adhikari, VB Adya, et al. Gw170817: observation of gravitational waves from a binary neutron star inspiral. *Physical Review Letters*, 119(16):161101, 2017.

[78] Gregory M Harry, Andri M Gretarsson, Peter R Saulson, Scott E Kittelberger, Steven D Penn, William J Startin, Sheila Rowan, Martin M Fejer, DRM Crooks, Gianpietro Cagnoli, et al. Thermal noise in interferometric gravitational wave detectors due to dielectric optical coatings. *Classical and Quantum Gravity*, 19(5):897, 2002.

[79] John Miller, Lisa Barsotti, Salvatore Vitale, Peter Fritschel, Matthew Evans, and Daniel Sigg. Prospects for doubling the range of advanced ligo. *Physical Review D*, 91(6):062005, 2015.

[80] Yuk Tung Liu and Kip S Thorne. Thermoelastic noise and homogeneous thermal noise in finite sized gravitational-wave test masses. *Physical Review D*, 62(12):122002, 2000.

[81] Yuri Levin. Fluctuation–dissipation theorem for thermo-refractive noise. *Physics Letters A*, 372(12):1941–1944, 2008.

[82] Alex Amato, Gianpietro Cagnoli, Maurizio Canepa, Elodie Coillet, Jerome Degallaix, Vincent Dolique, Daniele Forest, Massimo Granata, Valérie Martinez, Christophe Michel, et al. In *Journal of Physics: Conference Series*, volume 957, page 012006. IOP Publishing, 2018.

[83] G Vajente, Ross Birney, A Ananyeva, S Angelova, R Asselin, B Baloukas, R Bassiri, G Billingsley, MM Fejer, D Gibson, et al. Effect of elevated substrate temperature de-

position on the mechanical losses in tantala thin film coatings. *Classical and Quantum Gravity*, 35(7):075001, 2018.

[84] R Ditchfield and EG Seebauer. Direct measurement of ion-influenced surface diffusion. *Physical review letters*, 82(6):1185, 1999.

[85] R Ditchfield and Edmund G Seebauer. Semiconductor surface diffusion: Effects of low-energy ion bombardment. *Physical Review B*, 63(12):125317, 2001.

[86] EH Hirsch and IK Varga. Thin film annealing by ion bombardment. *Thin Solid Films*, 69(1):99–105, 1980.

[87] R Bassiri, KB Borisenko, DJH Cockayne, J Hough, I MacLaren, and S Rowan. Probing the atomic structure of amorphous ta 2 o 5 coatings. *Applied Physics Letters*, 98(3):031904, 2011.

[88] LIGO Scientific Collaboration et al. Advanced ligo. *Class Quantum Grav*, 32:074001, 2015.

[89] Israel Perez, José Luis Enríquez Carrejo, Víctor Sosa, Fidel Gamboa Perera, José Rurik Farias Mancillas, José Trinidad Elizalde Galindo, and Carlos Iván Rodríguez Rodríguez. Evidence for structural transition in crystalline tantalum pentoxide films grown by rf magnetron sputtering. *Journal of Alloys and Compounds*, 712:303–310, 2017.

[90] E Atanassova, G Tyuliev, A Paskaleva, D Spassov, and K Kostov. Xps study of n2 annealing effect on thermal ta2o5 layers on si. *Applied surface science*, 225(1-4):86–99, 2004.

[91] Robin Simpson, Richard G White, John F Watts, and Mark A Baker. Xps investigation of monatomic and cluster argon ion sputtering of tantalum pentoxide. *Applied Surface Science*, 405:79–87, 2017.

[92] Riccardo Bassiri, Franklin Liou, Matthew R Abernathy, Angie C Lin, Namjun Kim, Apurva Mehta, Badri Shyam, Robert L Byer, Eric K Gustafson, Martin Hart, et al. Order within disorder: The atomic structure of ion-beam sputtered amorphous tantala (a-ta2o5). *APL materials*, 3(3):036103, 2015.

[93] Devendra Gupta. *Diffusion processes in advanced technological materials*. Springer Science & Business Media, 2010.

[94] R Nakamura, T Toda, S Tsukui, M Tane, M Ishimaru, T Suzuki, and H Nakajima. Diffusion of oxygen in amorphous al2o3, ta2o5, and nb2o5. *Journal of applied Physics*, 116(3):033504, 2014.

[95] Yingge Du, Zdenek Dohnalek, and Igor Lyubinetsky. Transient mobility of oxygen adatoms upon o2 dissociation on reduced tio2 (110). *The Journal of Physical Chemistry C*, 112(7):2649–2653, 2008.

[96] EG Seebauer and CE Allen. Estimating surface diffusion coefficients. *Progress in surface science*, 49(3):265–330, 1995.

[97] Oliver LG Alderman, CJ Benmore, J Neuefeind, E Coillet, A Mermet, V Martinez, Anthony Tamalonis, and Rick Weber. Amorphous tantala and its relationship with the molten state. *Physical Review Materials*, 2(4):043602, 2018.

[98] TM Mayer, E Chason, and AJ Howard. Roughening instability and ion-induced viscous relaxation of sio2 surfaces. *Journal of applied physics*, 76(3):1633–1643, 1994.

[99] R Mark Bradley and James ME Harper. Theory of ripple topography induced by ion bombardment. *Journal of Vacuum Science & Technology A: Vacuum, Surfaces, and Films*, 6(4):2390–2395, 1988.

[100] Le Yang, Mariana Fazio, Gabriele Vajente, Alena Ananyeva, GariLynn Billingsley, Ashot Markosyan, Riccardo Bassiri, Martin M Fejer, and Carmen S Menoni. Structural evolution of binary oxide nanolaminates with annealing and its impact on room-temperature internal friction. *arXiv preprint arXiv:2010.04272*, 2020.

[101] P Tsipas, SN Volkos, A Sotiropoulos, SF Galata, G Mavrou, D Tsoutsou, Y Panayiotatos, A Dimoulas, C Marchiori, and J Fompeyrine. Germanium-induced stabilization of a very high-k zirconia phase in Zro 2/GeO 2 gate stacks. *Applied physics letters*, 93(8):082904, 2008.

[102] GD Wilk, RM Wallace, and JM Anthony. Hafnium and zirconium silicates for advanced gate dielectrics. *Journal of Applied Physics*, 87(1):484–492, 2000.

[103] F Boscherini, F D'Acapito, SF Galata, D Tsoutsou, and A Dimoulas. Atomic scale mechanism for the ge-induced stabilization of the tetragonal, very high-κ, phase of zro2. *Applied Physics Letters*, 99(12):121909, 2011.

[104] Xiaogeng Huo, Xiao-Xu Wang, Zhanyu Li, Jian Liu, and Jianling Li. Two-dimensional composite of d-ti3c2tx@ s@ tio2 (mxene) as cathode material for aluminum-ion batteries. *Nanoscale*, 2020.

[105] Naba K Sahoo and Alan P Shapiro. Mgo–al 2 o 3–zro 2 amorphous ternary composite: a dense and stable optical coating. *Applied optics*, 37(34):8043–8056, 1998.

[106] L Karvonen, A Säynätjoki, Y Chen, H Jussila, J Rönn, M Ruoho, T Alasaarela, S Kujala, Robert A Norwood, N Peyghambarian, et al. Enhancement of the third-order optical nonlinearity in zno/al2o3 nanolaminates fabricated by atomic layer deposition. *Applied Physics Letters*, 103(3):031903, 2013.

[107] Abdelkader Kahouli, Oleg Lebedev, Marwa Ben Elbahri, Bernard Mercey, Wilfrid Prellier, Stefan Riedel, Malte Czernohorsky, Florent Lallemand, Catherine Bunel, and Ulrike Lüders. Structural and dielectric properties of subnanometric laminates of binary oxides. *ACS applied materials & interfaces*, 7(46):25679–25684, 2015.

[108] M-H Cho, HS Chang, YJ Cho, DW Moon, K-H Min, R Sinclair, SK Kang, D-H Ko, JH Lee, JH Gu, et al. Change in the chemical state and thermal stability of hfo 2 by the incorporation of al 2 o 3. *Applied physics letters*, 84(4):571–573, 2004.

[109] Tuo Wang and John G Ekerdt. Structure versus thermal stability: The periodic structure of atomic layer deposition-grown al-incorporated hfo2 films and its effects on amorphous stabilization. *Chemistry of Materials*, 23(7):1679–1685, 2011.

[110] Tuo Wang and John G Ekerdt. Atomic layer deposition of lanthanum stabilized amorphous hafnium oxide thin films. *Chemistry of Materials*, 21(14):3096–3101, 2009.

[111] Lae Ho Kim, Kyunghun Kim, Seonuk Park, Yong Jin Jeong, Haekyoung Kim, Dae Sung Chung, Se Hyun Kim, and Chan Eon Park. Al2o3/tio2 nanolaminate thin film encapsula-

tion for organic thin film transistors via plasma-enhanced atomic layer deposition. *ACS Applied Materials & Interfaces*, 6(9):6731–6738, 2014.

[112] Lae Ho Kim, Yong Jin Jeong, Tae Kyu An, Seonuk Park, Jin Hyuk Jang, Sooji Nam, Jaeyoung Jang, Se Hyun Kim, and Chan Eon Park. Optimization of al 2 o 3/tio 2 nanolaminate thin films prepared with different oxide ratios, for use in organic light-emitting diode encapsulation, via plasma-enhanced atomic layer deposition. *Physical Chemistry Chemical Physics*, 18(2):1042–1049, 2016.

[113] Jens Meyer, Patrick Görrn, Franz Bertram, Sami Hamwi, Thomas Winkler, Hans-Hermann Johannes, Thomas Weimann, Peter Hinze, Thomas Riedl, and Wolfgang Kowalsky. Al2o3/zro2 nanolaminates as ultrahigh gas-diffusion barriers—a strategy for reliable encapsulation of organic electronics. *Advanced materials*, 21(18):1845–1849, 2009.

[114] C Zhao, O Richard, H Bender, M Caymax, Stefan De Gendt, Marc Heyns, E Young, Gert Roebben, Omer Van der Biest, and S Haukka. Miscibility of amorphous zro 2–al 2 o 3 binary alloy. *Applied physics letters*, 80(13):2374–2376, 2002.

[115] Jens Meyer, H Schmidt, W Kowalsky, T Riedl, and Antoine Kahn. The origin of low water vapor transmission rates through al 2 o 3/zro 2 nanolaminate gas-diffusion barriers grown by atomic layer deposition. *Applied Physics Letters*, 96(24):117, 2010.

[116] Garrett D Cole, Wei Zhang, Michael J Martin, Jun Ye, and Markus Aspelmeyer. Tenfold reduction of brownian noise in high-reflectivity optical coatings. *Nature Photonics*, 7(8):644–650, 2013.

[117] Nicolas Morell, Antoine Reserbat-Plantey, Ioannis Tsioutsios, Kevin G Schädler, François Dubin, Frank HL Koppens, and Adrian Bachtold. High quality factor mechanical resonators based on wse2 monolayers. *Nano letters*, 16(8):5102–5108, 2016.

[118] Gabriele Vajente, Eric K Gustafson, and David H Reitze. Precision interferometry for gravitational wave detection: Current status and future trends. In *Advances In Atomic, Molecular, and Optical Physics*, volume 68, pages 75–148. Elsevier, 2019.

[119] Benjamin P Abbott, R Abbott, TD Abbott, MR Abernathy, F Acernese, K Ackley, C Adams, T Adams, Paolo Addesso, RX Adhikari, et al. Prospects for observing and localizing gravitational-wave transients with advanced ligo, advanced virgo and kagra. *Living Reviews in Relativity*, 21(1):3, 2018.

[120] Huang-Wei Pan, Shun-Jin Wang, Ling-Chi Kuo, Shiuh Chao, Maria Principe, Innocenzo M Pinto, and Riccardo DeSalvo. Thickness-dependent crystallization on thermal anneal for titania/silica nm-layer composites deposited by ion beam sputter method. *Optics express*, 22(24):29847–29854, 2014.

[121] M Magnozzi, S Terreni, L Anghinolfi, S Uttiya, MM Carnasciali, G Gemme, M Neri, M Principe, I Pinto, L-C Kuo, and M Canepa. Optical properties of amorphous sio_2-tio_2 multi-nanolayered coatings for 1064-nm mirror technology. *Optical Materials*, 75:94–101, 2018.

[122] E Cesarini, M Lorenzini, E Campagna, Filippo Martelli, Francesco Piergiovanni, Flavio Vetrano, G Losurdo, and G Cagnoli. A “gentle” nodal suspension for measurements of the acoustic attenuation in materials. *Review of Scientific Instruments*, 80(5):053904, 2009.

[123] Gregory Harry, Timothy P Bodiya, and Riccardo DeSalvo. *Optical coatings and thermal noise in precision measurement*. Cambridge University Press, 2012.

[124] Lei Zhang, Jinlong Zhang, Hongfei Jiao, Ganghua Bao, Zhanshan Wang, and Xinbin Cheng. Thickness-dependent surface morphology and crystallization of hfo2 coatings prepared with ion-assisted deposition. *Thin Solid Films*, 642:359–363, 2017.

[125] C Chaneliere, S Four, JL Autran, RAB Devine, and NP Sandler. Properties of amorphous and crystalline ta 2 o 5 thin films deposited on si from a ta (oc 2 h 5) 5 precursor. *Journal of applied physics*, 83(9):4823–4829, 1998.

[126] J Il Langford and AJC Wilson. Scherrer after sixty years: a survey and some new results in the determination of crystallite size. *Journal of applied crystallography*, 11(2):102–113, 1978.

[127] Davide Barreca, Alberto Gasparotto, Chiara Maccato, Cinzia Maragno, and Eugenio Tondello. Tio2 thin films by chemical vapor deposition: An xps characterization. *Surface Science Spectra*, 14(1):27–33, 2007.

[128] Massimo Granata, Elodie Coillet, Valérie Martinez, Vincent Dolique, Alex Amato, Maurizio Canepa, Jérémie Margueritat, Christine Martinet, Alain Mermet, Christophe Michel, et al. Correlated evolution of structure and mechanical loss of a sputtered silica film. *Physical Review Materials*, 2(5):053607, 2018.

[129] J Jiang, A Mishkin, K Prasai, M Yazback, R Zhang, R Bassiri, M Fejer, and H Cheng. Atomic structures modeling and mechanical loss study of amorphous zro2-doped ta2o5. *https://dcc.ligo.org/LIGO-P1900371*.

[130] Le Yang, Gabriele Vajente, Mariana Fazio, Alena Ananyeva, GariLynn Billingsley, Ashot Markosyan, Riccardo Bassiri, Kiran Prasai, Martin M. Fejer, and Carmen S. Menoni. Enhanced medium range order in vapor deposited germania glasses at elevated temperatures. *arXiv preprint arXiv:2102.08526*, 2021.

[131] Mark D Ediger. Perspective: Highly stable vapor-deposited glasses. *The Journal of chemical physics*, 147(21):210901, 2017.

[132] Shakeel S Dalal and Mark D Ediger. Molecular orientation in stable glasses of indomethacin. *The journal of physical chemistry letters*, 3(10):1229–1233, 2012.

[133] Kushal Bagchi and Mark D Ediger. Controlling structure and properties of vapor-deposited glasses of organic semiconductors: Recent advances and challenges. *The Journal of Physical Chemistry Letters*, 11(17):6935–6945, 2020.

[134] Sadanand Singh, Mark D Ediger, and Juan J De Pablo. Ultrastable glasses from in silico vapour deposition. *Nature materials*, 12(2):139–144, 2013.

[135] Ralf Brüning and Tim Crowell. A method to determine the kinetics of a supercooled liquid by temperature scanning measurements applied to (li, na) acetate and geo2. *Journal of non-crystalline solids*, 248(2-3):183–193, 1999.

[136] Ralf Brüning. On the glass transition in vitreous silica by differential thermal analysis measurements. *Journal of non-crystalline solids*, 330(1-3):13–22, 2003.

[137] Matthieu Micoulaut and James C Phillips. Rings and rigidity transitions in network glasses. *Physical Review B*, 67(10):104204, 2003.

[138] AE Geissberger and Frank L Galeener. Raman studies of vitreous si o 2 versus fictive temperature. *Physical Review B*, 28(6):3266, 1983.

[139] Rui Shi and Hajime Tanaka. Distinct signature of local tetrahedral ordering in the scattering function of covalent liquids and glasses. *Science advances*, 5(3):eaav3194, 2019.

[140] Hideo Hosono, Yoshiaki Ikuta, Takeru Kinoshita, Kouichi Kajihara, and Masahiro Hirano. Physical disorder and optical properties in the vacuum ultraviolet region of amorphous sio 2. *Physical review letters*, 87(17):175501, 2001.

[141] Norbert Kaiser. Review of the fundamentals of thin-film growth. *Applied optics*, 41(16):3053–3060, 2002.

[142] Zhe Wang, Tao Du, NM Anoop Krishnan, Morten M Smedskjaer, and Mathieu Bauchy. On the equivalence of vapor-deposited and melt-quenched glasses. *The Journal of Chemical Physics*, 152(16):164504, 2020.

[143] Jessica Steinlechner. Development of mirror coatings for gravitational-wave detectors. *Philosophical Transactions of the Royal Society A: Mathematical, Physical and Engineering Sciences*, 376(2120):20170282, 2018.

[144] Denis V Martynov, ED Hall, BP Abbott, R Abbott, TD Abbott, C Adams, RX Adhikari, RA Anderson, SB Anderson, K Arai, et al. Sensitivity of the advanced ligo detectors at the beginning of gravitational wave astronomy. *Physical Review D*, 93(11):112004, 2016.

[145] Aaron Buikema, Craig Cahillane, GL Mansell, CD Blair, R Abbott, C Adams, RX Adhikari, A Ananyeva, S Appert, K Arai, et al. Sensitivity and performance of the advanced ligo detectors in the third observing run. *Physical Review D*, 102(6):062003, 2020.

[146] Alessandra Buonanno and Yanbei Chen. Quantum noise in second generation, signal-recycled laser interferometric gravitational-wave detectors. *Physical Review D*, 64(4):042006, 2001.

[147] Vladimir B Braginsky and SP Vyatchanin. Thermodynamical fluctuations in optical mirror coatings. *Physics Letters A*, 312(3-4):244–255, 2003.

[148] Ting Hong, Huan Yang, Eric K Gustafson, Rana X Adhikari, and Yanbei Chen. Brownian thermal noise in multilayer coated mirrors. *Physical Review D*, 87(8):082001, 2013.

[149] Massimo Granata, Alex Amato, Laurent Balzarini, Maurizio Canepa, Jérôme Degallaix, Danièle Forest, Vincent Dolique, Lorenzo Mereni, Christophe Michel, Laurent Pinard, et al. Amorphous optical coatings of present gravitational-wave interferometers. *Classical and Quantum Gravity*, 37(9):095004, 2020.

[150] Sonja Rau, Christian Enss, Siegfried Hunklinger, Peter Neu, and Alois Würger. Acoustic properties of oxide glasses at low temperatures. *Physical Review B*, 52(10):7179, 1995.

[151] KA Topp and David G Cahill. Elastic properties of several amorphous solids and disordered crystals below 100 k. *Zeitschrift für Physik B Condensed Matter*, 101(2):235–245, 1996.

[152] Matej Mayer. Simnra, a simulation program for the analysis of nra, rbs and erda. *AIP Conference Proceedings*, 475, 1999.

[153] Kheamrutai Thamaphat, Pichet Limsuwan, and Boonlaer Ngotawornchai. Phase characterization of tio2 powder by xrd and tem. *Agriculture and Natural Resources*, 42(5):357–361, 2008.

[154] Steven D Penn, Alexander Ageev, Dan Busby, Gregory M Harry, Andri M Gretarsson, Kenji Numata, and Phil Willems. Frequency and surface dependence of the mechanical loss in fused silica. *Physics Letters A*, 352(1-2):3–6, 2006.

[155] Alexandr Ageev, Belkis Cabrera Palmer, Antonio De Felice, Steven D Penn, and Peter R Saulson. Very high quality factor measured in annealed fused silica. *Classical and Quantum Gravity*, 21(16):3887, 2004.

[156] Tianjun Li, Felipe A Aguilar Sandoval, Mickael Geitner, Ludovic Bellon, Gianpietro Cagnoli, Jérôme Degallaix, Vincent Dolique, Raffaele Flaminio, Danièle Forest, Massimo Granata, et al. Measurements of mechanical thermal noise and energy dissipation in optical dielectric coatings. *Physical Review D*, 89(9):092004, 2014.

[157] Slawomir Gras and Matthew Evans. Direct measurement of coating thermal noise in optical resonators. *Physical Review D*, 98(12):122001, 2018.

[158] L McCuller, C Whittle, D Ganapathy, K Komori, M Tse, A Fernandez-Galiana, L Barsotti, P Fritschel, M MacInnis, F Matichard, et al. Frequency-dependent squeezing for advanced ligo. *Physical review letters*, 124(17):171102, 2020.

[159] Computed with the software pygwinc, available from https://git.ligo.org/gwinc/pygwinc.

Appendix A

Ion Dose Measurement with Faraday Cup

The assist ion dose at the substrate surface was measured with a Faraday cup (Figure A.1). The Faraday cup has a conductive cup with an electron suppressor plate in front. The ions enter and hit the cup so that charge is transferred to a connecting picoammeter.

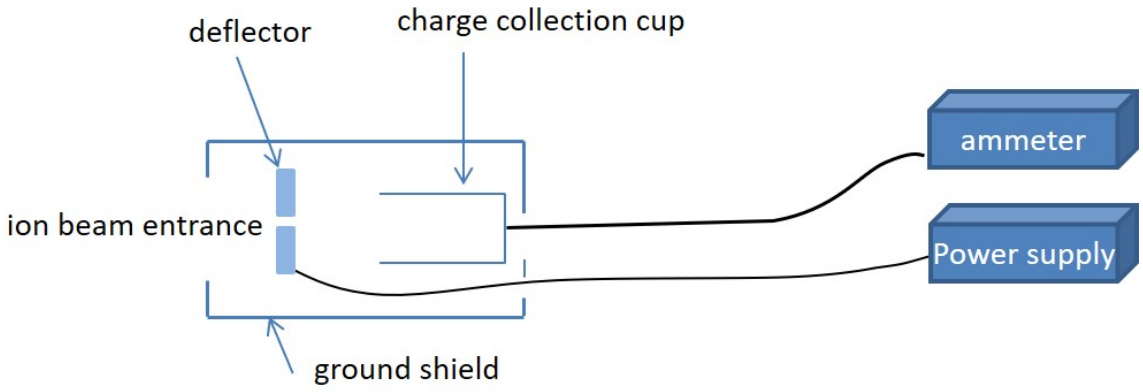


Figure A.1: Schematic of the Faraday cup measurement.

After the assist ion beam was turned on and stabilized, a negative voltage in step of 5 V was applied to the electron suppressor until no variance in current was reached (Figure A.2). The ions arriving at the surface per second N_{ions} (ions·cm^2 ·s^{-1}) can be calculated using the following equation,

$$N_{\text{ions}} = \frac{i}{e}\frac{1}{A} \tag{A.1}$$

i is the measured current created by the collected ions (μA), e is the elemental charge (A·s), A is the aperture area (cm^2). In this case, A is 0.123 cm^2 for the aperture. The current reading from the ammeter as a function of the applied voltage is plotted for different assist beam conditions

in Figure A.2. When the assist beam was at 100 V and 100 mA, the plateau of the current was around 4 μA. Increasing the beam voltage or the beam current both resulted in an increase in the assist ion dose at the substrate surface.

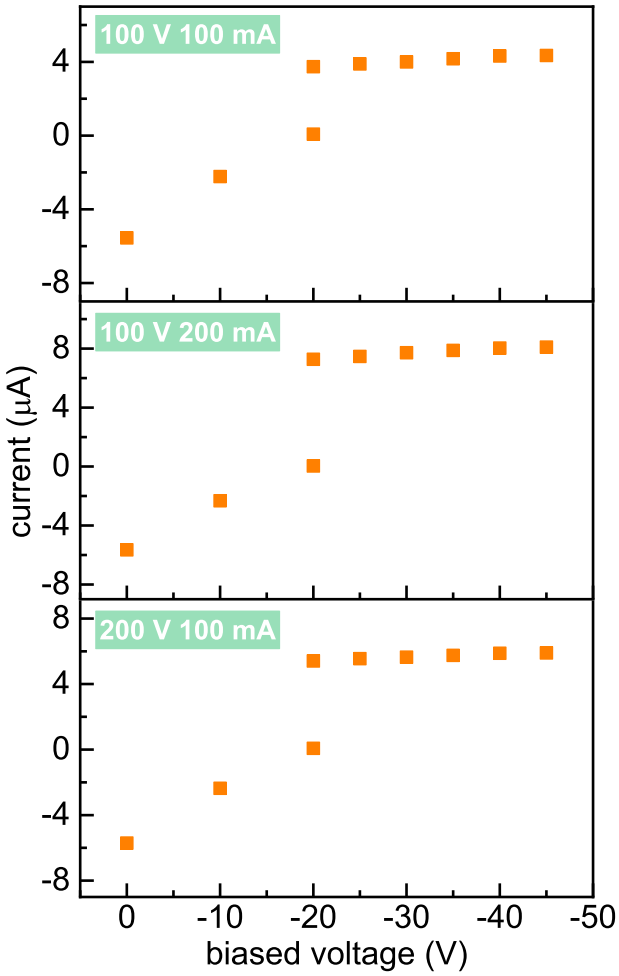


Figure A.2: Current as a function of the negative voltage applied to the deflector for assist beam of 50% Ar and 50% O_2 at different beam voltage and beam current.

The number of sputtered particles was estimated from the deposition rate with no assist ion bombardment. Considering a scenario with substrate fully covered, the atoms arriving at the surface per second per area, N_{atoms} (atoms·cm^2 ·s^{-1}), can be estimated from the following

equation:

$$N_{\text{atoms}} = \theta \frac{r \cdot A}{V} \frac{1}{A} \tag{A.2}$$

where θ is the surface coverage, which is 1 in this case, r is the deposition rate(Å/s), A is the surface area in cm^2, and V is the volume of the sputtered particles ($Å^3$).

Appendix B

Design of Nanolaminates

The cation concentration, Si/(Si+Ta) and Ti/(Ti+Ta), was aimed at ~20 at.% for both the mixture and nanolaminate samples.

To determine the cation concentration of the mixtures, x-ray photoelectron spectroscopy (XPS) measurements were carried out with a Physical Electronics PE 5800 ESCA/ASE system equipped with a monochromatic Al Kα x-ray source. A take-off angle of 45° and a pass energy of 23.5 eV were used for all scans. The neutralizer operating at 10 μA was used to counteract the charging effect of the sample. High resolution scans were obtained from the sample surface with no sputtering. The C 1*s* peak position was used to calibrate the binding energy scale of the spectra. The peak profile was fitted with the Gaussian function. To calculate the cation concentration, the relative sensitivity factor was used to convert the area of each peak to corresponding cation concentration.

To design nanolaminates with the same cation concentration ~20 at.%, the volume of each oxide in the mixture samples needs to be determined so that the layer thickness for each oxide in the nanolaminates could be determined. In the case of the SiO_2/Ta_2O_5 nanolaminate, two test runs were carried out to repeat the depositions of the 20% mixtures. In the first run, a shield was positioned between the Ta target and the substrate to block the sputtered from Ta_2O_5 depositing on the substrate.Then the thickness of SiO_2 constituting the 20% SiO_2/Ta_2O_5 mixture can be found. Similarly, the shield was used to prevent the deposition of SiO_2 in the second run to determined the thickness of the Ta_2O_5. It was found that for the mixture sample of 20 at.%,

the thickness ratio was,

$$\frac{t_{Ta_2O_5}}{t_{SiO_2}} = \frac{100.4\text{nm}}{25.2\text{nm}} = \frac{4}{1} \tag{B.1}$$

which was approximately the same as the cation ratio for Ta/Si. As such, the thickness ratio between the Ta_2O_5 and the SiO_2 layers, t(Ta_2O_5)/t(SiO_2), was designed to be around 4/1 in the nanolaminate structure. The nanolaminate samples were designed to have a 6 nm top layer of Ta_2O_5 and 15 pairs of 1.6 nm SiO_2 or TiO_2 and 6 nm Ta_2O_5.

Appendix C

GIXRD of GeO_2 Thin Films with Annealing

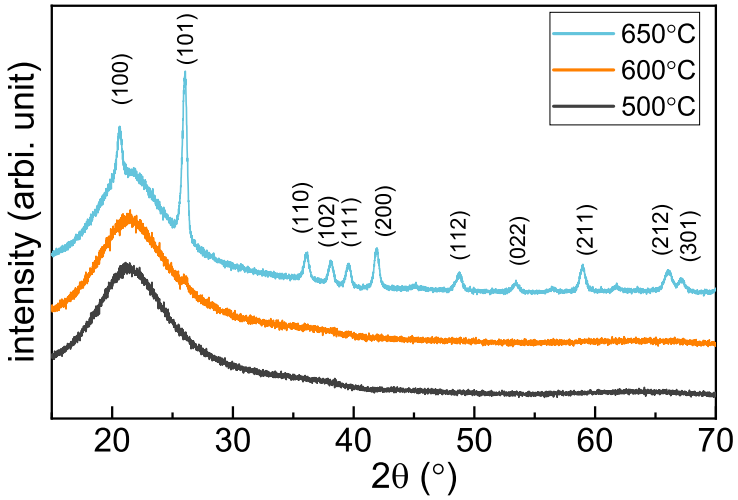


Figure C.1: Grazing incidence x-ray diffractograms for GeO_2 thin films with annealing. The peak at 2θ = 21.8° is assigned to the fused silica substrate. Diffraction peaks are attributed to the α-quartz phase of GeO_2.

Table C.1: Diffraction peak position for GeO_2 after crystallization.

Peak (hkl)	experiment, 2θ (°)	theory, 2θ (°)
100	20.60	20.56
101	26.01	25.96
110	36.09	36.01
102	38.12	38.04
111	39.57	39.48
200	41.90	41.81
112	48.73	48.69
022	53.43	53.44
211	58.96	58.86
212	66.06	66.08
301	67.16	67.06